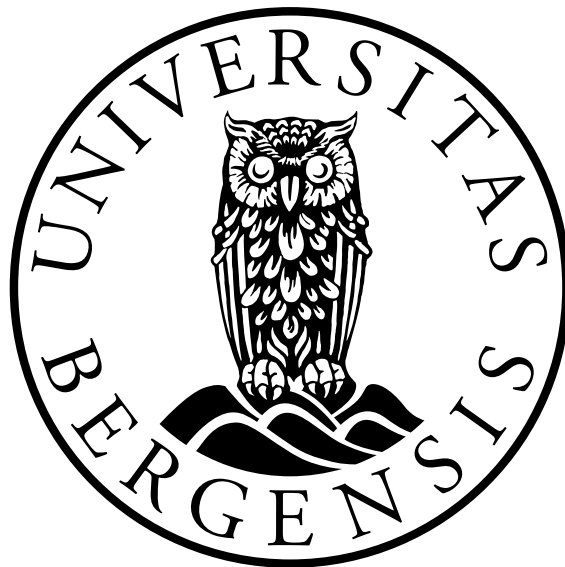


Visual Exploration of Human Physiology: Visualizing Perfusion, Blood Flow and Aging

PAOLO ANGELELLI



Dissertation for the degree of Philosophiae Doctor (PhD)

Supervised by Helwig Hauser

Co-Supervised by Ivan Viola and Odd Helge Gilja

Department of Informatics

University of Bergen

April 2012

ISBN 978-82-308-XXXX-X

University of Bergen, Norway

Submitted 23rd April 2012 (print version XXth XXXX 2012)

Some of the articles included in this thesis were originally published by IEEE, Eurographics Association or Elsevier. All rights reserved. The material is used with permission, according to the copyright agreements.

When not specified otherwise, text and figures © 2012 Paolo Angelelli.

To my family

Contents

Scientific Environment	ix
Abstract	xi
Related Publications	xiii
I Overview	1
1 Introduction	3
1.1 Challenges in visualization of physiology image data	4
1.2 Contributions and thesis structure	6
2 Related Work	7
2.1 Medical visualization	7
2.1.1 Visualization of anatomy	7
2.1.2 Visualization of physiology	8
Perfusion	9
Blood flow	10
Aging	12
Other functions	13
2.2 Visualization technology	14
2.2.1 Volume rendering	14
2.2.2 Illustrative visualization	15
2.2.3 Interactive visual analysis	15
2.2.4 Space warping	16
3 Visual Exploration and Analysis of Human Physiology Data	17
3.1 Visual exploration and semi-automatic supervised classification of CEUS perfusion data	17
3.2 Reformation and visual analysis of blood flow data	21
3.3 Aggregated visual analysis of aging data	25
3.4 Guided exploration of follow-up ultrasound examinations	28

4	Demonstration Cases	33
4.1	Visual analysis of focal liver lesions in contrast-enhanced ultrasound data	33
4.2	Visual analysis of aortic flow	35
4.3	Visual Analysis of Heterogeneous Aging Data	38
5	Conclusion and Future Work	43
II	Scientific Results	45
A	Interactive Visual Analysis of Contrast-Enhanced Ultrasound Data based on Small Neighborhood Statistics	47
A.1	Introduction	48
A.2	Related work	50
A.3	Requirement analysis	53
A.4	Visual CEUS Data Exploration and Analysis	55
A.4.1	Perfusion metrics extraction	56
A.4.2	Interactive visual analysis	59
	Similarity measure for TICs	59
	Similarity-based exploration and segmentation	59
	ROIs comparison and characterization	61
A.5	Results	63
A.5.1	Liver Lesion diagnosis	64
A.6	Conclusion	65
B	Straightening Tubular Flow for Side-by-Side Visualization	67
B.1	Introduction	68
B.2	Related Work	69
B.3	Method	71
B.3.1	Centerline-centric tubular flow straightening	72
	Prerequisites	73
	Physical space, tubular space and the straightened space	74
	Centerline centric line straightening	76
	Centerline centric vector field reformation	78
B.3.2	Side-by-side straightened flow visualizations	79
	Visualization design and layout	79
	Straightened side-by-side visualization	81
B.4	Realization and evaluation	82
B.4.1	Aortic flow visualization	83
B.4.2	Exhaust system flow visualization	83
B.4.3	Performance and Error Analysis	84
B.4.4	Evaluation	85
B.5	Summary and conclusions	86

C	Interactive Visual Analysis of Heterogeneous Cohort Study Data	89
C.1	Introduction	90
C.2	A Typical Scenario of Heterogeneous Data in a Cohort Study	91
C.3	Related Work (goes in a box)	92
C.4	A Data-Cube Based Model To Enable Interactive Visual Analysis	93
C.5	Linking Abstract and Spatial Data	98
C.6	Case Study	100
C.7	Conclusion and Future Work	102
D	Guided Visualization of Ultrasound Image Sequences	105
D.1	Introduction	106
D.2	Related work	108
D.3	Guided Ultrasound Visualization	109
D.3.1	DOI Volume Specification	109
D.3.2	DOI Profile Generation	112
D.3.3	DOI Profile Processing / Enhancement	113
D.3.4	Guided Visualization	115
	Multi-Planar Reconstruction from 2D US Data	116
D.4	Results	118
D.5	Summary and Conclusions	120
	Bibliography	123

Scientific Environment

The research presented in this thesis has been conducted within the Visualization group at the Department of Informatics, University of Bergen. The work has also been supported by the MedViz initiative in Bergen (PK1760 Project 11). Part of the research presented here has also been supported by the IllustraSound research project, funded by the VERDIKT program of the Norwegian Research Council (Nr. 193170). Part of this research has also been done while on a research stay in, and in close collaboration with, the Visualization Group at the University of Magdeburg.

UNIVERSITY OF BERGEN
Department of Informatics



ICT

**Research School in
Information and Communication Technology**



FROM VISION TO DECISION

**ILLUSTRA
SOUND** 

Abstract

With the technological advancements in medical imaging, it is nowadays possible to capture in-vivo information related to different human physiological systems. Such data extends the more traditional anatomical scans, but add size, complexity and heterogeneity. In addition, while anatomy data is defined in three-dimensional space, and 3D graphics techniques can be used to represent it on the screen, physiology information is often more abstract, and require tailored solutions to be represented in combination with their anatomical context.

This thesis presents solutions for visualizing selected aspects in three domains of physiology: blood flow, perfusion and aging. With respect to blood flow, it includes a technique to enhance the side-by-side visualization of the tubular flow in vessels. This result is achieved with a method that generates straightened visualizations of the flow in its context, which can be easily aligned and then related to each other. With respect to perfusion, this thesis includes an interactive visual analysis solution that ease and improve the exploration, segmentation and analysis of perfusion data acquired using contrast-enhanced ultrasound. This result is achieved by using a statistical framework to extract enhancement information, and an interactive, correlation-based approach to classify the tissue based on similarity. Finally, with respect to aging, two solutions to help exploring large data collections of repeated examinations are presented. In one, interactive visual analysis methods are employed to explore and analyze cohort study data, while the other focuses on the guided exploration of repeated ultrasound examinations. Demonstration case studies are include to exemplify the utility of the presented work.

Related Publications

This thesis is based on the following publications, written during the Ph.D. project of the thesis author (see Part II of the thesis):

Paper A Paolo Angelelli, Kim Nylund, Odd Helge Gilja and Helwig Hauser. **Interactive Visual Analysis of Contrast-Enhanced Ultrasound Data based on Small Neighborhood Statistics.** In *Computers & Graphics*, volume 35, number 2, pages 218–226, 2011.

Paper B Paolo Angelelli and Helwig Hauser. **Straightening Tubular Flow for Side-by-Side Visualization.** In *IEEE Transactions on Visualization and Computer Graphics*, volume 17, number 12, pages 2063–2070, 2011.

Paper C Paolo Angelelli, Steffen Oeltze, Judit Haász, Cagatay Turkay, Erlend Hodneland, Arvid Lundervold, Astri Lundervold, Bernhard Preim and Helwig Hauser. **Interactive Visual Analysis of Heterogeneous Cohort Study Data.** *After a first round of reviewing, a major revision is now in preparation for the journal Computer Graphics and Applications.*

Paper D Paolo Angelelli, Ivan Viola, Kim Nylund, Odd Helge Gilja and Helwig Hauser. **Guided Visualization of Ultrasound Image Sequences.** In *Proceedings of the Eurographics Workshop on Visual Computing for Biology and Medicine (VCBM), 2010*, pages 125–132, Leipzig, Germany, 2010.

The thesis author is also the main author of the publications above. In addition, the following publication is also related to the thesis:

Paper 1 Sebastian Schäfer, Paolo Angelelli, Kim Nylund, Odd Helge Gilja and Klaus Tönnies. **Registration of ultrasonography sequences based on temporal regions.** In *Proceedings of the 7th International Symposium on Image and Signal Processing and Analysis (ISPA), 2011*, pages 749–754, 2011.

The papers **A** and **D** have been done in cooperation with two domain scientists from the National Centre for Ultrasound in Gastroenterology from the Institute of Medicine at the University of Bergen, Norway, Kim Nylund and Odd Helge Gilja (also my co-supervisor in this PhD project), and my supervisor, Helwig Hauser. Paper **D** was also co-authored by Ivan Viola, also my co-supervisor. In both of these papers i was the principal researcher on the visualization side, while Kim Nylund was the principal researcher on the medical side. Paper **C** has been done in cooperation with the Department of Simulation and Graphics, University of Magdeburg, Germany (Steffen Oeltze and Bernhard Preim), and with the Neuroscience Research Group at the Department of Biomedicine, University of Bergen, Norway (Arvid Lundervold and Astri Lundervold, Erlend Hodneland and Judit Haász). In this paper i was the principal researcher on the visualization side, while Judit Haász was the principal researcher on the medical side, contributing with problem and solution definition and also with the evaluation. In this work, Erlend Hodneland helped with the interpretation of the medical image data according to the addressed application domain. My colleague Cagatay Turkay has also contributed with respect to the visual analysis of high-dimensional data. Paper **B** was carried out by me and my supervisor, Helwig Hauser. Finally, Paper **1** represent the research of my colleague, Sebastian Schäfer, from the Department of Simulation and Graphics, University of Magdeburg, Germany. I contributed in the definition of the problem and possible solutions, and helped in writing up the research.

Part I

Overview

CHAPTER 1

Introduction

Physiology can be defined as the science of life processes. Its goal is to explain the physical and chemical factors that are responsible for the origin and progression of life. Since even a small malfunction in one of the many processes in the human body can cause illness or even death, then it becomes clear what importance the study of physiology and the detection of malfunctioning in physiological processes has in medicine. This involves the study of mechanical, physical, and biochemical functions of human organs, and the cells of which they are composed, as well as the interaction between organs and cells [56]. This study operates on two different levels: molecular (or cell) and organ level. While cell level physiology is mainly subject of study in biology, the principal level of focus of physiology in medicine is mostly at the level of organs, and this is also the domain focus of the work presented in this thesis.

The visualization of organ level (or macro scale) physiological processes, or functions, is, in fact, a special subfield of computerized medical data visualization. This research field is often referred to, by researchers in the field, simply as medical visualization. However, in other domains, such as medicine, this term is sometimes used to address a broader set of medical imaging related fields, including medical imaging itself, medical image processing, medical image analysis, as well as computerized medical data visualization.

This broader set of medical imaging related fields was initiated at the end of the 19th century, not at the least with the invention of X-ray imaging [155]. Until the early seventies of the 20th century, it mostly amounted to radiological imaging. However, with the advent of computers, radiological data began to be processed, analyzed and visualized with the aid of computers [122]. In today's medical visualization, here considered as

the superset of medical imaging related fields mentioned above, computer aid has become essential and unavoidable, and this field could therefore be also named “computational medicine”¹ [72]. The work presented in this thesis does not attempt to address the physiological aspects in computational medicine as a whole. It is instead focused on the computerized visualization of physiological data, even if it touches upon other medical imaging related fields as well, such as data processing and analysis.

In the early years of computational medicine a lot of effort has been put on medical imaging for the acquisition of three-dimensional image data, by developing new imaging modalities such as Computed Tomography (CT), Magnetic Resonance Imaging (MRI) and also Ultrasound, among the others [81]. From a computerized visualization perspective, it was primarily the rendering of the three-dimensional data [65, 173] that was central to visualization research. The developed rendering solutions have been successfully employed in different medical applications, such as treatment and intervention planning, intra-operative support, diagnosis, education and training, and others [146].

However, with all the immense technological innovation in medical imaging, it became possible to acquire a much broader spectrum of medical data for the patients. New characteristics of such data include, for example, time-dependency, since the technology for several imaging modalities became fast enough to perform repeated acquisitions in small time frames. This led to medical images, which not only capture an instantaneous picture of the patient’s anatomy, but a time-varying capture of some aspect of the patient’s physiology. In addition, thanks to the introduction of new elements in the examinations, such as measures of blood tracers and new imaging protocols, medical imaging became able to capture a richer set of physiological parameters, such as measures of blood concentration, blood flow, neuronal activation, water diffusivity, etc. [42]. With the capability of acquiring time-varying sequences of anatomical snapshots, in combination with blood tracers and new additions to the imaging protocols, it is now possible to image a broader spectrum of physiological processes.

1.1 Challenges in visualization of physiology image data

Since physiological processes can be observed only in-vivo, the importance of medical imaging for capturing human physiology analysis in diagnosis, treatment planning and research became crucial. Physiological processes have, of course, a strong reference to the organs they involve, and, in this

¹In the following, this is the term that will be used to address such a superset of disciplines, whereas the term “visualization” will only stand for the “computerized visualization” part.

sense, anatomy visualization can be considered as a part of physiology visualization. Still, physiology data comprise other information, in addition to anatomy, encoded in form of additional data dimensions and features, which are usually not immediately visible. For this reason, and when comparing to the visualization of anatomy data, more advanced solutions are required to convey a more complete picture as provided by physiology data. The additional information would otherwise be difficult to represent by, e.g., using classical visualization approaches, common for anatomy inspections, such as, for example, slice-based visualization.

In the simplest case, physiological datasets have “just” an additional temporal dimension, but they may also become as complex as time-varying vector or tensor fields, for example. Physiology data can be also multi-modal: an example is the combination of functional MRI (fMRI) with tractography data extracted from diffusion tensor imaging (DTI) MRI data, in order to understand functional connections between brain regions [197]. Acquisitions can also be heterogeneous: an example is, again, fMRI brain activation data, which is anatomically located, acquired together with EEG data, which has a different anatomical reference. Such type of acquisitions can be performed during cognition tests, where the results of the tests are also combined, consisting of additional abstract data with no anatomical reference [197].

When developing new solutions for visualizing physiology data, these additional data features have to be treated properly. The time dimension, for example, must be communicated to the user, either by, e.g., encoding it in a cine-loop or by representing it in other ways. Multiple modalities must be combined or linked in order to relate the different measures they provide with each other. This task becomes even more complex when the data is heterogeneous, and spatial and non-spatial information need to be linked. Moreover, when investigating physiological processes, analyzing the acquired functional data in order to extract different functional parameters becomes even more central than for anatomy data [110, 132]. Finally, physiological data normally contain much more information than data representing only the anatomy, and technologies for smart access to the information of interest in such data sets are needed, in order to effectively inspect them.

The work presented in this thesis is an attempt to address some of the challenges encountered while visualizing and visually analyzing imaging data of physiological processes, for the specific domain areas of blood flow, perfusion and aging. This work is part of a new movement in the field as such, amounting to a few selected pioneering steps into the direction of advanced physiology visualization. Even though some work has been already done in this direction (see Chapter 2, for an overview on the related work in physiology visualization), the problem of visualizing physiology is still far from being adequately covered. In this respect, the work pre-

sented in this thesis extends the state of the art in the visualization of human physiology.

1.2 Contributions and thesis structure

The main contributions, as presented in this thesis, are as follows:

1. A two-level approach for the analysis of Contrast-Enhanced Ultrasound (CEUS) perfusion data. It consists of a perfusion metrics extraction method for CEUS imaging, based on small neighborhood statistics, to address the signal instability of this modality. This method can be seen as the back-end of a new approach to a supervised classification of CEUS perfusion scans, based on temporal correlation of the enhancement metrics.
2. A new, two-staged pipeline enabling the visual side-by-side comparison of blood flow data. It consists of a method to perform a curve-centric reformation of tubular flow, in the form of raw vector field or already integrated geometry. A solution to juxtapose (and compare) straightened views of blood flow data is introduced, in order to convey spatial orientation as well as qualitative and quantitative information of the flow.
3. A data-cube based model for enabling the visual analysis and integration of heterogeneous data collected in cohort studies, and the linking of structural (anatomical) and abstract data.
4. A navigation method to explore (multiple) tracked Ultrasound cine-loops, and identify the parts in the cine-loops containing the regions of interest. In this way, the data containing the regions of interest can be easily extracted and compared also across multiple examinations, in order to also study physiological changes over time.

This thesis is organized as follows: In chapter 2, the related state of the art with respect to the visualization and the visual analysis of physiology data is discussed, as well as the related visualization technology. In chapter 3 the different contributions of this work are then described in more detail. In chapter 4 the presented approaches are exemplified in different application cases, in order to demonstrate their effectiveness. Chapter 5 concludes the first part of this thesis. The second part of this thesis then includes the four main papers that resulted from this work up to now.

CHAPTER 2

Related Work

Even though the field of physiology visualization is relatively new in medical visualization, during the last years a number of solutions have been developed for representing and analyzing certain physiological processes. These methods often incorporate techniques to visualize the anatomy, to depict these function in their anatomical context, providing a spatial reference for the functions, and this is also done in the work presented in this thesis. This chapter presents, in the next section, the related work in the field of medical visualization. Afterward, the technological solutions related to those adopted in the work presented in this thesis will be discussed.

2.1 Medical visualization

The field of Medical Visualization started in the early '70s, when the computers became able to generate pictures on screen [55, 159]. Nevertheless, this field grew tremendously already in the following years [64]. In this section, the work related to medical visualization is classified in two parts: anatomy visualization and physiology visualization. The latter part discusses solutions addressing problems similar to those that are addressed by the work presented in this thesis. The former part briefly discusses solutions to the visualization of anatomical images, which is a problem often embedded in the visualization of physiology.

2.1.1 Visualization of anatomy

Before the introduction of tomographic imaging, it was impossible to obtain both 3D pictures of the human body and density information, as conventional X-ray imaging only provide a superimposition of objects along

each ray path. But tomographic imaging made possible to obtain information about internal densities on cross sections of the patient. Starting in the early seventies, medical visualization has therefore strongly focused on reconstructing and rendering 3D surfaces from medical 3D scans [64, 76]. In Section 3.1, 3.2 and 3.4, volume visualization solutions have been used to render the organs involved in the physiological processes under investigation. Section 2.2.1 discusses methods for the rendering of 3D volumetric data. In Section 3.3, the surfaces of the brain and brain segments have been extracted and visualized, instead of utilizing direct volume rendering solutions. The advantages and disadvantages of surface extraction and techniques, as compared with direct volume rendering techniques have been long discussed, and Udupa et al. [178] presented an overview on the subject already in the nineties. In Section 3.3, a streamline visualization technique [50] has also been employed, to represent white matter fiber tracts and communicate fiber integrity information directly within its anatomical context. The problem of visualizing white matter fibers has also been addressed by others, for example by enhancing the perception of the fibers using line illumination and shadowing typical of hair rendering [136], by adding depth-dependent halos to generate an illustrative rendering of dense line data [39], or by fusing the fiber tracts line data with fMRI information, and structural MRI information, in order to interactively assess which functional areas would be involved, in case of a brain tumor resection [14].

These anatomy visualization solutions, as well as others, have been employed in different domain-specific application fields, such as intervention and treatment planning, diagnosis, as well as education and others. What is given above is only a short wrap-up of this field, but extensive coverage of the visualization solutions for anatomical images, and their applications, is provided by Bartz and Preim in the book entitled “Visualization in Medicine” [146].

2.1.2 Visualization of physiology

Human physiology information can come from two different sources: imaging data or modeling and simulation data.

Even though the focus of this thesis work is on the visualization of physiology information from imaging data, extensive work has been done to also model and simulate physiological processes, and to visualize the results of the simulations.

Comprehensive projects have also been initiated for a systematic modeling of the whole human functional behavior, also called *human physiome*. For example, the aim of the IUPS Physiome project [69], the most known of the physiome projects, was to develop integrative models at all levels of biological organization, from genes to the whole organism. The outcome

of this project was a modeling framework for understanding biological structures and functions, from proteins to whole organisms. For this purpose, a set of modeling languages, including CellML, TissueML, AnatML and OrganSystemML, were developed to model physiology at its different scales. The usage of a standard declarative language to define, for example, anatomy allowed the creation of compliant viewers able to visualize all the different models. Other physiome projects having similar intents have also been initiated: among the others, the EuroPhysiome Initiative [43], the NSR Physiome Project [9], and the Japanese Physiome Initiative (physiome.jp). Most of these projects are now connected, worldwide, under the initiative known as the Virtual Physiological Human.

However, despite the big effort that is being put on modeling physiology, with the goal of becoming able to create patient-specific models [7], this is still not generally possible. For this reason, at the present, it is mostly image data that is analyzed and visualized directly, in order to diagnose malfunctioning in the physiological functions of patients. Now, the related work on visualization of physiology from image data is discussed, specifically for the three domains that are addressed by the presented work, and also for other domains that have received attention in the medical visualization field.

Perfusion

Perfusion imaging techniques measure the amount of blood in tissue over time, thanks to the use of specific blood tracers. These data are acquired to support essential diagnostic tasks, such as ischemic stroke diagnosis, inflammation assessment, detection of coronary heart diseases and different types of tumors [147]. The amount of blood in tissue is, in fact, related to the level and type of tissue vascularization [116]. For this reason, the perfusion kinetic of the blood over time is analyzed, and expressive perfusion parameters are determined, in order to come up with a diagnosis [147].

To analyze and effectively communicate this information, a number of work have been proposed in the recent years. Mlejnek et al. [117] presented in 2005 the profile flags, a technique to interactively probe 3D perfusion data, and pin, in space, relevant regions, showing their perfusion in a contextual banner. Coto et al. [29], in the same year, presented the first Interactive Visual Analysis (IVA, see section 2.2.3) approach for perfusion data. In MammoExplorer, the authors interactively classified the tissue by brushing scatterplots opposing MRI T2 intensity values and perfusion enhancement values. More recently, Oeltze et al. [130] performed IVA on MRI perfusion data and added principal component analysis on different derived perfusion parameters, showing how some of these parameters contain redundant information. Oeltze et al. [132] also presented a comprehensive visualization solution for myocardial perfusion data. In this

work, the authors combined a mapping on the cardiac wall of contractility and viability information with carefully designed glyphs that communicate the perfusion in the different sectors of the left ventricle, following the Bull's Eye Plot segmentation [21]. Finally, Glaßer et al. [53] proposed a new type of a 2-dimensional glyph, used to encode two different perfusion parameters over a single parametric map. This technique, in combination with change diagrams, has been used to study the perfusion of breast perfusion acquired using MRI. An overview of the proposed methods for visualizing perfusion data acquired with CT or MRI is also provided by Preim et al. [148].

With respect to specific analysis and visualization challenges introduced by CEUS perfusion data, the available solutions are mostly limited to added rigid or also deformable registration capabilities to applications showing basic perfusion analysis functionalities (Qontrast [3], QontraXt [68], SonoLiver [153, 154], SonoProstate [46]).

The work presented in this thesis addresses some of the specific challenges of this modality (noisy enhancement and residual motion artifacts), as well as introducing a method for supervised classification of the tissue based on perfusion similarity. This method allows fast and precise segmentation of the different regions in the data, which can be challenging otherwise, especially with complex structures.

Blood flow

The imaging and analysis of cardiovascular morphology, functions and hemodynamics has a strong impact on the diagnosis of cardiovascular diseases [16, 168], as well as on the understanding of atherogenesis and arterial remodeling processes [52, 94]. For this reason, blood flow in its context has been investigated in different ways during the last years. Blood flow information is imaged in medicine using mainly two different modalities: power and color Doppler Ultrasound, and Phase-Contrast MRI (PC-MRI). Doppler US is a real time imaging modality, that can capture a whole image (or volume, in 4D Doppler US) several times per second. These data, however, contains only information about the velocity of the flow along the US beam direction [114]. They are, therefore, acquisition dependent, and the information change if the probe orientation change. PC-MRI, instead, produces full three-dimensional vector fields of the blood flow at high frame rate. However, these volumes are assembled by imaging only a little part of the volume at each heart cycle [137]. These parts are synchronized using Electrocardiography (ECG) information, and therefore this modality works best for patients without cardiac dysrhythmia. Concerning the visualization of color Doppler data, classical methods superimpose color Doppler information (red for flow shifting toward the US beam, and blue shifting away from it) over the b-mode images. The multi-component

nature of the problem introduces challenges for conveying both the relevant contextual anatomical structures, and the color Doppler information. Petersch and Hönigmann [140] presented a new method to visualize 3D color Doppler information in its context, combining photorealistic and nonphotorealistic rendering methods such as gradient shading and silhouette rendering.

Moving to vector field data, work has been done to both visualize the blood flow itself, as well as other scalar hemodynamic parameters, such as the wall shear stress (WSS), caused by the flow on the arterial walls. Regarding blood flow visualization, van Pelt et al. [180] used different illustrative techniques to enhance the classical visualization of aortic flow. In their work, the authors included cell shading and silhouette rendering for the anatomical context, as well as flow arrows and exploded views showing a Doppler-like visualization of the flow. In a following work, van Pelt et al. [181] also introduced additional illustrative techniques to visualize blood flow, where illustrative particles were “injected” in the blood, and depicted using contours and speed lines. Exploded views have been also proposed by Mark et al. [110], and used to present analytical information about the flow for each user-specified cross section of the aorta, in a comprehensive solution for the visualization of aortic flow. A more analytical approach to the visualization of blood flow has been presented by Friman et al. [45]. In this work, the trajectories of the flow have been computed taking into consideration the noise generated by the PC-MRI imaging modality. Therefore, for each integration step, a probabilistic scheme has been used to determine the most probable trajectory, as well as the set of possible trajectories. An extension of this work has been presented by Schwenke et al. [164], using anisotropic fast marching to compute the minimal path trajectory from tensors combining blood flow directions as well as the estimated uncertainty. Neugebauer et al. [121] presented an anatomy guided solution to explore blood flow in complex anatomical structures, such as cerebral aneurysms, including appropriate anatomy based placement of the seeding body, to fit the typical flow dynamics in aneurysms. Gasteiger et al. [51] proposed to use a combination of illustrative techniques (simple contours) with other rendering styles to enhance the perception of the flow in cerebral aneurysms. Gasteiger et al. [50] also proposed the “Flow Lens”, a focus+context approach to enhance the investigation of different blood flow parameters (including WSS) in the context of cerebral aneurysm flow analysis.

Concerning wall shear stress visualization, Frydrychowicz et al. [47] has mapped WSS estimated using CFD methods from PC-MRI data on a visualization of the aortic arch, by using discs that encode the WSS for each sector of the aortic sections. Neugebauer et al. [120] also visualize the WSS in cerebral aneurysms by mapping this flow aspect on the surface of the aneurysm. However, they also add a 2D projection map to also

visualize, with a single image, the sides of the aneurysm that are not visible, including the backside. Borkin et al. [17] presented a method to create comprehensive visualizations of the WSS in the whole coronary artery tree, by straightening the vessels walls, and representing them in an illustrative tree structure. The WSS was then color mapped on the straightened vessels, also depicting the vessels diameters. In this way an overview is provided, as well as easing the comparison of the different branches of the coronary artery tree.

The work presented in this thesis addresses the related problem of providing an overview of the unsteady blood flow through blood vessels. By enabling the generation of straightened flow visualizations, it becomes easier to relate different views of the flow in the same context, as they can be effectively aligned to each other. This method could be also combined with the one proposed by Borkin et al., to provide a comprehensive visualization of the blood flow in the whole coronary artery tree.

Aging

As compared to perfusion and blood flow, which are relatively short-termed aspects, the physiological effects of aging on the human body and functions appear in longer time frames. Therefore, for this purpose, studies carrying out repeated acquisitions over longer time frames have been performed. Such studies are normally performed on a larger sample of individuals, in order to obtain statistically significant results [197, 198]. The resulting data are therefore quite large, comprising heterogeneous multimodal information about many subjects, examined multiple times. The analysis and visualization of such large data is normally performed by manually extracting the subset of the data needed to confirm or discard specific hypotheses under investigation. These data are then statistically processed, and the results are normally displayed with static images [198]. In the master thesis work of Eikeland [37], IVA techniques are used to perform an exploratory analysis of such type of datasets (the OASIS database on Alzheimer's diseases [109]). In this work, a parallel coordinate plot was used to identify interesting groups of patients, and different fused views were used to compare the subjects in these groups. Steenwijk et al. [169] also proposed an interactive visual analysis solution for exploring and analyzing cohort study data, having a similar goal to the one in section 3.3. Their solution consists of a back-end system constructed on top of a relational database, that is queried by a front-end comprising coordinated multiple views and brushing capabilities. Compared to the solution presented here, their approach is based on a more classical relational database for the data storage and retrieval, instead of OLAP technologies. These technologies are known to be more efficient for the processing and aggregation of large amount of data. Less heterogeneous data, in the form of

personal health history records data have been also visualized, for example using Lifelines [141], PatternFinder [40], or other methods for categorical searching and group comparison [191].

Other functions

Advanced visualization solutions have also been presented for other types of physiological functions. Cardiac functions, for example, have been covered in different aspects. Termeer presented, in 2009, a phd thesis [174] containing a comprehensive set of visualization solutions for cardiac MRI data, to enable the assessment of coronary artery disease. These solutions include the volumetric bull's eye plot, several techniques to relate functional information to heart anatomy, and a method to simulate myocardial perfusion, given structural data of the heart. Meyer-Spradow et al. [115] proposed to use supertoroidal glyphs to combine heart functional information with perfusion information of the ventricular wall. These glyphs are placed on the surface of the ventricle, and their shape is designed to minimize the occlusion of the ventricular wall, and thus the information mapped onto it. Kondratieva et al. [88] visualized the anisotropic water diffusion properties of the cardiac muscle by applying GPU based particle tracing. Another method to visualize this physiological aspect, not only in the cardiac muscle but in other type tissue as well, and normally defined on tensor fields, consist of using glyphs. These have been proposed in different shapes, such as ellipsoids [92], superquadrics [82], or Q-Balls [31].

Different solutions for the visualization of functional brain data have also been proposed. Anderson et al. [4] examine working memory by means of S-transformed representations of eeg data, and topographic maps, to provide a spatial indication of brain activity. Crippa et al. [30] visualize the connectivity information between functional brain regions, acquired using resting state fMRI examinations. To do so, a parcellation of the gray matter into functionally distinct areas is performed, and visualized in a topographic map, where these areas are also subdivided in Voroni cells, representing EEG electrodes. Van Dixoorn et al. [179] presented an IVA solution to explore fMRI data. In their work, the authors make use of linked views providing an anatomical rendering of the involved functional areas, a 3D graph representation of the resting state network, a radial graph representation of the connectivity between functional areas, and a scatterplot to perform selections.

Other physiological functions have been also addressed from a visualization perspective. These, among the others, include respiration [98], motion [77, 89, 90] and metabolism [156].

2.2 Visualization technology

The work presented in this thesis involves different visualization technologies to reach the intended goals. The most relevant areas of visualization from which technologies have been incorporated in the presented work, and in certain cases extended, are volume visualization, illustrative rendering, interactive visual analysis and space warping. In the next section, the work related in each of these areas is discussed.

2.2.1 Volume rendering

Three-dimensional data visualization has been a central area of research ever since the early seventies. Herman [65] reports the work of Greenleaf et al. [55] as the first example of 3D data visualization. However, more general techniques for volume rendering began to appear only in the late seventies, with the Cuberille being one of the first [22, 66]. The images generated by the cuberille algorithm were not smooth, being the algorithm able only to approximate a surface with a boundary surface, binarily including or excluding entire voxels, and to obtain a smooth surface, a low-pass filtering procedure was employed. Other algorithms to extract surfaces were also presented (Keppel et al. [79]), but the first high quality surface extraction algorithm was the marching cubes, presented by Lorensen et al. [105], and still widely employed for computing isosurfaces from volume data. Isosurface extraction techniques are widely used, but are based on precomputation, and to display multiple surfaces semi-transparently, order-independent alpha blending techniques must be employed. In addition, the final image is contributed only by the extracted surfaces, thus discarding all the rest of the data. Drebin et al. [35], as well as Levoy [102], presented the first algorithms to display surfaces from volume data directly, by casting rays from each screen pixel. For this reason, this family of algorithms are called *direct volume rendering* algorithms. These graphics algorithms are normally slower than rendering extracted isosurfaces, but all the data can contribute to the final image, potentially generating more accurate images. Kaufman [76] as well as Kaufman et al. [24] extensively covered these early achievements on volume graphics. In more recent years, direct volume rendering techniques have been accelerated using the modern GPU based graphics hardware, making them able to perform interactively. Hadwiger et al. [57] published a comprehensive work on the acceleration of volume graphics using the computational power provided by GPUs. Finally, with modern GPUs, it became also possible to approximate global illumination in volume rendering at interactive frame rates. Methods to achieve this include dynamic ambient occlusion [157], multi-directional occlusion shading [166], or even ray tracing solutions [91]. Lindemann and Ropinski published a study on the

effect of various advanced global illumination models for volume rendering on image comprehension [104].

2.2.2 Illustrative visualization

Illustrative visualization is the branch of visualization that makes use of non-photorealistic rendering techniques [54] to abstract and simplify the data representation, conveying only selected aspects of it. These techniques are often an attempt to mimic the work of illustrators, who emphasize certain features while suppressing others by using different levels of abstraction for different data aspects [186]. Illustrations are especially used in medicine, being their main purpose to communicate information and not necessarily to look photo-realistic. In physiology, in particular, medical illustrations are widely used, and they abstract the context (anatomy), representing only the relevant features that enable to convey the physiological process that is the focus [56]. Different attempts to mimic the work of medical illustrators have been done in medical visualization too, and Viola et al. [188] presented, in 2006, a comprehensive tutorial on this topic.

2.2.3 Interactive visual analysis

In the work presented in this thesis there is a various degree of Interactive Visual Analysis (IVA) technologies included. This ranges from pieces of work where IVA is integral part of the solution (see section 3.1 and 3.3) to other pieces of work where IVA is less prominent (section 3.2 and 3.4).

IVA has its roots in the seminal work on exploratory data analysis by Tukey [176]. Up to that point, much of the statistical visualization consisted of static images of the results. Tukey suggested to connect the visualizations directly to the data, also using interaction. The basic idea of IVA is to combine multiple views on the data, and coordinate them so that the user can visually correlate their content. This technique is also known as Coordinated Multiple Views (CMV), and Roberts provides an overview on their use in exploratory visualization [152]. Then, on such coordinated multiple view (sometimes also referred to as linked views), interaction methods such as *brushing* [10] are employed, in order to define a data selection (a tagged subset of the data). The results of brushing are then propagated to linked views, which show the selected data items in other ways. This selection mechanism is often complemented by so-called focus+context methods, as illustrated by Hauser [60], that are used to emphasize the tagged subset of the data (the focus), while maintaining an overview on the rest of the data (the context).

IVA is very close, in its goals and methods, to another field, called Visual Analytics (VA), defined by Wong and Thomas [195] as the science of

analytical reasoning facilitated by interactive visual interfaces. For both IVA and VA, the way of proceeding in the visual exploration follows the steps given by Schneiderman [165] in the so-called visual information seeking mantra: “Overview first, zoom and filter, then details-on-demand”. Keim et al. [78] found that, in certain cases, with large amounts of data, it might not be possible to get an overview on the data. He therefore extended Shneidermans mantra to “Analyze First, Show the Important, Zoom, Filter and Analyze Further – Details-on-Demand”. Finally, different applications and frameworks include the IVA technologies discussed above, like the SimVis framework [32], ComVis [111], or XmdvTool [192].

2.2.4 Space warping

The contribution presented in section 3.2 introduces a method that is used to create straightened visualizations of tubular blood flow. This method can be considered as a space warping technique. In this area of research, Daae Lampe et al. [93] presented a new technique to perform curve-centric reformation of scalar volumes (CCVR), straightening the original 3D scalar data into a new volume, centered around a 3D curve. Chen et al. [25], and Correa et al. [28], proposed more general space warping methods, based on spatial transfer functions and generalized displacement mapping. Birkeland et al. [13] extended these methods to interactively generate view-dependent peel-aways of medical scans. Finally, Ropinski et al. [156] applied flattening techniques to volumetric scans of mice aortas, to provide a navigational view that links 2D and 3D visualizations of their multimodal datasets.

CHAPTER 3

Visual Exploration and Analysis of Human Physiology Data

This chapter discusses the contributions as resulting from the research project that is covered in this thesis. While this chapter focuses primarily on the contributions of this work, a number of related demonstration cases are presented in Chapter 4.

3.1 Visual exploration and semi-automatic supervised classification of CEUS perfusion data

Contrast-enhanced imaging (CE) is an increasingly used approach in medicine to analyze the physiology of blood perfusion in tissue, which correlates with the level and type of tissue vascularization [116]. This non-invasive imaging modality is used for different purposes, such as ischemic stroke assessment, inflammations assessment, and oncologic diagnosis [85, 149, 194]. To perform the diagnosis, the imaged data can be analyzed and quantified after the examination. So-called time-intensity curves (TIC) are computed from the time series for each pixel (2D+time data), or voxel (3D+time data). A TIC represents the enhancement in the corresponding region as a function of time, and correlates with the perfusion kinetics of the blood in the location after the injection of the contrast agent. Parameters describing the kinetics of blood perfusion are extracted from the TICs, then analyzed and compared in different regions to diagnose lesions characterized by abnormal perfusion. Examples of such parameters are *time-of-arrival* (TOA) of the contrast, *time-to-peak* (TTP) enhancement, or the *peak enhancement* (PE) itself, and others.

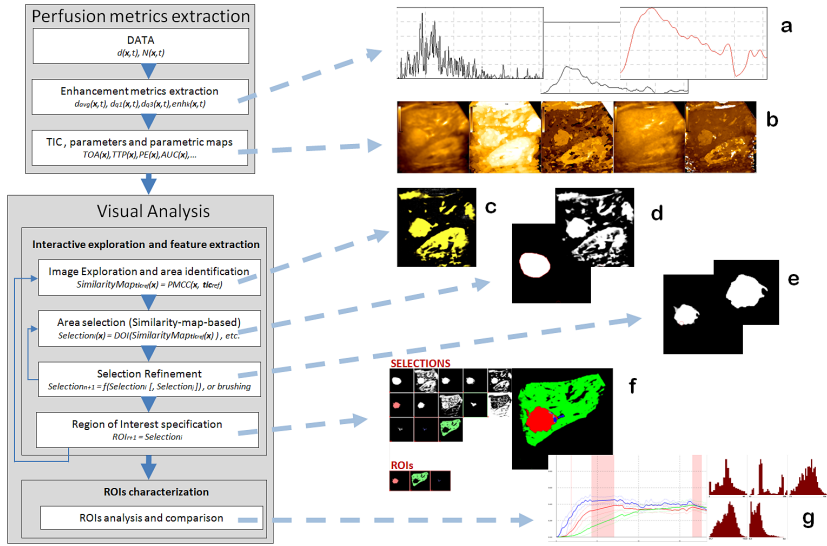


Figure 3.1: Illustration of the presented pipeline solution. In the first stage enhancement metrics are extracted (a) and parametric maps are computed (b). In the IVA stage, data are explored interactively using correlation analysis (c), and selection masks can be automatically extracted (d). Masks can be automatically combined or refined (e) and selected as ROI (f). Finally, the ROIs can be analyzed and compared to assess the tissue condition

CE imaging is also interesting in conjunction with ultrasonography (US). This modality, however, introduces additional challenges to the perfusion data analysis: first, US has a lower signal-to-noise ratio, when compared to MR and CT. Second, the data exhibit a non-linear enhancement behavior caused by the nature of the contrast agent, especially in combination with high resolution transducers, that can be seen as a noisy enhancement signal. Third, CEUS data are difficult to register, as the acquisition is performed freehand. It is almost impossible to keep the probe perfectly still, and deformations and off-plane movements add up to the effects of breathing and pulse. In such a scenario, even deformable registration methods cannot provide maximum accuracy. In addition, the typical analysis workflow consists of three stages: First, the examiner attempts to delineate regions of interest (ROI) according to their echogenicity in B-mode US (for brightness modulation: pixel intensities represent the strength of the echo) and to their perfusion enhancement, by looking at the cine-loop (animated image sequence) of the acquired CE data. This can be aided by additional parametric images. Then, ROIs showing abnormal enhancement patterns are selected, and the perfusion in these regions is characterized. The final stage normally consists of comparing the perfusion parameters of the selected regions with each other or with healthy

tissue (when possible), eventually leading to a diagnosis. A fourth challenge, within this workflow, is the procedure of delineating the ROIs, that has to be done manually. In certain cases, with large and irregular regions, like an organ parenchyma from which vessels should be excluded, this task can become tedious and time consuming.

The here presented interactive (and iterative) visual analysis approach for CE data exploration, analysis, and tissue classification is specifically tailored for the analysis of CEUS data, and addresses the four challenges described above in order to improve the CEUS perfusion exploration and analysis process.

This is achieved by introducing a data processing framework that extracts accurate enhancement parameters, which are more stable, in presence of noise and movements. It also offers a visual exploration mechanism to discover relationships in the anatomy with respect to perfusion, by using interactive similarity maps. Such maps are constructed using correlation information between each pixel pair with respect to the perfusion course, and can visualize clearly and precisely areas with perfusion patterns similar to the perfusion in a selected region, and also delineate other homogeneous areas. This method also allows to convert these similarity maps into selection masks, by thresholding them using a degree-of-interest function, and to easily combine such masks. Finally, different visualizations are used to enable an effective analysis and comparison of selected masks (elected as ROI), and assess the tissue condition.

The presented visualization pipeline consists of two main stages, plus one iterative stage, which are intended to gradually extract and visualize the perfusion trends. This pipeline is depicted in figure 3.1), where the perfusion metrics extraction part includes the first stage, while the visual analysis includes the last two stages.

To overcome the noise-related challenges (noisy enhancement and residual motion), the first stage extracts statistical enhancement information for each voxel (pixel/timestep) from its local spatio-temporal neighborhood. In particular, three enhancement metrics are derived: the mean enhancement value, the first and third quartiles of the values, and the percentage of enhanced values (values above a threshold divided by the total number of voxels in the neighborhood). As a result of this first stage, more robust enhancement curves are derived, as well as parametric maps of the perfusion parameters as described in the introduction, computed using the just mentioned enhancement curves (see figure 3.1(a,b)).

The second stage consists of an interactive visual analysis solution to identify and segment the regions of interest. To do so, the examiner starts getting an overview of the perfusion enhancement of the anatomy by looking at parametric maps, for example showing the area-under-the-curve parameter, the peak enhancement, or other expressive parameters. Each of these parameters only represents a selected aspect of the perfusion, and

parametric maps, singularly, appear not to outline the boundaries of suspicious regions with sufficient precision. Therefore, an interactive similarity map derivation is introduced. By selecting a pixel, a region, or a template curve shape, this method allows the classification of the entire dataset according to how similar the perfusion patterns are with respect to the selection (see figure 3.1(c)). To do so, Pearson's product-moment correlation coefficient (Pearson's r) is computed from the TICs as a similarity function. This computation is performed in real-time using the GPU, therefore, by simply hovering the pointer on the image, the similarity map gets updated interactively. Once the examiner has outlined an area of interest with the similarity map, the region can be saved immediately as a mask for later refinement. This procedure can be repeated to quickly obtain more masks, which then can be easily combined using set and morphological operators (see figure 3.1(f,e)).

In the third stage, the examiner elects the result of the processing operations on masks as ROIs, and, for each ROI, perfusion parameters are automatically computed. In this stage these ROIs can be analyzed and compared, with the system presenting the information about tissue perfusion for the selected ROIs, to eventually lead to the characterization of the regions.

This pipeline was designed to avoid a fully automatic but inflexible and error prone tissue classification solution. Instead, it keeps the domain expert involved in a semi-automatic, supervised classification process, aiding the characterization of the tissue, so that the result would benefit also from her or his knowledge. In too many situations, in fact, single approaches alone would lead to the wrong diagnosis (such as only TIC comparison in our case), while an expert can usually combine the information extracted from the data to achieve a more accurate diagnosis. A case study, demonstrating the usefulness of this solution is presented in section 4.1.

Further details on this contribution are given in Paper A.

Motion Correction. The presented approach does not include any motion correction stage, being based on the assumption that the image stack under investigation is already aligned. To achieve this, based on the data as coming from the US scanner, ImageJ [1] was used to register the datasets before the analysis. It uses the scale invariant feature transform (SIFT) [106] for feature extraction and, depending on the dataset characteristics, rigid registration or deformable registration using vector-spline regularization [5]. The prototype application is therefore not dependent on the motion correction approach adopted, and simply requires already aligned datasets. However, this work led to further work (Schäfer et al. [163]), specifically on the alignment of the CEUS image stacks. In this work, by making use of temporal regions, it has been possible to determine which frames could be

safely registered, and which instead should be discarded, thus improving the overall alignment of the stack.

3.2 Reformation and visual analysis of blood flow data

Tubular flows are studied in many fields, and in medicine the analysis of blood flow is crucial to detect possible pathologies such as aneurysms [50]. The visual exploration and analysis of such flow data can be challenging, due to the often varied geometry and topology of the flow, and due to a larger number of aspects of the data that are of interest, in particular in time-dependent flows like blood flow. These aspects include various scalar attributes, such as flow velocity, pressure, and vorticity, as well as derived attributes. On the visualization side, the variation of seeding structures, integration length, and the choice of a primitive type for an integration-based visualization, different time steps of the flow, and the variation of other visualization parameters are also aspects of interest. To enable an analysis that is based on several of such aspects, it becomes interesting to consider different views on the data as well as the relation between these views. Side-by-side visualizations [182] are one option to integrate different views of the data in one visualization, and are only limited by the overall available screen space. Moreover, being these visualizations simpler when compared to others, such as image fusion techniques [48] or coordinate multiple views [33], they are generally easier to read and interpret. Additionally, they can also be used to show the same attribute over multiple time-steps or visualized with different parameters, thus enabling alternative types of visual comparison. Last, they can also be combined with image-fusion techniques, leading to side-by-side visualizations of fused views. However, in terms of limitations, it takes significant additional space to juxtapose views, so the number of views that can be placed side-by-side is also limited. Second, relating separated views is not always a straightforward process, as they are not specified in a common reference frame anymore.

To solve this problem, a space warping solution to the side-by-side visualization of tubular blood flow datasets is presented here. In order to effectively juxtapose views of tubular flows, the concept of straightening the flow visualization (e.g., streamlines or pathlines) along the center line of the bounding tubular structure is introduced, as the centerline generally represents the main reference direction of the flow. Using this approach, multiple views can be aligned with one axis of the visualization and made parallel to each other along the straightened center line. With such a side-by-side layout it becomes possible to relate different views in the visualization in a straightforward way, having a common axis for the alignment and co-registration of different views of the data. In addition, this layout makes the visualization more compact, allowing to have more views at the

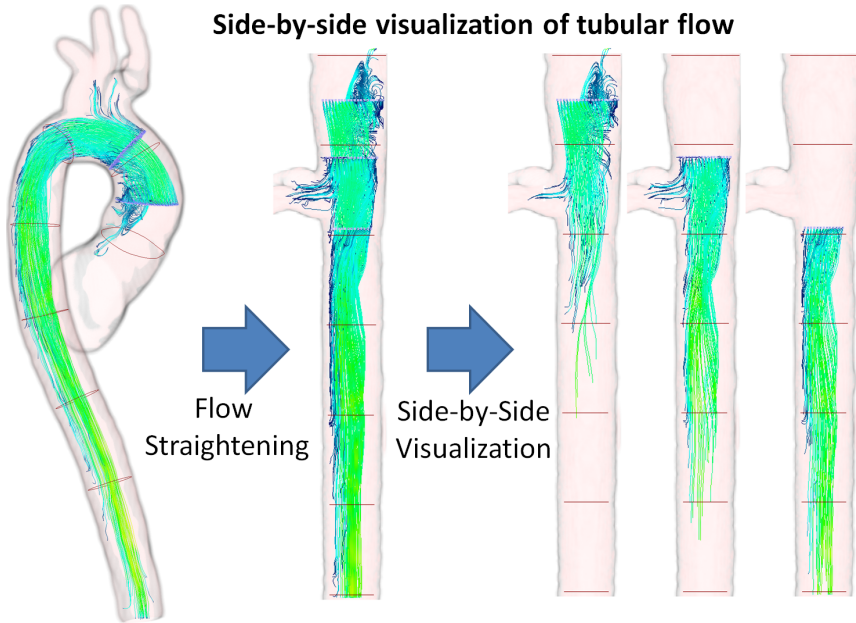


Figure 3.2: Overview of the proposed approach for realizing a side-by-side visualization of tubular flow (here aortic flow) based on straightening the flow domain. In the side-by-side visualization, the seeding structure has been varied in order to study different seeding locations

same time. This method can also be used to complement regular visualizations of tubular flows, in order to statically visualize multiple aspects of the data at once, including the time dependency. Last, it helps comparing different aspects of a dataset (such as different time points, or different descriptors), or even different datasets (as in population studies). Previous work [182] suggests that the question of whether or not to use side-by-side visualization also depends on the application at hand and on which advantages/disadvantages to prioritize, and our contribution addresses the cases where a side-by-side visualization is preferred.

The proposed method consists of two main parts: first, a combined technique for generating straightened visualizations of tubular flows, defined as vector fields on a Cartesian grid; then, a set of techniques to assemble these straightened views in order to create effective side-by-side visualizations.

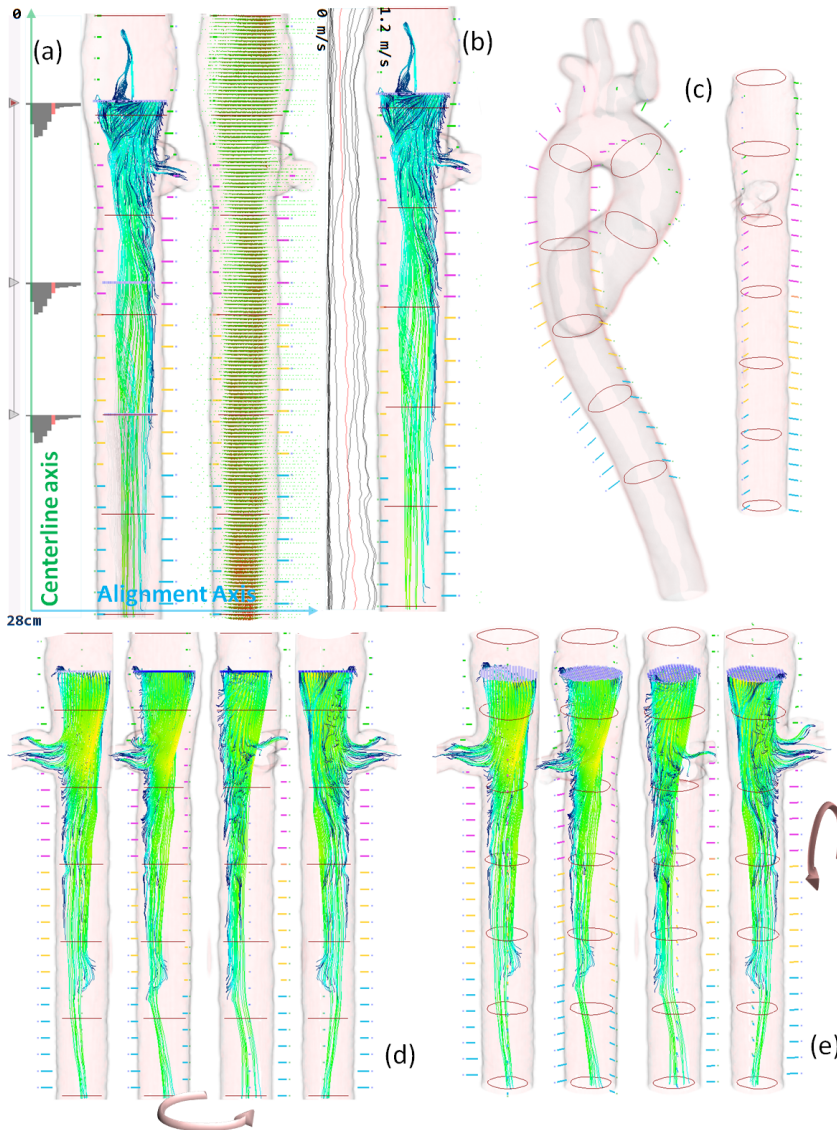


Figure 3.3: Design options for a side-by-side visualization of straightened tubular flow: straightened views should be aligned to one of the screen axes, and juxtaposed along the other. Informative visualizations, such as a line graph or a histogram of the flow magnitude can also be placed along the centerline, to provide quantitative information in addition. Orientation cues are useful: here a volume rendering of the physical context, with contours, is used to convey the physical space. Glyphs are also added to convey from which perspective the data is shown. Interaction with the visualization is constrained to allow only meaningful camera transformations: only rotations around the two axes used for the alignment are allowed

Conceptually, the first part can be realized in two different ways: by straightening the flow domain, and then performing the visualization mapping, or first performing the visualization mapping, and then straightening the geometry representing the visualization itself. The advantage of the first approach is the simplicity of producing flow visualizations: once the vector field is reformed, any existing flow visualization technique can be used without modification. This also avoids performance penalties when compared to visualizing the original data. On the downside, the vector field reformation process sometimes introduces numerical inaccuracies. Reforming visualization cues, on the other side, produces an exact straightening of the visualization primitives, at the cost of a higher computational complexity. Moreover, this approach requires a tailored algorithm for each flow visualization technique to be realized. In order to combine the best of both approaches and to avoid the mentioned drawbacks, a hybrid scheme was developed, that renders the straightened vector field data during user interaction, to keep the system interactive. The second approach is then used to produce an as accurate as possible straightened visualization on demand.

The second part of the method consists of techniques to assemble the final side-by-side visualization, paying attention to how to combine the views. Here, first, the straightening axis in the views is aligned to one of the screen axes, in order to facilitate the juxtaposition and the alignment of several views. Having the reformed centerline aligned to one of the screen axes has the additional advantage that it minimizes the space between the different views. This alignment also allows to combine visualization of the actual data (such as standard flow visualization techniques) with more abstract visualization techniques, such as line graphs, plotting selected quantities along the centerline (see figure 3.2 Right (a,b)). With such setup, it becomes also possible to use the centerline axis as navigational tool: it can be used for operations such as cross-section placement and movement, and length measurement (see figure 3.2 Right (a)). Second, special attention must be paid also to conveying the shape of the reformation, in order to let the viewer easily relate positions and directions in the reformed view to positions and directions in the original space. The presented method uses two kinds of orientation cues. The primary cue is the rendering of the reformed tubular structure around the flow as its spatial context. To do this, volume ray casting of the straightened context is performed, instead of rendering the extracted isosurface. This allows to perform fast and correct depth-buffer based alpha blending with the integrated geometric primitives, such as streamlines, in a single (modified) ray casting pass, without the need of performing expensive multi-pass rendering techniques, such as depth-peeling. In addition, a number of “i-shaped” glyphs are placed along the projection of the normal and of the binormal onto the flow bounding structure (see figure 3.2 Right (c)). The body color

of these glyphs encodes the distance from the beginning of the centerline, while the dot color encodes the projection axis (green dot = glyph above the normal, blue dot = glyph above the binormal). This helps the user to orient and understand from which viewpoint he or she is looking at the flow. These glyphs, in combination with a specified number of isocontours of the tubular structure, also help the user relating a region along the centerline “axis” between the conventional view and the reformed side-by-side visualization.

The proposed side-by-side layout also introduces some challenges in the interaction process with the visualization. Rotating the visualization with the classical joystick or trackball paradigms, in particular, might become unfeasible. For this reason only 2 rotation methods are enabled: per-view rotation around the centerline axis, and global rotation around the other screen axis (see figure 7). This method proved to allow thorough exploration of the straightened data, while, at the same time, being intuitive and error-proof, preventing the user to “get lost” while interacting with the visualization. A case study, demonstrating the usefulness of this solution is presented in section 4.2. Further details on this contribution are also given in Paper B.

3.3 Aggregated visual analysis of aging data

Cohort studies in medicine [169, 198] are becoming increasingly common, partly due to the availability and recent improvements in medical imaging technologies. Such studies are used to evaluate medical hypotheses in a sample, either healthy or presenting a common pathology, in order to gain a better understanding of healthy aging and of the development of pathological changes. Cohort study datasets are often acquired over longer time periods and follow strictly defined protocols. Normally, they are designed to deliver data which, later, can be the basis for evaluating further sets of hypotheses. However, while there are means to evaluate specific hypotheses, based on such cohort study data, often involving accordingly designed data extraction, transformation, and fusion approaches, there is a lack of technology that would support the flexible and open-ended exploration of such data, mostly because of its high heterogeneity. For certain aspects, in addition, there are both quantitative abstract measures, and physical (anatomical) data. While the analysis is often performed on the quantitative measures, it also occasionally becomes necessary to fetch and inspect the related anatomical data, which can, for example, explain data outliers, or to map measures to their anatomical context.

Integrating all the available data within one visualization tool that allows to seamlessly combine them on demand is expected to help the experts to explore heterogeneous cohort study data more easily, to allow for

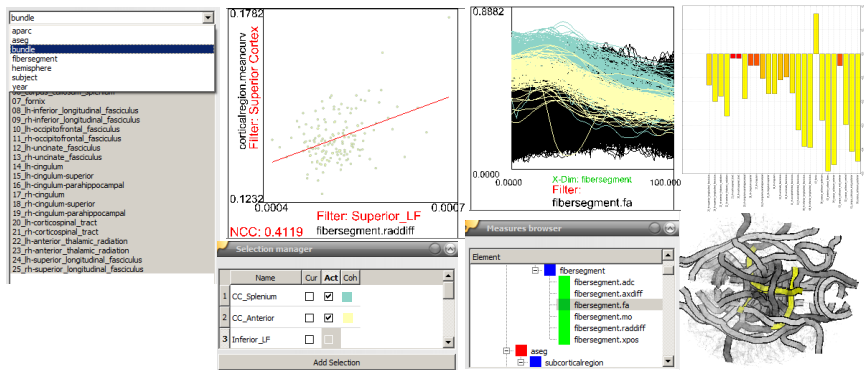


Figure 3.4: Screen-shots of the prototype of the proposed model. The Measure Browser lets the user drag desired measures into a view, the Selection Manager allows to add new selections, activate them, enable one of them for editing, and drag them into views, to be used as filters. The Dimension Brusher (leftmost) enables to slice the data cubes in the data collection, while the other views can be seen as projections of the data, and allow a more advanced definition of the selections, by means of brushing ranges of measures. Finally, the fiber model view (bottom right) represents a selection in the anatomical context using a brain model

an improved hypothesis generation, and, not at the least, to speed up their current research workflow.

When designing a solution for a visualization of such data, there is a dual goal: on one side, it is important to enhance the data exploration process, in particular in those aspects not yet investigated, and possibly provide enough information to generate new hypotheses and subsequently verify them. On the other side, it is also important to enhance the process of hypotheses verification by easing the extraction of the aspects of interest from the dataset, and to investigate the relation between them.

Storing, accessing and manipulating the data acquired with such studies in a fast and flexible way is the first and perhaps the biggest challenge in designing an interactive visualization system targeted at this problem. Organizing the data in a relational database, similarly to Steenwijk et al. [169], is probably the most straightforward solution at hand, and probably also the easiest to design. However, the database schema is bound to the particular structure of a specific study, and has to be redefined for different studies, as well as the logic for data access, thus showing lack of flexibility. Moreover, a relational database might not provide the required performance to enable an interactive exploration, depending on the dimension of such (generally large) data.

With Polaris, Stolte et al. [170] showed how data can also be organized for visualization as an n-dimensional data cube, in data warehousing called OLAP cubes (for On-Line Analytical Processing) [58]. In OLAP

data analysis this strategy is used in order to enable fast processing of large amount of data.

OLAP cubes are constructed using categorical attributes as dimensions, while quantitative numerical values are stored as measures. The dimensions and measures can be thought as independent and dependent variables, where dimension coordinates are used to access the measures. In practice, after assigning an order to the dimensions, a data cube can be implemented as an in-memory n-dimensional array. This allows, for example, a faster data access, as compared to keeping the data in a relational database.

The proposed solution builds on a model that organizes the cohort study data in a collection of data-cubes. This model includes associated operations to aggregate these partially overlapping data-cubes, link them together, and perform filtering and selections of them. With this model it is possible to automatically compute the common dimensions of two or

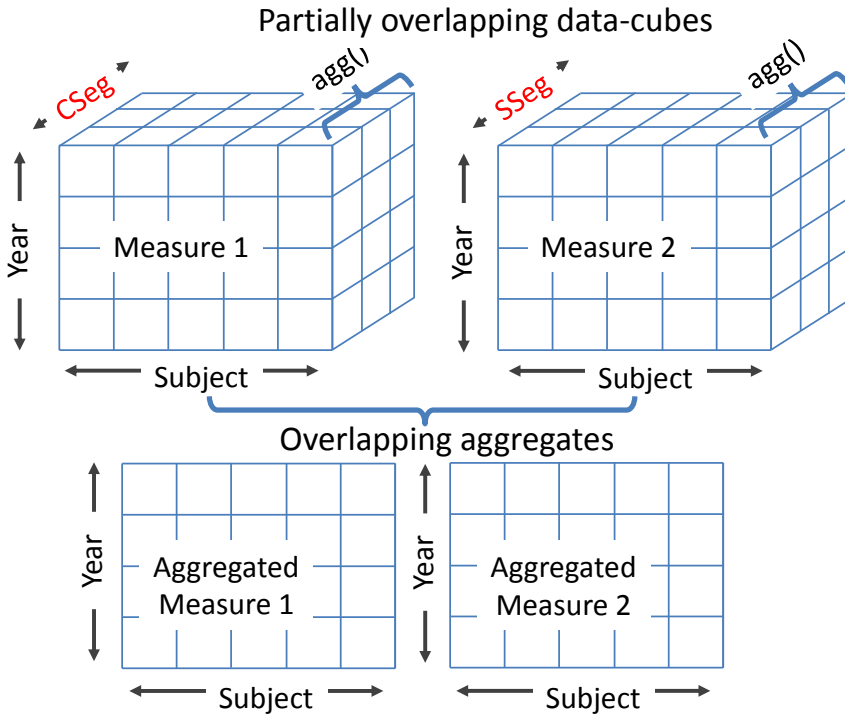


Figure 3.5: Projecting two three-dimensional measure cubes (e.g., thickness of cortical regions and volume of subcortical regions) on the common dimensions. The dimensions which are not common (in red) are processed using a statistical estimator (e.g., average)

more measures by simply intersecting the dimensions set of the measures, without having any prior knowledge of the relations between measures (as necessary when using a relational database model for the data, when the system would need to know about the database schema, together with complex logic for performing the operations). In the presented model, when multiple measures are combined in a visualization (e.g., in a scatterplot, or a parallel coordinate view), each measure is automatically aggregated (or projected [170]) along those dimensions not belonging to the intersection (as illustrated in figure 3.5). Along with the model, a prototype system has been developed, where a drag-and-drop interaction model has been included, so that it is sufficient to drag the desired measures into a view to obtain the aggregation (if necessary) and the visualization. The system lets the user also toggle which of the common dimensions should be kept during the aggregation, and which not, thus performing a sort of roll-up operation, to change the level of detail. The difference to a classical roll-up operation is that there is no hierarchy in the dimension structure. Therefore it would be possible to roll-up independently any dimension in the set. In addition, brushing is used to perform selections on the data. In order to deal with the additional challenge of having only partially overlapping data cubes, in the presented model, a brush on one cube is propagated to all the other cubes in the collection that share dimensions with the brushed one, by first computing a projection of the brushed entity using the common dimensions with the other ones. This projection of the brush is performed using the max operator, which eventually tags the items in these projections that have been created out of at least one tagged item. However, it is also possible to compute the percentage of items that have been tagged using the specific common coordinates (instead of the max), resulting in a non-binary tag. Finally, in the presented model, selections can be used also for a second purpose: since most of the views are built upon aggregated data-cubes, this aggregation can be steered, or filtered, using a selection. By setting a selection as aggregation filter, the aggregation is performed only using the items that are selected in the filter. A case study, demonstrating the visual analysis of a cohort study dataset on brain aging is presented in section 4.3. Further details on this contribution are also given in Paper C.

3.4 Guided exploration of follow-up ultrasound examinations

Ultrasonography (US) is a powerful and inexpensive medical imaging modality, and one of the most used worldwide in clinical practice. When there is the need to communicate the examination further, for example from the radiologist to the surgeon, the acquired data can be saved for later reviewing. Data exported by 2D US scanners consists of annotated, and often printed, still images, as well as video sequences containing all the

acquired US images, captured at a certain frame rate during the examinations. During certain kinds of US examinations, the physician scans several different anatomical structures, without focusing exclusively on one part of the anatomy. In such situations, as, for example, during abdominal examinations, simple snapshots of US slices may lack contextual information. They may also miss some important information that the examiner may have scanned, but not recognized and thus stored, in the first place. Stored video sequences contain all the imaged data, and, to a certain extent, prevent the loss of important information about structures of interest or their context. Unfortunately, such video data lacks higher semantic information, present during the live examination, such as the 3D position and orientation of the US planes, knowledge of which anatomical structures are imaged, neighboring anatomical structures and scanning direction. Therefore it is challenging and time-consuming to review entire ultrasonographic sequences after the examination, especially if the review is performed by another physician, without first hand knowledge of the examination. Moreover, videos of US data, lacking semantic annotations such as the imaged anatomical structures, require the examiner to go through all the video sequences, during the reviewing process, to find the images with the structures of interest, taking (potentially) long time. This becomes even more evident when not only one, but several examinations of the same patient have been performed. In this situation, many video sequences, containing 2D images of the patient at different points in time, would require extensive inspection in order to identify the frames imaging the region of interest in every cine-loop and detect changes or progression of diseases.

To solve these problems, the goal of the the pipelined approach presented here is to enrich the US data with semantic information about the content of each image in the video sequences. Being able to input to a visualization system the data and the information about what the data contain, the examiner could be guided, by the system, during the data exploration and reviewing tasks.

The key concept in the pipelined solution presented is to compute the degree of interest (DOI) for each US image with respect to the anatomical structures the examiner is investigating. This is done by considering a so called DOI volume, created out of volumetric representations of the anatomical structures of interest, that describes how much a voxel belongs to the structure(s) of interest. In a following step this annotation of the space is combined with the US images. The output of this step is an aggregated measure of the DOI for each image in the US sequences, telling how many pixels in the image belong to the structures of interest. This measure can be seen as a measure of the importance of each US images with respect to a selected focus structure. Once this measure has been computed, it can employed through appropriate visualization methods to guide the

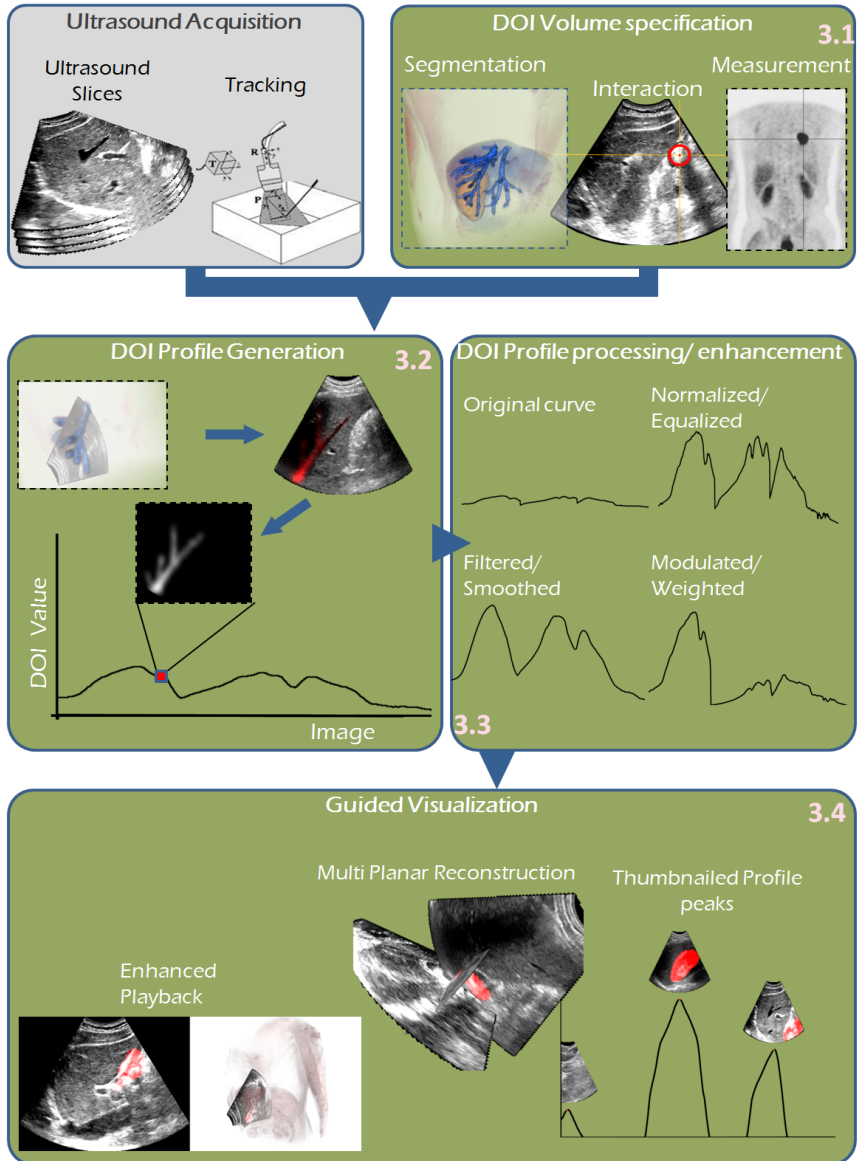


Figure 3.6: Schematic illustration of the presented pipelined solution, consisting of four stages

examiner to the relevant images or video subsequences. The methods that are employed in this work consist of an enhanced timeline bar, used for navigation, that depicts the importance of the frames as a function, and

contains clickable bookmarks to the points in the videos where the structures of interest are very visible. In this way, subsequences in multiple acquisitions can be quickly accessed and easily compared. The enhanced timeline bar is then complemented by a fused view of each frame within its context consisting of the volumetric structures of interest, to get a clear idea from which position/orientation the image was acquired. Further details on this contribution, including the data acquisition requirements, are given in Paper D.

CHAPTER 4

Demonstration Cases

4.1 Visual analysis of focal liver lesions in contrast-enhanced ultrasound data

The method described in section 3.1 was implemented using the OpenCL computing framework, to enable interactive perfusion measure extraction and computation of the correlation. For this reason, the prototype was run on a workstation with an nVIDIA GeForce GTX280 graphics card, for which nVIDIA provides drivers supporting OpenCL. With this method, six CEUS datasets have been analyzed, imaging focal liver lesions. The resolution of the data containing the liver and the right kidney was 240×240 pixels, acquired at approximately 9 frames per second. These datasets are representative for their respective diagnostic field, concerning spatial and temporal resolution, and also concerning the observed enhancement behavior. From a performance point of view, this setup allowed interactive exploration of the available data without problems using standard settings. For such image resolution, it has been possible to notice, during the analysis, that the neighborhood diameter of the perfusion metric extraction stage should not exceed the size of 7–9 pixels, to prevent information loss. In the case of liver lesions, the parameters that have to be evaluated in order to assess the type of the lesion [149] are:

- the enhancement dynamics, that allow to assess the type of vascularization in the lesion
- the homogeneity of the enhancement in the lesion (homogeneous enhancement versus areas with different perfusion dynamics)
- the shape of the lesion

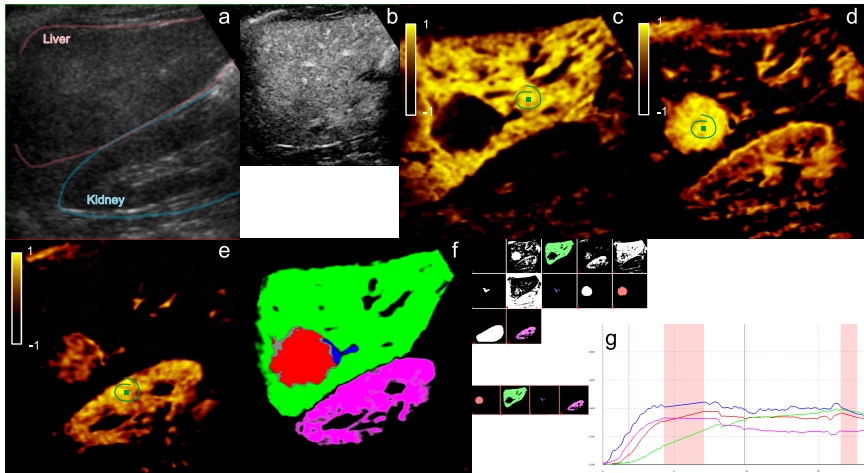


Figure 4.1: Interactive visual analysis of a dataset with a liver lesion. One B-Mode image showing the imaged anatomy (a). One contrast image from the dataset, showing diffuse enhancement, where only vessels are highlighted (b). Similarity map for a point specified on the (presumably) healthy liver parenchyma, in green. The healthy tissue highlights, and also delineates other structures in the liver, such as the vessels and the lesion on the left (c). Similarity map for a point specified on the lesion. The lesion highlights entirely (d). Similarity map for the kidney (e). ROIs defined on the healthy tissue (green), lesion (red), lesion feeding vessel (blue) and kidney (purple). In grey the uncertain area. (f). TICs for the four ROIs. The lesion exhibits a kinetic similar to the feeding vessel, much earlier (TOA and TTP) when compared with the healthy tissue, similar peak enhancement, and almost iso-echoic behavior in the mid phase (g).

In this case study, the patient suffered from flank pain and, from a first Ultrasound examination, appeared to have several liver lesions. So each one of them was separately imaged in a dedicated perfusion examination. What follows is a description of the analysis of one of the scans, which is also representative for the other cases studied. The sequence contains 257 timesteps, that, acquired at approximately 9 frames per second, amount to a total duration of about 30 seconds. The sequence is cut, in time, before the contrast is completely washed out from the area, thus containing only the arterial phase. This, however, provides enough data to assess the vascular structure in the lesion, together with its shape, echogenicity, and homogeneity. The results of the visual analysis are illustrated in figure 4.1.

After the data was loaded, the perfusion metrics were automatically extracted using the default settings for the neighborhoods size (diameter of 5 pixels in the spatial dimensions and 3 timesteps in the temporal dimension). The system also provided an enhancement profile for the whole image, to automatically identify the global *Time-Of-Arrival* (TOA) of the contrast (TOA in the regions enhanced first). The starting timestep for

the analysis was then set to the global TOA. Next, all the frames were inspected to identify those frames with alignment errors, so that they could be excluded from the analysis, and the values interpolated using neighboring frames. In figure 4.1(g), the red bands on the plot represent timesteps with excluded frames and interpolated information. After this procedure was completed, the different parametric maps provided by the system were visually inspected, to identify the regions with the characteristic perfusion (figure 3.1(b)). These maps highlighted the liver parenchyma, part of the kidney parenchyma – that usually has a fast wash-out and thus a small *Area-Under-the-Curve* (AUC) – and, most prominently, the vessels as well as a spherical region in the liver parenchyma not consistently defined among the maps. So, a pixel on the (presumably) healthy liver parenchyma was selected, in order to obtain a similarity map for the healthy tissue (figure 4.1(c)). This similarity map for the healthy area was converted into selection, and used as reference (figure 4.1(f,g) (green)). In the similarity map of the healthy tissue, the non-consistently defined region on the left gained a much sharper contour, as it was very different in perfusion. So this area was investigated by selecting a pixel, and obtaining the similarity map for what turned out to be a lesion (see figure 4.1(d)). By doing this, the lesion was precisely highlighted and immediately converted it into a selection. A rough lasso selection around it was defined and intersected with the similarity-based selection to exclude non-related areas (figure 4.1(f) (red)). At this point, a precise segmentation of the lesion was obtained, and its perfusion information, automatically computed by the system, could be compared with the other regions segmented (healthy parenchyma and artery).

In this way it was possible to assess the composition of the lesion (single compound), the shape (regular) and the size (diameter of about 3cm). Compared to the healthy parenchyma, the lesion enhanced earlier (*Time-Of-Arrival* and *Time-To-Peak*), and in the late phase it was almost iso-echoic (figure 4.1(g)). But the peak enhancement was lower and in general the wash-out began slightly earlier, already in a 30 seconds sequence, which indicates the absence of the portal phase. These features should characterize the lesion as a hepatocellular adenoma (benign) [49, 149]. After the patient also underwent a liver biopsy, the diagnosis was eventually confirmed.

4.2 Visual analysis of aortic flow

To demonstrate the utility of the method described in section 3.2, a prototype was developed, and different visualizations of aortic flow were created. The data came from time-resolved 3D Phase-Contrast MRI (PC-MRI) scans, which proved to be effective to image the blood flow in the human

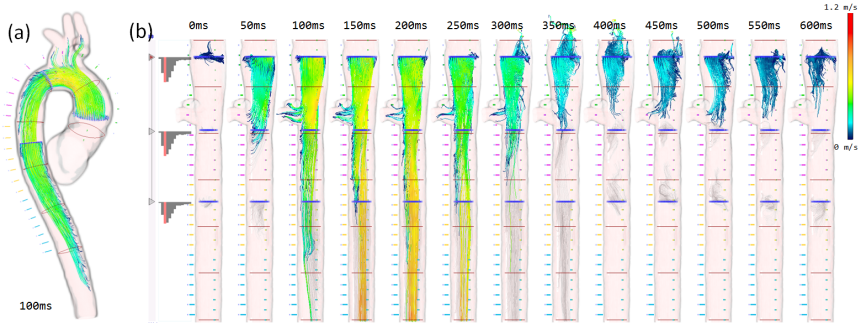


Figure 4.2: (a) A timestep of an aortic flow dataset in its anatomical context, rendered using a conventional streamline visualization. (b) Side-by-side visualization of the straightened vector field, showing all the timesteps juxtaposed. The streamlines traced from the first seeding plane are rendered in focus, and the others in grey as context.

body [15]. These visualizations were kindly evaluated by the the Cardiovascular MRI Group at the University Medical Center Freiburg, Medical Physics department, which provided feedback on the usefulness of the method (reported below), in order to understand how possible end users would benefit from this technique. The dataset visualized is a vector field of the blood flow in a human aorta, specified on a Cartesian grid with a resolution of $192 \times 144 \times 24$ voxels in x , y and z respectively, and containing 13 time steps acquired at a time resolution of about 50 milliseconds. The spatial resolution of the scan is [1.67mm, 1.67mm, 3.5mm] in x , y and z , for an imaged volume of $32 \times 24 \times 8.5$ cm. To simplify the handling of the significant anisotropy of this dataset, the dataset was upsampled to an isotropic grid. The aorta was segmented in a similar manner as van Pelt et al. [180], and the centerline of the arterial wall was extracted. The centerline was subdivided in segments of voxel-length to minimize resampling artifacts, and the straightening was performed using quads with a side length of approximately 7.5 cm, with a transversal resampling resolution of 49×49 voxels (approximately the same resolution of the data).

In the prototype, streamline and pathline tracing were implemented on the GPU, using geometry shaders [180]. Abstract visualization techniques such as line graphs and histograms (of averaged velocity) were also added, showing also how simple it is, with this method, to combine classic flow visualizations with other data visualization methods in an intuitive way. Additional flow visualization methods could, however, be also used with the prototype.

Examples of the visualization produced with the presented method are shown in figure 4.2, 4.3 and 3.2. Figure 4.2 shows all the timesteps in the dataset, side by side, using streamlines with a fixed seeding grid and

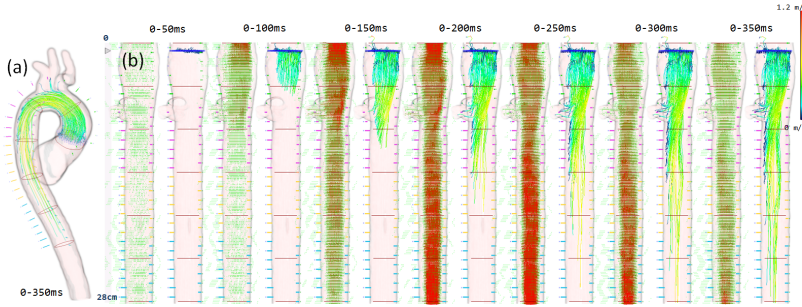


Figure 4.3: Timesteps from 0 to 6 of the aorta dataset, visualized with pathlines and glyphs illustrating the vector field. Each pair of views shows the glyphs rendering of the vector field at the last time point stated on top, and the pathline integration from time 0 to the last time point.

3 seeding planes, presenting them in a time-lapse manner. In figure 3.2 (left) a single timestep is investigated, by separating the seeding body into different views, thus preventing streamlines related to different seeding planes from overlapping. Figure 4.3 shows the evolution of pathlines integration, from timestep 1 to 7, side by side with the vector field at each timestep.

The evaluation from the Cardiovascular MRI Group at the University Medical Center Freiburg, Medical Physics department, is composed of general impressions and of answers to specific questions asked by the authors. In general, the reformatting of the aorta has been seen as potentially useful to compare some hemodynamic parameters (such as wall shear stress or pressure differences), also across a population. However, in this case one would need some kind of aortic atlas, and then map the dataset onto this atlas. There was also some uncertainty about how the visualization would look in presence of an aneurysm or a stenosis. The group also believed that medical personnel is more accustomed to seeing the blood flow in its original context, and would, therefore, require a certain training in order to profit from the proposed method.

The specific questions that were asked to the Cardiovascular MRI Group in Freiburg contemplated what kind of visual comparison are they interested in, whether this approach would ease the comparison of integrated lines in the aorta, and what are other parameters typically investigated. Then also whether they think that physicians would profit from this technique as well, and what do physicians generally look at in such data. According to their answers, at the present they do not perform that much comparison visually, but the presented approach could be useful to compare hemodynamic parameters, while other typical parameters of interest along the vessel are helicity and vorticity. The presented approach has

been seen as definitely easing the comparison of integrated lines from their point of view, but, from a medical point of view, physicians are currently very accustomed to the original shape of the vessel. Last, visual features of interest, from a medical perspective, are helices, vortices, and retrograde flow at late timepoints. From this evaluation it is possible to conclude that domain experts could profit from this flow straightening techniques, but some training is necessary. However, there have been other cases of reformation techniques which required a certain learning, before being embraced in the clinical routine, such as the curved-planar reformation of the human vessel tree [75].

4.3 Visual Analysis of Heterogeneous Aging Data

One major goal of the work presented in section 3.3 was to have a solution for enabling the explorative visualization and analysis of data that was acquired as part of a longitudinal study on cognitive aging. During this study, more than 100 healthy individuals (mean age 60.8 (7.8), 65% females at inclusion) were recruited through advertisements in local newspapers. All the participants were interviewed before inclusion, to exclude those reporting previous or present neurological or psychiatric disorders, a history of substance abuse, or other significant medical conditions. The neuropsychological evaluation confirmed that the participants showed no symptoms indicating mild cognitive impairment (MCI) or dementia. Each participant was examined twice, first in year 2004/2005, and then in 2008 (a third wave is at the moment being completed). The participants were subjected to neuropsychological testing, multimodal MR imaging and genetic analysis (not used in this study). The result of each examination consisted of data on white matter fiber integrity, as expressed by fractional anisotropy computed from diffusion tensor imaging (DTI), cortical and subcortical gray matter measures, automatically calculated from structural MR images, and a number of neuropsychological tests, including the California Verbal Learning Test–Second Version (CVLT-II), the Color–Word Interference Test (CWIT), the Digit Symbol Substitution Task from WAIS-R, and the Mini Mental State Exam (MMSE). In addition, multiple quantitative measures for the white matter fiber bundles and the gray matter segments were extracted: different anisotropy measures for the bundles, and volume, thickness and area measures for the brain regions. To summarize, each examination (per subject and year) consists of:

- white matter fiber bundles with anisotropy measures. Each individual fiber was divided into 100 segments of equal length.
- gray matter cortical and subcortical regions with quantitative measures for each region.

4.3. Visual Analysis of Heterogeneous Aging Data

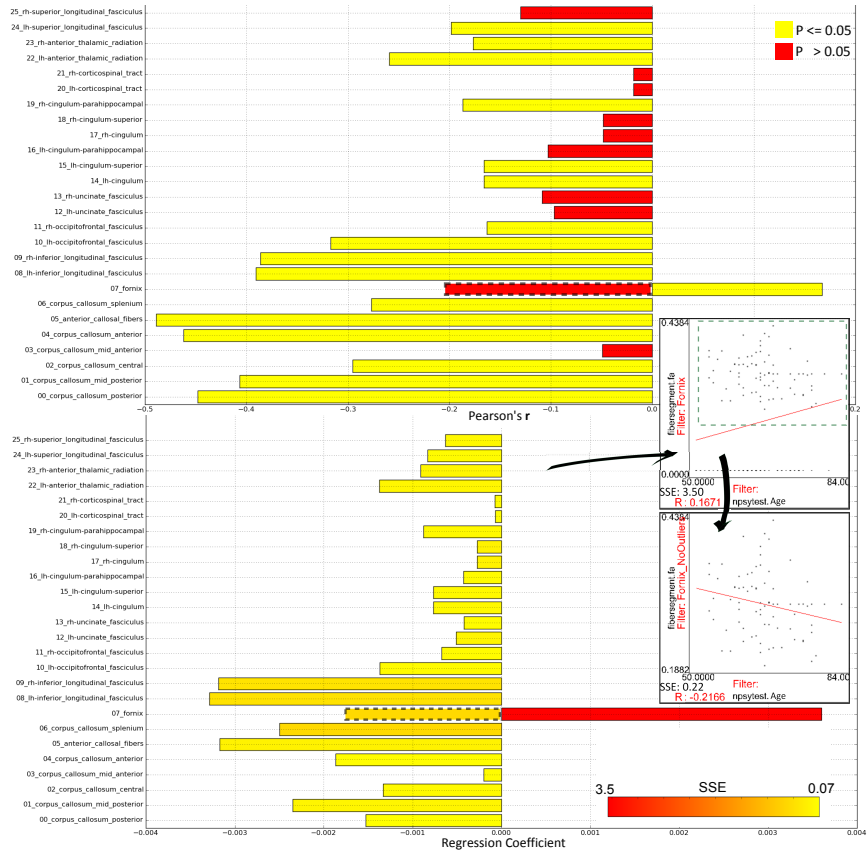


Figure 4.4: (top) Visualizing the correlation coefficient between age and fractional anisotropy of the fibers across all subjects, years. The FA measure is filtered by automatically iterating over a chosen dimension, in this case fiberbundle (thus iteratively slicing the measure). Therefore, each bar in the bar chart represents the correlation referred to a specific coordinate in the fiberbundle dimension. (bottom) The same type of visualization representing the regression coefficient instead. (right) Scatterplots related to the fornix, before and after excluding wrong values.

- scores from different neuropsychological tests.

One specific challenge with respect to these data is that their domains overlaps only partially. For example, how should one combine, in a scatterplot, fractional anisotropy, specified for each segment of the fiber bundles, with thickness of the cortex, available for each cortical region? The model/prototype presented in section 3.3 was developed to specifically address this challenging partial incompatibility of the data domains.

To demonstrate the utility of the presented solution, a case study on these data was carried out to investigate which fiber bundles show a decline in fractional anisotropy with age, and which do not. Subsequently, the prototype system was used to look for evidences of known hypotheses of age related white matter changes in the sample under investigation. The explorative investigation of the relation between anisotropy decline and age started by looking at the correlation coefficient of each fiber bundles fractional anisotropy with age, as well as the regression coefficient. The system estimates these statistics for the chosen measure by iterating over a user specified dimension, in our case *fiberbundle*. These estimates are presented in two bar charts, shown in figure 4.4. In these charts it is easy to spot one fiber (fornix) that goes against the general declining trend, also showing a bad fitting (sum of squared residual, SSE). The data related to this fiber was brought up in a scatterplot (figure 4.4, top right), where showing several zero values, probably due to missing data. Since these missing data should be removed, a brush on the scatterplot was performed, in order to exclude the incorrect values. This led to opposite results for this bundle (figure 4.4, bottom right), in line with the overall declining trend (these results are sketched with a dashed line in the barchart of figure 4.4). Finally, it was possible to notice two specular fiber tracts, left and right occipitofrontal fasciculi, that show not homogeneous anisotropy values, with the right one showing a more pronounced anisotropy decline.

The second part of this case study was an attempt to confirm or reject three hypotheses that were already statistically examined in previous work [172, 189]:

- The increased anisotropy decline in the anterior callosal fiber (CC-Anterior) with aging, as compared to the posterior portion of the corpus callosum, called splenium (CC-Splenium).
- The higher sensitivity of superior fibers (Superior-LF) to anisotropy decline, as compared to inferior fibers (Inferior-LF).
- The resistance of the cortico-spinal tract to anisotropy decline.

To do so, the fibers under investigation were initially selected, and these selections were used as filters in scatterplots opposing the age of the subjects to the fractional anisotropy (FA) of the fiber segments in their brains. In these scatterplots, shown in figure 4.5, each point represents a single subject examination, while the other dimensions are aggregated for each of the measures. In the case of FA measure, this aggregation was filtered using the selections above. The system automatically computed the Pearson's r value of the two measures (one aggregated using the filter), the p -value, which, in this case, is below 0.05 except for the corticospinal tract (that, therefore, does not show a correlation that is statistically significant),

4.3. Visual Analysis of Heterogeneous Aging Data

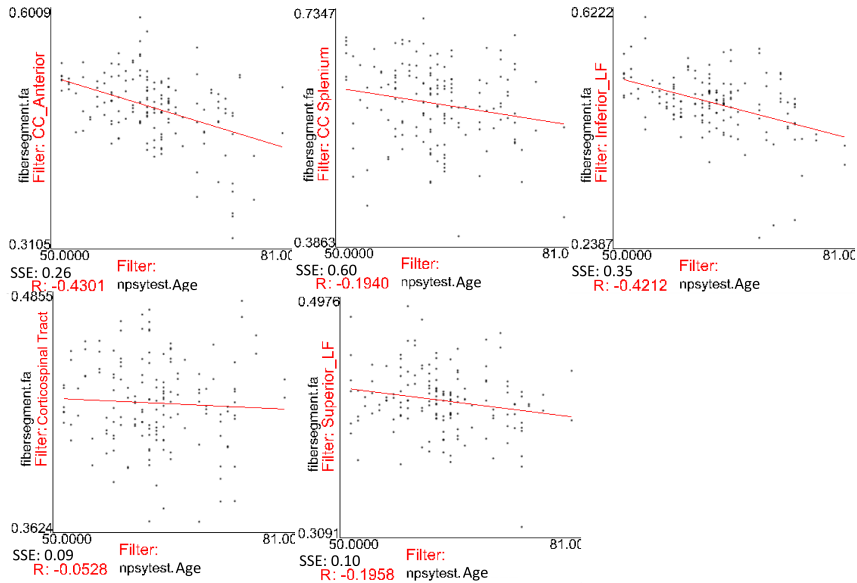


Figure 4.5: Age opposed to Fractional Anisotropy (FA) for each examination (subject, year). In each scatterplot, the FA value has been aggregated (across segments and bundles) using a different filter, as labeled in the views. Top left and top right show a stronger negative correlation of the FA plotted against age, while top center and bottom center show a weaker negative correlation. Bottom left shows almost no correlation of FA change with age for the corticospinal fiber tracts, which confirms previously published studies, and can be used as control. In each plot: R is the correlation coefficient, SSE is the sum of squared residuals of the regression analysis.

and the regression line. The regression analysis also provides the regression coefficient and the sum of squared residuals (SSE) as a metric of the goodness of fit.

From these plots, it is possible to confirm that the spinal tract is indeed relatively insensitive to the age effect. They also show that the posterior portion of the corpus callosum is less prone to the age effect, compared to the frontal portion. However, in contrast to the hypothesis, superior fibers were less prone to age effect than inferior fibers, which could imply that language function stays normal in the sample, but visual integration might decline.

CHAPTER 5

Conclusion and Future Work

The technological advancements in medical imaging allow to capture an increasing amount of patient-specific physiological information. Compared to structural anatomy data, these physiological data add complexity to the overall picture available for a patient. Due to this increased complexity, and to added aspects that are not always directly mappable to screen images (as, for example, the time course of a process), there is the need for solutions that are able to represent physiological information in an understandable manner.

In order to improve the comprehension and analysis of data that image selected aspects of physiology, namely perfusion, blood flow and aging, the work presented in this thesis made use, and often extended, different visualization technologies. From the case studies, and from the evaluation that has been obtained, it is possible to conclude that IVA methodologies are useful for bringing up these aspects in the data that are not directly mappable to pictures. Furthermore, these methodologies proved to be also suitable to analyze heterogeneous data. In this particular problem, different statistical methods have also proven to be very effective in condensing the information into meaningful quantities.

The evaluation gathered from domain experts also shows that, in certain cases, carefully designed alternative methods for data representation can provide advantages to unveil relations in the data otherwise difficult to see. This was the case of straightening methods applied to blood flow visualizations, that were used to bring different views in a common space of reference. Together with additional illustrative techniques used to link the new representation to the original one, this enabled a more effective comparison of aspects otherwise harder to perceive, such as the time dependency.

In future work, there is a plan to combine more extensive statistical solutions with IVA techniques, to fully reveal the relations in large and complex heterogeneous dataset. In addition, exploring the applicability of flow deformation and straightening methods for providing informative overviews similar to those proposed by Borkin et al. [17] would be fruitful.

However, despite the advancements in the field produced by the work presented in this thesis, the visualization of physiology data remains a wide, and partly unexplored field. In future, we can expect that aspects that are currently not addressed by visualization, also due to lack of detailed enough data, will be considered. Examples are the multi scale aspect of physiological processes, and the integration of physiological models with patient specific information acquired, for example, through imaging. These goals were also seen by Ayache et al. [7], when defining the Virtual Physiological Human project, in order to reach the creation of patient-specific physiological models. To achieve this we should also expect that physiology visualization will leave the corner of scientific visualization, to include technologies from other fields, such as information visualization, illustration, and visual analytics. A step in this direction can be found in the work presented in this thesis, where the visualization of physiology has been addressed using also methods coming from outside the classical scientific visualization. Finally, we should also expect the visualization of physiology data to advance arm-in-arm with medical imaging. In the future, it will become possible to capture new extraordinary aspects of physiology, and visualization will be essential to communicate these aspects to humans.

Part II

Scientific Results

Interactive Visual Analysis of Contrast-Enhanced Ultrasound Data based on Small Neighborhood Statistics

Paolo Angelelli¹, Kim Nylund²,
Odd Helge Gilja^{2,3}, Helwig Hauser¹

¹Department of Informatics, University of Bergen, Norway

²Institute of Medicine, University of Bergen, Norway

³National Centre for Gastroenterologic Ultrasonography, Haukeland University Hospital, Bergen, Norway

Abstract

Contrast-enhanced ultrasound (CEUS) has recently become an important technology for lesion detection and characterization in cancer diagnosis. CEUS is used to investigate the perfusion kinetics in tissue over time, which relates to tissue vascularization. In this paper we present a pipeline that enables interactive visual exploration and semi-automatic segmentation and classification of CEUS data.

For the visual analysis of this challenging data, with characteristic noise patterns and residual movements, we propose a robust method to derive expressive enhancement measures from small spatio-temporal neighborhoods. We use this information in a staged visual analysis pipeline that leads from a more

local investigation to global results such as the delineation of anatomic regions according to their perfusion properties. To make the visual exploration interactive, we have developed an accelerated framework based on the OpenCL library, that exploits modern many-cores hardware. Using our application, we were able to analyze datasets from CEUS liver examinations, being able to identify several focal liver lesions, segment and analyze them quickly and precisely, and eventually characterize them.

A.1 Introduction

Contrast-enhanced imaging (CE) is an increasingly used approach in medicine. A contrast agent tracer is injected in the blood stream of the patient before the imaging process. The contrast agent increases the enhancement in the images, which makes it easily detectable. It can be used to determine the blood concentration in the imaged tissue at specific time steps. This makes it possible to analyze the *perfusion kinetics* of blood in tissue, which correlates with the level and type of tissue vascularization [116]. This non-invasive imaging modality is increasingly used in ischemic stroke assessment and oncologic diagnosis; In oncology, for instance, the presence of abnormal vascularization can be an indicator of a malignant lesion. Changes in blood perfusion kinetics can therefore be used for the identification and diagnosis of possibly malignant tissue in parenchymatous organs, such as the liver [149], breast [194], and pancreas [85].

To perform the diagnosis, the imaged data can be analyzed after the examination using dedicated quantification software. So-called time-intensity curves (TIC) are computed from the time series for each pixel (2D+time data), or voxel (3D+time data). A TIC represents the enhancement in the corresponding region as a function of time, and correlates with the perfusion kinetics of the blood in the location after the injection of the contrast agent. Parameters describing the kinetics of blood perfusion are extracted from the TICs, then analyzed and compared in different regions to diagnose lesions characterized by abnormal perfusion. Typical descriptive perfusion parameters (see figure 1) include Time-of-Arrival of the contrast (TOA), Time-to-Peak (TTP) enhancement, Peak Enhancement (PE), Rise Time (RT), Area-Under-the-Curve (AUC), Mean Transit Time (MTT), Wash-in Rate (Slope/WiR) and Wash-out Rate (WoR) [46, 130].

The typical analysis workflow consists of three stages: First, the examiner attempts to delineate regions of interest (ROI) according to their echogenicity (in B-mode, or brightness modulation: pixel intensities represent the strength of the echo) and perfusion enhancement, by looking at the cine-loop (animated image sequence) of the CE data. This can be aided

by additional parametric images. Secondly, ROIs showing abnormal enhancement patterns are selected, and the perfusion in these regions is characterized. The final stage consists of comparing the perfusion parameters of the selected regions with each other or with healthy tissue (when possible), eventually leading to a diagnosis.

CE imaging became interesting also in conjunction with ultrasonography (US): recently, safe contrast agents have been developed, consisting of gas-filled microbubbles. They can be administered intravenously into the systemic circulation, and excreted through respiration and breakdown in the liver. The microbubbles have a high degree of echogenicity, and behave like signal-emitting micro particles, flowing with the blood. Moreover, the CEUS contrast agents are so-called blood pool agents, meaning that, contrary to X-ray contrast media, they do not leave the blood vessels [145]. This provides the clinicians with an excellent tool for following the dynamic phases of contrast enhancement in both large vessels and the microcirculation, delineating the vascular structure in the tissues.

CEUS examinations are generally performed freehand by the operator, who keeps the US probe as still as possible, focusing on the region of interest for a certain period of time after a contrast agent bolus is injected intravenously. The recorded time-dependent dataset consists of a sequence of staggered images (2D + time), acquired alternately in B-mode and a specific contrast mode, that uses low power and specific acoustic settings to filter out the tissue signal from the bubble signal. This way each contrast image, containing the contrast enhancement for a specific time-step, has a corresponding B-mode image, showing the anatomy clearly. Compared to contrast-enhanced computed tomography (CT) or dynamic contrast-enhanced magnetic resonance imaging (DCE-MRI) data, CEUS data show analogous perfusion patterns. Therefore the analysis process can follow a workflow comparable to the other CE modalities. However, there are certain unique characteristics that CEUS data exhibit, which pose serious challenges for the data analysis.

First, US has a lower signal-to-noise ratio, when compared with MR and CT. Secondly, the data exhibit a non-linear enhancement behavior, caused by the nature of the contrast agent. The gas-filled microbubbles have a discrete dimension ($\sim 10\mu\text{m}$), and do not fuse with the plasma but rather flow together with the blood stream. The enhancement is generated by the presence of bubbles under the US probe, and we observed that it is not continuous, but, to a certain extent, has an "on-off" type of behavior. We also observed that this behavior is more prominent with high resolution transducers, probably due to supersampling of the fixed-sized microbubbles and also of the voids between them. Thirdly, CEUS data are difficult to register, as the acquisition is performed freehand. It is almost impossible to keep the probe perfectly still, and deformations and off-plane movements add up to the effects of breathing and pulse. In such

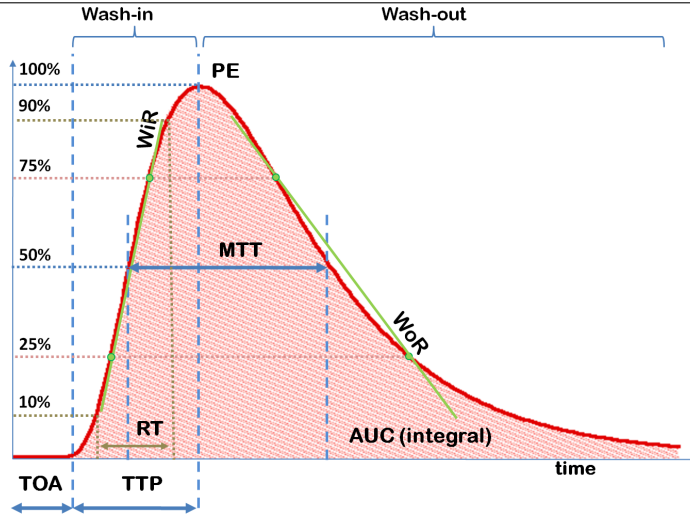


Figure 1: Illustration of an approach to compute descriptive perfusion parameters from a time-intensity curve.

a scenario, even deformable registration methods cannot provide maximum accuracy.

In this paper we present an interactive and iterative visual analysis approach for CE data exploration, analysis, and tissue classification. It is specifically tailored for the analysis of CEUS data, incorporating an innovative data processing framework that extracts accurate enhancement parameters, stabler in presence of noise and movements. It offers a visual exploration metaphor to discover relationships in the anatomy with respect to perfusion by using interactive similarity maps. Such maps visualize clearly and precisely areas with similar perfusion patterns with respect to the selected region, and also delineate other homogeneous areas. Our approach allows to extract automatically selection masks from similarity maps using a degree-of-interest function, and to combine such masks easily and quickly. Finally, we make use of different visualizations to enable effective analysis and comparison of selected masks (elected as ROI), and assess the tissue condition.

A.2 Related work

Applications for the analysis of CEUS data have mainly been developed by ultrasound scanner manufacturers¹ (e.g., GE, Philips, Siemens, Toshiba),

¹All brand names and trademarks mentioned in this paper are properties of their respective owners

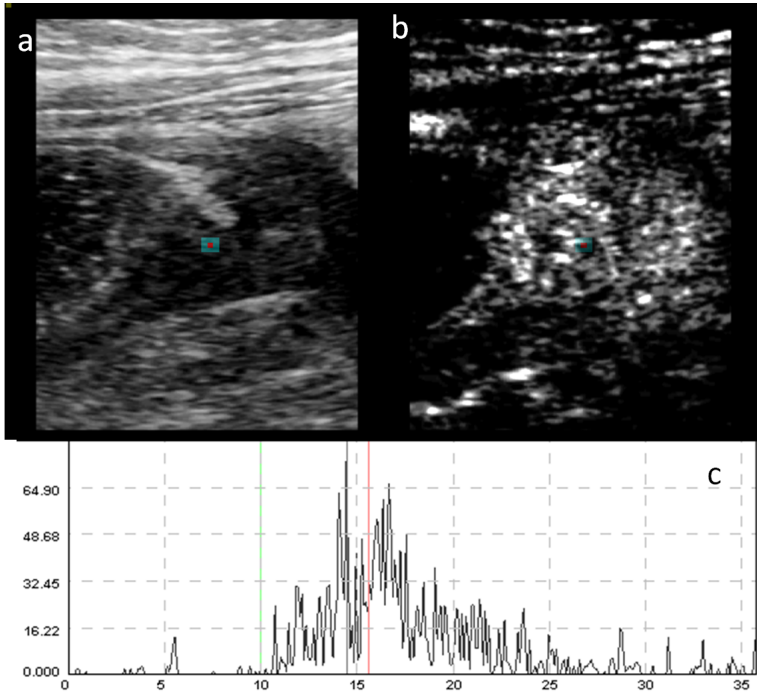


Figure 2: (a) Example of 2D CEUS data of the intestinal wall of a patient suffering from Crohn's disease: B-Mode data. (c) The related contrast data showing a typical (noisy) CEUS enhancement pattern. (d) Time-intensity-curve relative to the pixel highlighted in red in (a,b), after the contrast administration, showing the characteristic unstable enhancement.

and are generally integrated into their workstations. Some of them are also available as stand-alone software solutions, such as Philips Q-Lab [71], Toshiba CHI-Q [38], VRI [97], and a custom application developed by Toshiba for the Tokyo General Hospital [171]. All of these applications offer a relatively basic quantification and characterization; They allow the user to manually define one or multiple ROIs, and extract perfusion parameters for these regions. Some of the manufacturers, e.g., Siemens and Toshiba, recently added rigid registration capabilities to correct for breathing artifacts. More advanced stand-alone applications have been developed by Bracco Imaging, an US contrast-agent producer. Bracco has developed several applications for CEUS data analysis and quantification, ranging from general purpose CEUS analysis (Qontrast [3], QontraXt [68]) to applications addressing specific diagnostic questions (SonoLiver [153, 154], SonoProstate [46]). In contrast to the software packages integrated into the scanners, the solutions from Bracco are capable of deformable registration

of the image stack. This is useful when dealing with issues more complex than only breathing movements.

Regarding the techniques as adopted in the approach presented in this paper, visualization techniques that exploit small voxel neighborhoods have been proposed for building transfer functions by considering local histograms [107] or correlation [135]. Local neighborhoods have often been considered in the field of image processing, e.g., to de-noise MRI data by extracting non-parametric statistics [6], or by using fourth-order partial differential equations [108].

In the domain of visualization approaches for perfusion data, a number of techniques have been proposed in the last decade. Automatic or semi-automatic segmentation techniques have been proposed for DCE-MRI, Positron Emission Tomography (PET) and Single-Photon Emission Tomography (SPECT) data, using clustering [2, 26], principal component analysis [175], or region-growing [53] to identify abnormal areas. Enhancement scatterplots have also been proposed to select the voxels of interest [29]. Fang et al. [41] propose the use of the Euclidean distance and the maximum cross-correlation as similarity metric between TICs to segment volumetric, time-varying medical data, according to a user-specified template. The technique is applied to MRI and PET phantom datasets, and a SPECT dataset of a patient with kidney problems. Kohle et al. [87] presented a new approach for volume visualization of these datasets introducing the closest vessel projection to add depth information to maximum intensity projection. In this work a HSV colormap is used to better convey abnormal tissue. Hauth et al. [63] adopt a three-timepoints TIC analysis for automatic classification of the tissues. Rognin et al. [153] propose an analogous approach, which also requires the identification of a healthy region of reference.

For the visual exploration of time-dependent medical data, Behrens et al. [11] proposed some basic visualization techniques. A more intuitive concept to probe and annotate the data was presented with the Profile Flags [117]. Interactive visual analysis techniques have also been proposed for the exploration and characterization of time-varying perfusion data [130]. They have been specifically applied to the analysis of cerebral perfusion data [131]. Recently, Glaßer et al. [53] proposed a visual analytics approach to characterize malignant tissues. Preim et al. [148] provide a comprehensive survey on the visual exploration and analysis of perfusion data. With respect to automatic classification and characterization of tissues in CE imaging, neural networks [177] and the self-organizing map [119] have been employed to automatically discriminate benign and malignant breast lesions in DCE-MRI. Recently, Napel et al. [118] developed a system for automated retrieval of similar lesions from a database of CE-CT datasets (non time-varying).

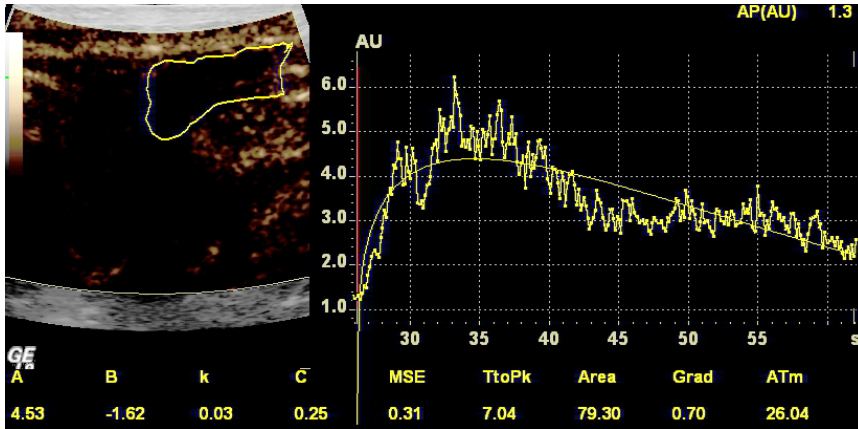


Figure 3: Screenshot of the perfusion analysis software present in the GE Logiq 9 workstation. The region of interest must be manually outlined, and an average TIC is displayed on the right, together with a function that is computed to best-fit the data. On the bottom various perfusion parameter are extracted and shown.

Compared with these approaches, we do not attempt to automatically segment or characterize the tissues. The reason for this is that even the best algorithms fail under certain circumstances, such as imperfectly aligned data or data containing a noisy signal, which is especially common in CEUS. We also do not want to replace the expertise of well-trained physicians, but rather to involve them in the process to achieve a more accurate result. We aim at providing fast and interactive exploration, and visually convey the segmentation of the data into regions with homogeneous perfusion patterns. We then offer a fast and interactive approach to segment these regions, combine them if necessary, and extract meaningful parameters to analyze and compare them. With this approach we want to help the physicians speeding up the diagnosis, by using the knowledge they have in the best possible way.

A.3 Requirement analysis

Before we present our CEUS exploration and analysis solution, we discuss the related application questions from a medical perspective (gastroenterology and cardiology). Several aspects of the data analysis process are covered, and can be summarized as follows:

- What limitations of the available tools cause the physicians the greatest discomfort, and should be improved?
- What visualizations solutions would the physicians benefit most from?

A. Interactive Visual Analysis of Contrast-Enhanced Ultrasound Data based on Small Neighborhood Statistics

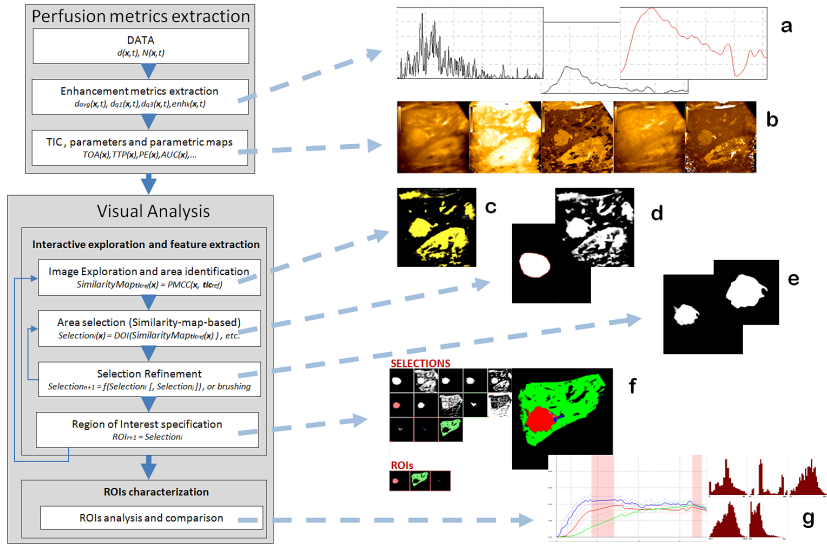


Figure 4: Illustration of the proposed pipeline. In the first stage enhancement metrics are extracted (a) and parametric maps are computed (b). In the IVA stage, data are explored interactively using correlation analysis (c), and selection masks can be automatically extracted (d). Masks can be automatically combined or refined (e) and selected as ROI (f). Finally, the ROIs can be analyzed and compared to assess the tissue condition.

At the present, the specification of the ROIs is considered a lengthy and cumbersome process, as the area of interest is not always clearly delineated in the US image, and it sometimes consists of heterogeneous tissue. The placement of the ROIs is a critical task in the process, as the ultimate goal of the analysis is to assess the extent, shape and composition of lesions. The physician has to examine different parametric maps before being able to distinguish regions and then decide where to place the ROIs. Another emerged problem with the available quantification software is how the perfusion curves are approximated and the parameters extracted. Figure 2(d) illustrates the typical enhancement in CEUS data, that exhibits high instability. Available software solutions perform little to no preprocessing of the data, partly due to the high computational cost of the operation. Since the unprocessed data are almost unusable due to their extreme instability in the enhancement, the currently most followed approach consists of fitting a statistical distribution to the samples, with characteristics similar to the blood perfusion kinetics in the tissue (e.g., a lognormal distribution function [46]). Unfortunately, in some real-life situations, the approximation provided by this approach might be not very accurate (see figure 3, the fitting do not match the samples well). Finally, the performances of the available tools in handling the whole analysis process

are also seen as a limiting factor, and an interactive and more integrated solution for exploring the data is needed.

We also had interdisciplinary discussions with physicians from the gastroenterology department at the Haukeland university hospital in Bergen, about the use of visualization techniques that have been previously proposed for perfusion visualization in the scientific community. While a (color) map of a single parameter does usually not suffice alone, from our discussions it emerged that clinicians are generally skeptical towards visualization techniques that combine multiple parameters, such as in a glyph visualization. Parametric maps are probably not far from the maximum complexity that clinicians are willing to use for visualization – visualizations for clinical practice have been requested to be *as simple and easy to understand as possible* (and also contain quantitative information where possible). It is however likely that physicians more oriented towards research are more willing to undertake a learning process and to use more compact but complex visualization metaphors. From the discussion it also emerged that physicians would benefit from an application capable to clearly convey where the boundaries of homogeneously perfused regions are, so that the selection of these regions would be easier, quicker and more precise. Therefore it seemed promising to invest into the interactive nature of the visual analysis approach, while keeping the visualization techniques easy to read and as plain and unambiguous as possible.

A.4 Visual CEUS Data Exploration and Analysis

The visualization pipeline presented in this paper consists of three stages, intended to gradually extract and visualize the perfusion trends (see figure 4). To overcome the noise-related challenges and the on-off signaling aspect of the contrast agent, the first stage extracts enhancement information for each voxel (pixel/timestep) from its local spatio-temporal neighborhood. We propose to derive three enhancement metrics: the mean enhancement value d_{avg} , the first d_{q1} and third d_{q3} quartiles of the values in the neighborhood, and the percentage of enhanced voxels enh_k . We also experimented with a number of other, related, measures, but these three metrics proved to produce stable and accurate profiles of the local enhancement, well representing the evolution of the contrast agent over time. Details on this stage with an explanation and more motivation are given in section A.4.1.

As a result of the first stage, useful enhancement curves are available, as well as parametric maps of the perfusion parameters described in the introduction, derived using the computed enhancement curves (see figure 4(b)). The second stage consists of an interactive visual analysis approach to identify and segment the regions of interest. To do so, the examiner would start getting an overview of the perfusion enhancement of the

anatomy by looking at parametric maps, for example of the AUC, PE, or another expressive parameter. Each of these parameters only represents a selected aspect of the perfusion, and we found that parametric maps, singularly, do not precisely outline the boundaries of suspicious regions. Therefore we included an interactive similarity map derivation, that, by selecting a pixel, a region, or a template curve shape, allows the classification of the data according to how similar the perfusion pattern is with respect to the selection (see figure 4(c)). Our method uses the Pearson product-moment correlation coefficient applied to the TICs as similarity function (details in section A.4.2). Once the examiner has outlined an area of interest with the similarity map, the region can be saved as a mask for later refinements. This procedure can be repeated to save more masks, which then can be combined using set and morphological operators (see figure 4(f,e)). In the third stage, the examiner elects the result of the processing operations on masks as ROIs, and, for each ROI, perfusion parameters are automatically computed. In this stage these ROIs can be analyzed and compared, with the system presenting the information about tissue perfusion for the selected ROIs, to eventually lead to the characterization of the regions. In the design of this pipeline we avoid to solely automatically characterize the tissues. Instead, we keep the physician involved and aid the characterization process, so that the result benefits also from her or his knowledge. In too many situations, in fact, single approaches alone would lead to the wrong diagnosis (such as only TIC comparison in our case), while an expert can usually combine the information extracted from the data to achieve a more accurate diagnosis.

Motion Correction The presented approach does not include any motion correction stage per se, and we assume that the image stack loaded in the application is already aligned. However, as this is usually not the case when the data come from the US scanner, we have used ImageJ [1] to register the datasets before the analysis. It uses the scale invariant feature transform (SIFT) [106] for feature extraction and, depending on the dataset characteristics, rigid registration or deformable registration using vector-spline regularization [5]. Our application is however not dependent on the motion correction approach adopted, and simply requires already aligned datasets.

A.4.1 Perfusion metrics extraction

As mentioned above, CEUS generates a signal that is not stable and may contain large oscillations. To better extract the enhancement value for each voxel location in space and time (x, t) along a TIC, we propose to extract three simple statistical measures from the local spatio-temporal neighborhood $\mathcal{N}(x, t)$ of the voxel (Figure 5(a)). We refer to the enhancement values

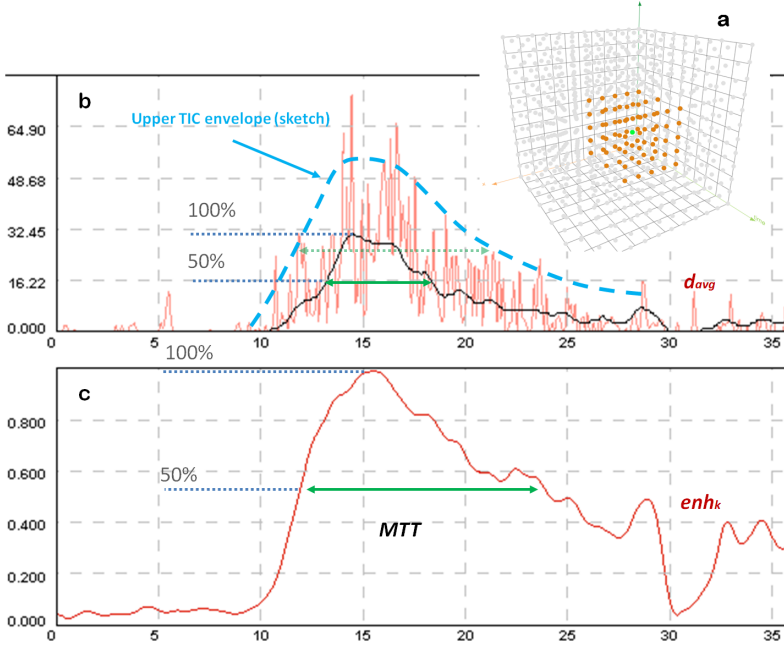


Figure 5: Illustration of a $5 \times 5 \times 3$ neighborhood considered to extract the perfusion measures (a) from a noisy dataset. Here, the Z dimension represents time. Comparison between the original TIC, also shown in figure 2 (red), the TIC built using the d_{avg} measure (black, b) and the profile built with the enh_k measure (red, c), showing the percentage of voxels in each neighborhood greater than a value k (here set to 25 over 255). In case of highly unstable signal, the enh_k profile proves to produce more accurate results during the perfusion parameter extraction (e.g., MTT)

of each voxel (\mathbf{x}, t) as $d(\mathbf{x}, t)$. We computed the mean value $d_{avg}(\mathbf{x}, t)$, as the average of the enhancement values in $\mathcal{N}(\mathbf{x}, t)$:

$$d_{avg}(\mathbf{x}, t) = \frac{\sum_{\mathbf{p} \in \mathcal{N}(\mathbf{x}, t)} d(\mathbf{p})}{|\mathcal{N}(\mathbf{x}, t)|} \quad (1)$$

This measure is needed to obtain a much stabler TIC shape for the computation of the similarity factor between TICs. Using the raw intensity data, the similarity derivator struggles finding enough correlation between any pair of TICs, while stabilizing and improving the shape of the curves proved to produce more meaningful results. Together with the mean, we also compute the quartiles $d_{q1}(\mathbf{x}, t)$ and $d_{q3}(\mathbf{x}, t)$ of the values in the neighborhood, defined as:

$$d_{q1}(\mathbf{x}, t) = \min_f \frac{|\{d \in \mathcal{N}(\mathbf{x}, t) \mid d \geq f\}|}{|\mathcal{N}(\mathbf{x}, t)|} \leq \frac{3}{4} \quad (2)$$

$$d_{q3}(\mathbf{x}, t) = \min_f \frac{|\{d \in \mathcal{N}(\mathbf{x}, t) \mid d \geq f\}|}{|\mathcal{N}(\mathbf{x}, t)|} \leq \frac{1}{4} \quad (3)$$

When compared with d_{avg} , d_{q3} turns out to be a better approximation for the curve upper envelope in case of unstable signals. Plotted together with $d(\mathbf{x}, t)$, d_{q1} and d_{q3} are used to convey the degree of oscillation of the signal for single TICs, or the heterogeneity of a ROI. These measures are eventually used to build up TICs, helping with the problem of voids in the perfusion pattern, as the value is now an aggregated over the local neighborhood.

However, to cope with the considerable "on-off" enhancement behavior present in certain CEUS datasets, typically acquired with high resolution transducers, we propose also a third measure, called *percentage of enhancement*. We refer to it as $enh_k(\mathbf{x}, t)$, and it is computed for each neighborhood $\mathcal{N}(\mathbf{x}, t)$ as:

$$enh_k(\mathbf{x}, t) = \frac{|\{\mathbf{p} \in \mathcal{N}(\mathbf{x}, t) \mid d(\mathbf{p}) \geq k\}|}{|\mathcal{N}(\mathbf{x}, t)|} \quad (4)$$

By specifying an enhancement threshold value k , ideally representing the minimum intensity value in presence of contrast, enh_k represents the percentage of enhanced voxels in each neighborhood. The value k is dependent on the dataset, as different scanners/setups produce signals with different intensity. However we let the user interactively modify this threshold, with the aid of a histogram of the dataset intensity values. We discovered that this metric, used to build *enhancement profiles*, highlights better the perfusion trends in presence of highly unstable enhancement, as compared with the raw and the averaged data. In such situations, profiles created with the other two proposed metrics tend to move away from the TIC upper envelope. So the enhancement profile, although not containing quantitative information, is useful to extract time-dependent measures (e.g., TOA, TTP, MTT) more precisely (see figure 5).

We have not been able, so far, to automatically compute the ideal neighborhood size for a given dataset, as there are many variables to take into consideration (e.g., scanner technology, transducer wavelength, contrast agent type). Therefore we include the option to interactively modify the size of the neighborhood, giving a visual feedback to let the examiner adjust the size to the data under analysis (in figure 2(a,b) the neighborhood is highlighted in green). This stage is computationally very expensive, and to enable the possibility of interactively changing the neighborhood dimension and the threshold value k , we developed a GPGPU implementation of the described statistic extraction techniques, written in OpenCL. In our implementation, each kernel independently performs the extraction of the described measures for a single voxel (pixel/timepoint), thus achieving a high level of parallelization, required for enabling fast interaction.

A.4.2 Interactive visual analysis

In order to correctly understand the boundaries of the ROIs and to outline them, at the present the examiner has to mentally correlate different parametric images together with the contrast data cine-loop. We instead propose a multi-stage interactive visual analysis (IVA) approach. In the first stage, a perfusion enhancement pattern is selected. The system automatically computes a *similarity* map, highlighting regions with a perfusion pattern similar to the selection. This map can be automatically converted into a selection, and can be also thresholded on the similarity value. Finally, saved selections can be further processed and combined with other selections via common morphological or set operators to accurately define the ROI (See section A.4.2). In such maps, however, other homogeneous regions also appear in uniform value and color, and can be easily spotted. Therefore, this procedure can be *iteratively* repeated to inspect other areas, and specify other ROIs using the related similarity maps.

Similarity measure for TICs

The perfusion enhancement for a pixel is defined by its TIC. To measure how similarly two pixels enhance, we use the Pearson product-moment correlation coefficient (PMCC [84]). The PMCC between two variables (TICs) A and B is defined as the covariance of the two variables, divided by the product of their standard deviations:

$$PMCC(A, B) = \frac{\sum_{i=1}^n (A_i - \bar{A})(B_i - \bar{B})}{\sqrt{\sum_{i=1}^n (A_i - \bar{A})^2} \sqrt{\sum_{i=1}^n (B_i - \bar{B})^2}} \quad (5)$$

with \bar{A} being the average of the samples A_i over the entire time span. The PMCC is a measure of the linear dependence between two value sequences, giving a value between +1 and -1. A value of 1 implies that a linear equation describes perfectly the relationship between the two value sequences. A value of 0 implies that there is no correlation, and a negative value implies that the variables are inversely correlated. In other words, the PMCC is a measure of shape similarity of two TICs. Therefore we can visualize how similarly two anatomical areas perfuse over time by showing PMCC values as parametric map.

Similarity-based exploration and segmentation

To obtain a similarity map for an area, understand perfusion relationships and specify ROIs, the examiner must be able to provide a target enhancement pattern. Once a similarity map has been obtained, it is superimposed semi-transparently over the cine-loop visualization. As the final goal of the IVA process is to characterize suspicious tissue, similarity maps can be

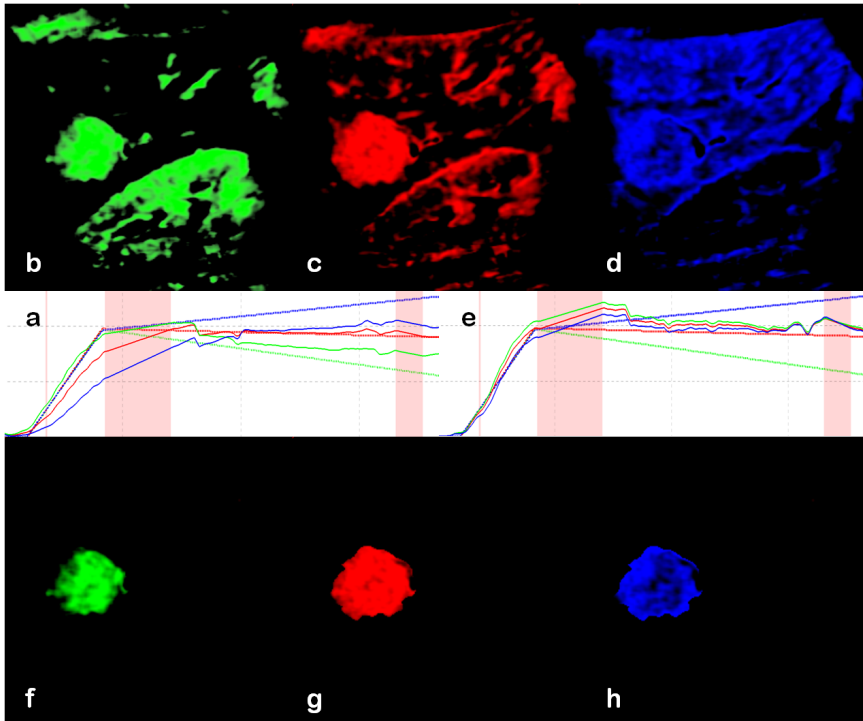


Figure 6: ROIs created using curve templates to investigate the variation in perfusion characteristics. Three templates (continued enhancement, stabilizing enhancement, measurable wash-out; depicted as dashed lines in a) and their corresponding similarity maps (b, c, and d). The template with higher wash-out profile highlights the boundaries of the lesion (d), while the one with lower wash-out highlights the core of the lesion (b). The TICs illustrated in (a) show a certain variation, that requires to be investigated. By applying a segmentation mask around the lesion to the maps in (b),(c) and (d) we obtain three new selections (respectively f, g and h). Their TICs are shown in (e), highlighting a much more similar pattern. This reflects a fairly homogeneous lesion compound.

converted into selections, processed and finally used as ROIs. In the application, a degree-of-interest (DOI) ramp function is applied like a transfer function as soft threshold for the conversion (as compared with a step function). In our application enhancement patterns can be provided in different ways:

By pixel selection using the cursor, it is possible to interactively select a pixel in the image. The system computes and displays the similarity map using the TIC of this pixel (Figure 8(e,f,g)).

By template TIC using a special widget, it is possible to sketch a perfusion enhancement pattern. The system uses this pattern to compute

and show a similarity map highlighting regions that perfuse similarly to the sketched pattern, providing interactive feedback to the user (Figure 6).

By area selection using an already stored selection, the system can compute the similarity map from the TIC averaged over the selection. In combination with the proposed map-to-selection conversion approach, this allows iteration over a selection to obtain a similarity map built upon a more representative TIC of the tissue under inspection.

Arbitrarily shaped selections can also be created, by using a brush or a lasso tool, and once a selection has been stored, it is displayed in a selection list, from where it can be specified to perform further operations. The operations on selections we included are:

- extraction of an averaged TIC, used for similarity map generation. With our smooth selections, we perform the TIC averaging using the DOI value in each pixel to produce a weighted average for each TIC.
- modification of the selection using morphological operators (dilation/erosion).
- combination with other selections using set operators (union/intersection/subtraction/inversion).

As a result of these operations, new selections are produced and inserted into the selection list, from where they can be used. Once the output selection is satisfactory, is ready to be analyzed, and it can be promoted to ROI (see figure 7(a)).

ROIs comparison and characterization

In the first IVA stage, ROIs have been defined. In this last stage, these regions can be analyzed individually, or compared with each other. Our application extracts and visualizes the TICs and the enhancement profiles of the ROIs. TICs are visualized as an average curve, upper and lower bounded by the first and third quartile, to visually convey the degree of homogeneity of the ROI (see figure 4(g)). Each ROI is also accompanied by its perfusion parameters and a histogram matrix showing the distribution of their values over the range. This way the shape, dimension and perfusion pattern can be analyzed to characterize the region. These parameters can also be compared to the healthy tissue (if available) or between different region, to refine the diagnosis, as we show in section A.5.1.

The application lets the user select which of available ROIs to compare. Selected ROIs are superimposed over the CEUS data, each one with a different color. When more than one ROI is selected and displayed, there may

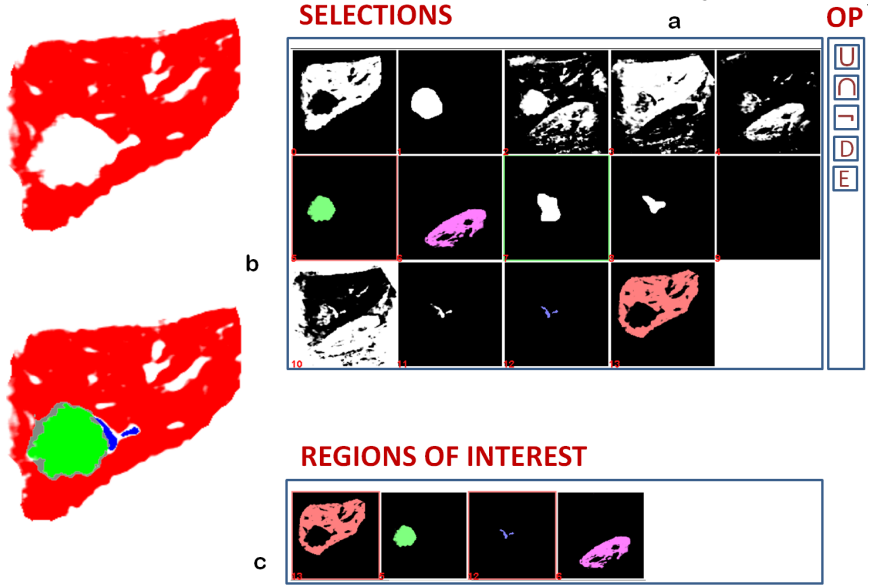


Figure 7: Selection-based generation of the ROIs: the selections are displayed with the number shown on their lower left, and can be processed with set/morphological operations (for example, here 12 was generated by inverting 3 into 10, intersecting 10 with 8 into 11, and then eroding 11). When a selection is suitable, it can be promoted to ROI, and is shown on the bottom area(a). ROIs can be analyzed singularly (b) or together (c). When multiple ROIs are analyzed, the regions where two or more ROI overlap can be treated considering the uncertainty in that area, and if the uncertainty is too high, the area is removed from all the conflicting ROIs, and shown in grey.

be a partial overlap. However selections are not binary: as mentioned, they contain pixel values within the $[0,1]$ range. Therefore we developed a voting scheme approach, that uses a user-specified threshold, to assign these overlapping areas to the ROI they most likely belong to. It can be formalized as follow:

$$ROI(\mathbf{x}, k) = \begin{cases} i \mid \forall j \neq i, \\ ROI_i(\mathbf{x}) > ROI_j(\mathbf{x}), & \text{if } |\{j \mid ROI_j(\mathbf{x}) > k\}| \leq 1 \\ -1, & \text{if } |\{j \mid ROI_j(\mathbf{x}) > k\}| > 1 \\ -2, & \text{if } \forall j, ROI_j(\mathbf{x}) = 0 \end{cases} \quad (6)$$

When two or more overlapping selection in a pixel have a value greater than the threshold k , then we cannot precisely determine to which of the ROI that pixel belong. Therefore the pixel is assigned to an "uncertain" grey region (-1 in equation 6). Otherwise, the pixel is assigned to the ROI that has highest value in that location (see figure 7(c)). Once this voting

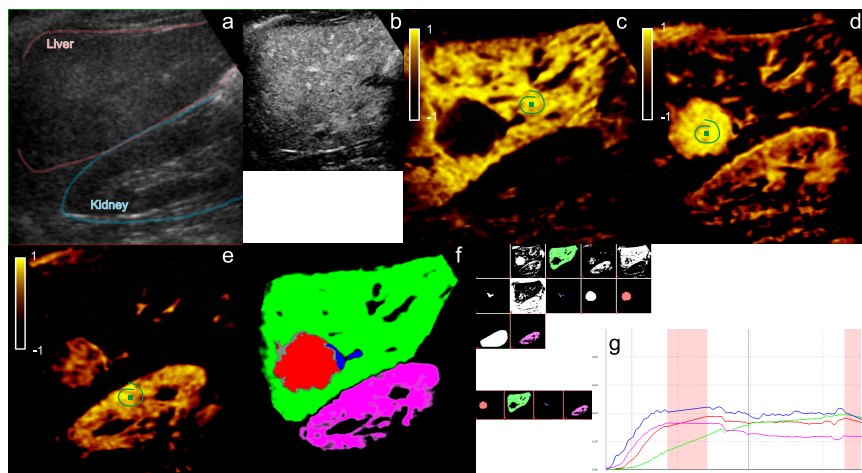


Figure 8: Interactive visual analysis of a dataset with a liver lesion. One B-Mode image showing the imaged anatomy (a). One contrast image from the dataset, showing diffuse enhancement, where only vessels are highlighted (b). Similarity map for a point specified on the (presumably) healthy liver parenchyma, in green. The healthy tissue highlights, and also delineates other structures in the liver, such as the vessels and the lesion on the left (c). Similarity map for a point specified on the lesion. The lesion highlights entirely (d). Similarity map for the kidney (e). ROIs defined on the healthy tissue (green), lesion (red), lesion feeding vessel (blue) and kidney (purple). In grey the uncertain area. (f). TICs for the four ROIs. The lesion exhibits a kinetic similar to the feeding vessel, much earlier (TOA and TTP) when compared with the healthy tissue, similar peak enhancement, and almost iso-echoic behavior in the mid phase (g).

scheme has been applied, we have two different set of parameters available: those related to the original ROIs and those related to the ROIs after the voting scheme has been applied. The two set can be analyzed separately, or overlapped to convey the changes.

A.5 Results

With our approach we have analyzed a six CEUS datasets imaging focal liver lesions. These datasets are representative for their respective diagnostic field, concerning spatial and temporal resolution, and also concerning the observed enhancement behavior. Our application makes use of the OpenCL computing framework to perform real-time measures extraction and PMCC computation operations. To be run, it requires a computer supporting it. We therefore ran the application on a workstation with an Intel Core CPU 2.5GHz and an nVIDIA GeForce GTX280 graphics card, for which nVIDIA provides drivers that support OpenCL. From a performance point of view, this system allows interactive exploration without

particular delays using typical settings. Increasing the neighborhoods diameter over 10 pixels, however, begins to generate waiting times even using the gpu to perform the computations. However, too large neighborhoods bring no benefits to the analysis, and particularly they cause a loss of detail on the edges of the regions. We experienced that, even for datasets acquired with high resolution probes, the neighborhood diameter should not exceed a size of 7–9 pixels to prevent information loss.

A.5.1 Liver Lesion diagnosis

In the case of a liver lesion, the parameters that have to be evaluated to assess the type of the lesion [149] are:

- the enhancement dynamics, to assess the type of vascularization in the lesion
- the consistence of the enhancement in the lesion, e.g., if there are multiple layers with different perfusion patterns
- the shape of the lesion

Case Study The patient suffered from flank pain and appeared to have several liver lesions. Each one of them was separately imaged in a dedicated perfusion examination. Here we describe the analysis of one of the scans, which is also representative for the other cases we studied. The sequence is cut short (in time), before the contrast is completely washed out from the area, thus containing only the arterial phase. It is enough data, however, to assess the vascular structure in the lesion, together with its shape and echogenicity. The resolution of the data containing the liver and the right kidney is 240×240 pixels, with 257 timesteps, acquired at approximately 9 frames per second, for a total duration of about 30 seconds.

Visual Analysis The results of the visual analysis are illustrated in figure 8. After the data was loaded, the perfusion metrics were automatically extracted using the default settings for the neighborhoods size (diameter of 5 pixels for the spatial dimensions and 3 timesteps for the temporal dimension). The system also provided an enhancement profile computed over the whole enhanced area (thus excluding areas that are never enhanced) to automatically identify the global TOA (TOA in the regions enhanced first). The computation of the other parameters discarded all the information prior to the global TOA. We then ran the cine-loop to identify frames with alignment errors, so that they could be excluded from the analysis, and the values interpolated using neighboring frames (Figure 8(g), the red bands

on the plot represent timesteps with interpolated frames). After this procedure was completed, we visually examined the map of the various parameters to identify the regions with the highest perfusion (Figure 4(b)). This map highlighted the liver parenchyma, part of the kidney parenchyma (that usually has a fast wash-out and thus a small AUC), and most prominently the vessels as well as a region on the left not consistently defined among the maps. So we selected a pixel on the (presumably) healthy liver parenchyma, to obtain a similarity map for the healthy tissue (Figure 8(c)). We converted the similarity map for the healthy area into selection, to use as reference (Figure 8(f,g) (green)). In the similarity map of the healthy tissue, the non-consistently defined region on the left gained a much sharper contour, as it was very different in perfusion. So we investigated that area by selecting a pixel, and obtained the similarity map for what turned out to be a lesion (see figure 8(d)). The lesion was precisely highlighted and we converted it into a selection, and then we specified a rough lasso selection over it, that we used to intersect the similarity-based selection (Figure 8(f) (red)). We also noticed how the lesion was surrounded by an area with higher enhancement on the right, presumably the supplying vessel. We segmented it, using the similarity map, to compare the arterial input to the lesion (Figure 8(f) (blue)). At this point, thanks to the similarity map, we had assessed the composition of the lesion (single compound), the shape (regular) and the size (diameter of about 3cm). Then we entered the last stage of the analysis, and compared the perfusion in the lesion with the perfusion in the healthy parenchyma (Figure 8(g)). We found that the lesion enhanced earlier than the healthy tissue (TOA and TTP), and in the late phase it was almost iso-echoic. But the peak enhancement was lower and in general the wash-out began slightly earlier, which indicates the absence of the portal phase. These features should characterize the lesion as a rare hepatocellular adenoma (benign) [49, 149]. After the patient also underwent a liver biopsy, the diagnosis was eventually confirmed.

A.6 Conclusion

In this paper we demonstrated how interactive visual analysis can lead to an improved analysis of CEUS data. For this application, we make use of an innovative data processing step that extracts robust enhancement measures from small spatio-temporal voxel neighborhoods to overcome the challenges arisen from the peculiar characteristics of CEUS data. With this approach, we can extract meaningful and realistic perfusion parameters even from this challenging data. We introduce the possibility to interactively explore the data using an interactively generated parametric map of similarity that improve the visual comprehension of the extent of suspicious tissues, and of the relationships between different tissues with respect to the perfusion enhancement pattern. Such approach showed a

good potential also when compared with automatic segmentation techniques such as automatic clustering, using the same similarity function. Here, the real-time interaction and feedback from the system provides the user with a better understanding of the data. By using such similarity map, it is also possible to automatically derive selections of homogeneously perfusing tissue highlighted in the map. Specified selections can be quickly combined into ROIs, that can eventually be analyzed and compared to assess the tissue condition. Compared to the available solutions, our system provides a faster and more accurate method for identification and segmentation of the ROIs, which has the potential to lead to a more accurate diagnosis. The solution presented here is the result of an interdisciplinary cooperation – between a team of technologists (visualization researchers with a background in computer science) and physicians (with a background in gastroenterology). The cooperation extended over the whole process from the initial assessment of limitations of current solutions all the way to the iterative improvement of the presented technology and to its initial informal evaluation studies. In the informal evaluation we discussed the approach with two experienced gastroenterologists, both familiar with CEUS in the clinical routine. Both were positive toward the interactivity of the application, and that the presented approach may be useful for the extraction of ROIs and their analysis. The interaction required for the selection processing step has proved to be relatively easy to understand and to use. As future work, we plan to perform a more thorough comparison of our approach with existing tools for CEUS analysis, to investigate more thoroughly the impact on the analysis of the misaligned frame removal strategy and to try to apply the presented technique to different kind of perfusion data, e.g., DCE-MRI.

Acknowledgements

This work has been carried out within the IllustraSound research project (# 193170), which is funded by the VERDIKT program of the Norwegian Research Council, with support of the MedViz network in Bergen, Norway (PK1760-5897- Project 11).

Straightening Tubular Flow for Side-by-Side Visualization

Paolo Angelelli¹, Helwig Hauser¹

¹Department of Informatics, University of Bergen, Norway

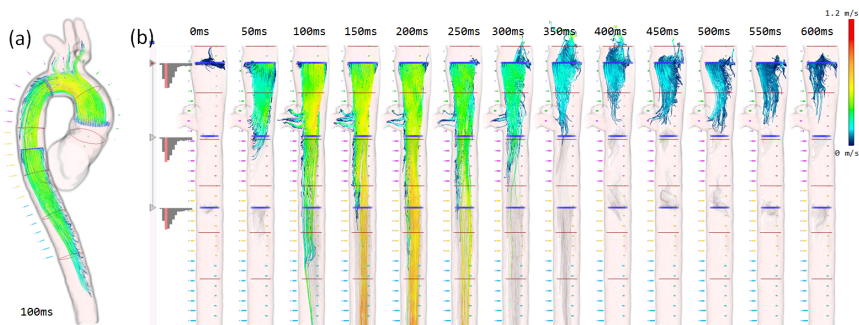


Figure 1: (a) A timestep of an aortic flow dataset in its anatomical context, rendered using a conventional streamline visualization. (b) Side-by-side visualization of the straightened vector field, showing all the timesteps juxtaposed. The streamlines traced from the first seeding plane are rendered in focus, and the others in grey as context.

Abstract

Flows through tubular structures are common in many fields, including blood flow in medicine and tubular fluid flows in engineering. The analysis of such flows is often done with a strong reference to the main flow direction along the tubular boundary. In this paper we present an approach for straightening the visualization of tubular flow. By aligning the main reference direction of the flow, i.e., the center line of the bounding tubular structure, with one axis of the screen, we are able to natively juxtapose (1.) different visualizations of the same flow, either utilizing different flow visualization techniques, or by varying parameters of a chosen approach such as the choice of seeding locations for integration-based flow visualization, (2.) the different time steps of a time-dependent flow, (3.) different projections around the center line, and (4.) quantitative flow visualizations in immediate spatial relation to the more qualitative classical flow visualization. We describe how to utilize this approach for an informative interactive visual analysis. We demonstrate the potential of our approach by visualizing two datasets from different fields: an arterial blood flow measurement and a tubular gas flow simulation from the automotive industry.

B.1 Introduction

Tubular flows are studied in many fields, such as in medicine and engineering. The visual exploration and analysis of such flow data can be challenging, due to the often varied geometry and topology of the flow, and due to a larger number of aspects of the data that are of interest, in particular in time-dependent flow. These aspects include various scalar attributes, such as flow velocity, pressure and vorticity (see Section B.2 for a collection of surveys on this topic), as well as derived attributes. On the visualization side, the variation of seeding structures, integration length and the type of primitive for an integration-based visualization, different time steps of the flow, and the variation of other visualization parameters are also aspects of interest.

To enable an analysis that is based on several such aspects, it becomes interesting to consider different views on the data as well as the relation between these views. Different strategies for integrating different visualizations have been proposed: interactive tools for the visual exploration with multiple, coordinated views [33, 113], the fusion of different visualizations in the same view [48, 83, 133], and placing different views side-by-side [182]. Image fusion techniques are powerful tools, as they can

visualize multiple aspects of the data in the same reference frame, thus allowing to easily and effectively relate them to each other. On the downside, there are rather limiting restrictions on how much can be fused in a single image. Side-by-side visualizations, instead, can integrate more views of the data, only limited by the overall available space. Moreover, being these visualization simpler when compared to others, they are generally easier to read and interpret. Additionally, they can also be used to show the same attribute over multiple time-steps or visualized with different parameters, thus enabling alternative types of visual comparison. Last, they can also be combined with image-fusion techniques, leading to side-by-side visualizations of fused views. In terms of limitations, it takes additional space to juxtapose views, so the number of views that can be placed side-by-side is also limited. Second, relating separated views is not a straightforward process, as they are not specified in a common reference frame anymore. Previous work [182] suggests that the question of whether or not to use side-by-side visualization also depends on the application at hand and on which advantages/disadvantages to prioritize. Our contribution addresses the cases where a side-by-side visualization is preferred.

We propose a new solution to the side-by-side visualization of tubular flow datasets. In order to effectively juxtapose views of tubular flows, we introduce the concept of straightening the flow visualization (e.g., streamlines or pathlines) along the center line of the bounding tubular structure, often being the main reference direction of the flow. Using this approach multiple views can be aligned with one axis of the visualization and made parallel to each other along the straightened center line. With such a side-by-side layout it becomes possible to relate different views in the visualization in a straightforward way, as well as making the visualization more compact, allowing to have more views at the same time.

In this paper we first describe how to realize such a straightened visualization. Then, we show how the presented approach has been used, in Section B.4, to visualize two tubular flow datasets: a Phase-Contrast Magnetic Resonance Imaging (PC-MRI) scan of a human aorta, containing time-dependent measurements of the blood flow, and a CFD simulation of the exhaust system of a racing engine. Conclusions and future work are presented in Section B.5. A discussion of related work is presented in the next Section.

B.2 Related Work

Flow visualization is an active research topic for over two decades. An extensive body of related literature exists, and many useful surveys exist as well. Post et al. [143, 144], as well as Laramée et al. [95, 96], Peng and Laramée [138], McLoughlin et al. [112], Salzbrunn et al. [162] and Pobitzer

et al. [142] have published extensive and informative surveys on different aspects of flow visualization.

Considering specifically the visualization of tubular flow, Nobrega et al. [125] simulated tubular flow in its context, relying on the centerline of the boundary structure for which they propose a novel extraction algorithm. Lež et al. [103] propose an interactive visual analysis approach for studying pathlines, using projections of the dataset for the selection process and to cope with the complex topology of the flow and its tubular context. More domain-specific work has been done, in particular in the field of medical visualization. Van Pelt et al. [180] incorporated illustrative visualization techniques in an application for visualizing blood flow in the aorta and other large vessels, introducing flow-rate arrow trails. Markl et al. [110] presented a comprehensive 4D visualization of the blood flow in the heart and great vessels by using glyphs, streamlines and pathlines, as well as exploded views with information visualization techniques.

One of our main goals was to enable an efficient comparison of the different aspects of the tubular flow data. Previously, Verma and Pang [182] presented a tool for comparing flow data. An important contribution of their work is the distinction of three possible levels of comparison in flow visualization: image-level, data-level and feature-level. They describe the major drawback of image-level comparison as “it leaves the burden on the users to identify regions of difference and to quantify the differences themselves”. Our approach eases the comparison by using the main direction of the flow to align multiple visualizations, paralleling each other, so that it becomes straightforward to relate the side-by-side views. Jones and Ma [73] have also adopted a similar concept to ease image-level comparison, by projecting integrated lines onto the three Cartesian planes.

Relevant work has also been done for reforming tubular structures into a plane, also here in particular in the field of medical visualization. Vilanova et al. [184] perform a 2D reformation of 3D human colon data. They extract the colon centerline, and use it for performing nonlinear radial raycasting, producing a flattened view of the internal wall of the colon. Kanitsar et al. [75] presented curved-planar reformation (CPR) approaches for entire vascular trees. Borkin et al. [18] also created projections of the coronary artery tree, mapping it to a 2D tree chart, where each vessel is straightened and depicts its endothelial shear stress. Ropinski et al. [156] applied flattening techniques to volumetric scans of mice aortas, to provide a navigational tool that links 2D and 3D visualizations of their multi-modal dataset. Curved-planar reformations has also been applied to other anatomical organs. Vrtovec et al. [190] applied CPR to human spine datasets: this work enabled the comparison of all the vertebrae in a single visualization, without the need of slicing through the volumetric scan. Daae Lampe et al. [93] presented a new technique to perform curve-centric volume reformation (CCVR), straightening the original 3D scalar data into a

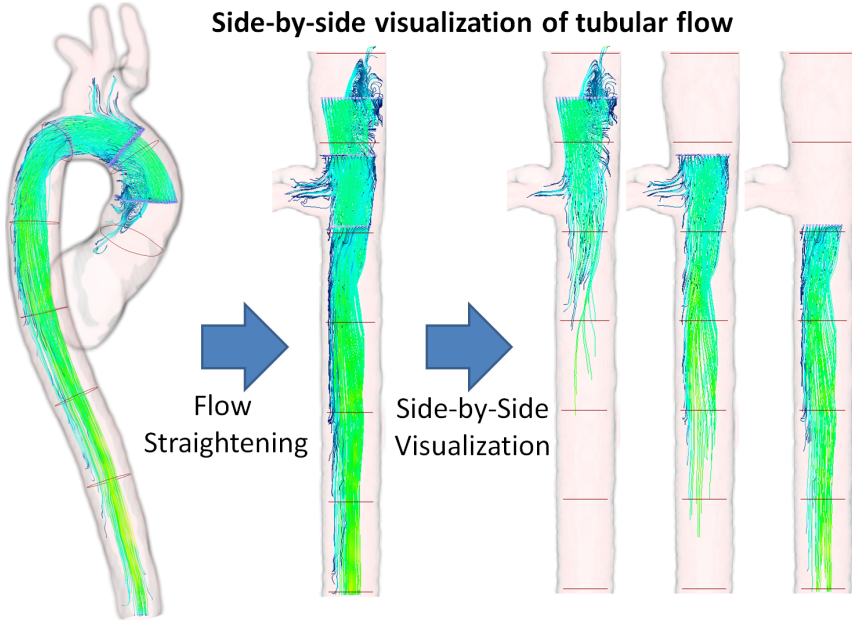


Figure 2: Illustrative overview of the proposed approach to realize a side-by-side visualization of tubular flow based on straightening the flow domain. In the side-by-side visualization the seeding structure has been varied in order to study different seeding locations.

new volume, centered around a 3D curve. This can be considered as warping the space, and previously Chen et al. [25], as well as Correa et al. [28], proposed generalized space warping methods, based on spatial transfer functions and generalized displacement mapping.

The method presented in our paper pursues the same purpose, however targeted not only to scalar data, but especially to vector field data. In the following we first describe how to realize straightened side-by-side visualizations of tubular flows before we then demonstrate our approach in the context of two application examples.

B.3 Method

In the following we present our method for creating straightened side-by-side visualizations of tubular flows, as illustrated in Figure 2. The method can be used to complement regular visualizations of tubular flows, in order to statically visualize multiple aspects of the data at once, including the time dependency. We describe the method in two parts: first, two techniques for generating straightened visualizations of tubular flows, defined as vector fields on a Cartesian grid; then, a set of techniques to assemble

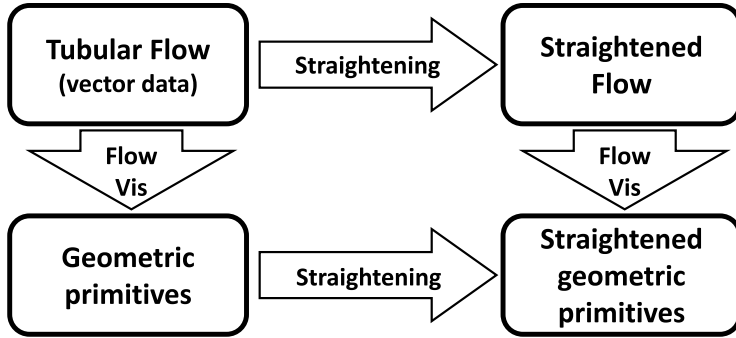


Figure 3: Two paths to realize a straightened visualization of tubular flow data: straightening flow visualization or visualizing straightened flow.

these straightened views in order to create efficient side-by-side visualizations. The first part is described in the next Section, while the second part is described in Section [B.3.2](#).

B.3.1 Centerline-centric tubular flow straightening

Conceptually, visualizations of straightened tubular flow can be generated using two different approaches (see [Figure 3](#)):

Straightening the flow domain: this approach performs a curve-centric vector field reformation (CCVFR), to generate a deformed vector field, straightened along the centerline of the tubular structure. In the second step, any flow visualization technique can be used directly to visualize this reformed vector field, producing straightened views of the flow. To perform the CCVFR, we introduce a method that extends the algorithm proposed by Daae Lampe et al. [[93](#)], such that it can be used to reform vector fields. This method is described in [Section B.3.1](#).

Straightening the flow visualization: this approach generates the primitives used for visualizing the flow, such as streamlines, pathlines, or more complex visualization cues, in the original flow domain. These generated visualization elements are subsequently deformed into the straightened domain using the centerline as reference. We describe an algorithm to perform this operation on line primitives in [Section B.3.1](#).

The advantage of the first approach is the simplicity of producing flow visualizations: once the vector field is reformed, any existing flow visualization technique can be used without modification. This also avoids

performance penalties when compared to visualizing the original data. On the downside, the vector field reformation process may introduce numerical inaccuracies. Reforming visualization cues, on the other side, produces an exact straightening of the visualization primitives, at the cost of a higher computational complexity. Moreover, this approach requires a tailored algorithm for each flow visualization technique to be realized. In order to combine the best of both approaches and to avoid the mentioned drawbacks, we realize a hybrid scheme, that renders the straightened vector field data during user interaction, to keep the system interactive. The second approach is then used on demand, to produce an as accurate as possible straightened visualization. Performance and error analysis are described in section [B.4.3](#).

Prerequisites

The straightening operation, that is integral to both of the approaches, grounds on the definition of a curvilinear coordinate system that is constructed along and around the centerline through the flow tube. Conceptually, we can consider a *moving frame*, similar to the Frenet frame of a curve [44], following the centerline of the structure bounding the flow, and thereby tracing the curved, centerline-centric, frame of reference for this tubular object. This moving frame is used to extract oriented cross-planes orthogonal to the centerline, and eventually to define a new grid for the data. Details on how to generate this grid within the curved structure are given in Section [B.3.1](#). Before, however, we describe how to extract the centerline itself, and how to compute the frame along it.

There exist several techniques for extracting centerlines, both from geometric data [125] and from volumetric data [27, 99, 183]. To demonstrate our method in Section [B.4](#), we use the approach proposed by Cornea et al. [27], previously also used in other works [156]. This approach operates on volumetric data, and extracts the skeleton of an object using a potential field. The skeleton consists of a set of segments, which need to be connected in order to create the final centerline. For the cases shown in this paper, we extracted the lumen of the tubular objects automatically, by thresholding a scalar volume containing the maximum magnitude of the vectors over all the time steps. For the aorta dataset, this extracted structure has been semi-automatically refined using the ITK-SNAP tool, to increase the accuracy and remove other vessels. However, different automatic techniques for 3D vessel lumen segmentation could also have been used, and Lesage et al. [101] provide a comprehensive survey on the topic. Once we extracted the object skeleton, we computed the final centerline using a tool based on the Visualization Toolkit (VTK), helping to pick and connect together the skeleton segments. This process could also be automated [156], but, for our purpose, it did not require further refinements.

Given a curve, such as the above-mentioned centerline, several methods for computing moving frames are available, and Daae Lampe et al. [93] provide a useful survey on this topic. In their paper, they also propose a modified version of the Frenet-Serret formulas for computing a moving frame [44], achieving a curve-centric (scalar) volume reformation (CCVR). The Frenet frame is, in fact, limited to twice continuously differentiable curves. By using a constant, user specified *up vector* to compute the binormal in a curve point, the authors both achieve a fixed frame orientation for the whole reformation, and a definition of the binormal (and subsequently of the normal) also where the curve is straight, and the derivatives would be vanishing. They also convolve the tangent and the normal with a smoothing kernel to prevent an exceeding roughness of the curve. Interpolation, in their case, is performed in spherical coordinates, to prevent abrupt sign changes of the vectors. This technique has, however, the obvious limitation that it is not applicable in those points of the centerline where the normal is parallel to the user-specified up vector.

To overcome this limitation, we extend this method by using a user-specified up vector (that also defines a fixed frame orientation around the centerline) only in the initial point of the centerline. We observed that the centerline is subdivided in segments by a number of evenly spaced positions along the line, depending on the desired amount of orthogonal cross-planes. For the binormal computation in the current position, our method uses the normal in the previous position as the “suggested” up vector. With a smoothly varying tangent and a sufficient density of points, this approach does not incur the case when the normal is parallel to the tangent. Therefore it becomes possible to reform tubular structures without being limited to bends of less than 90 degrees along the normal direction. In our visualizations, we always visualize the flow in its context, e.g., the boundary surface of the tubular structure, that we consider as the primary orientation cue. Therefore, this enhanced computation of the moving frame is also used in our prototype to implement a standard CCVR for the flow context. The CCVR method makes use of quads of user specified side length to bound the resampling of the original data on evenly spaced planes along and around the centerline (not at the least to prevent the resampling in regions where these planes intersect).

Physical space, tubular space and the straightened space

The centerline with its orthogonal cross-planes can be seen as a skeleton bounding the tubular flow. The main idea behind this work consists of using this skeleton to “superimpose” a new curvilinear grid on the data. This grid is used to perform a curve-centric reformation of the vector field, by transforming the vectors with the inverted Jacobian matrix of the grid in each sampling position [160]. This grid is also used to compute “reference”

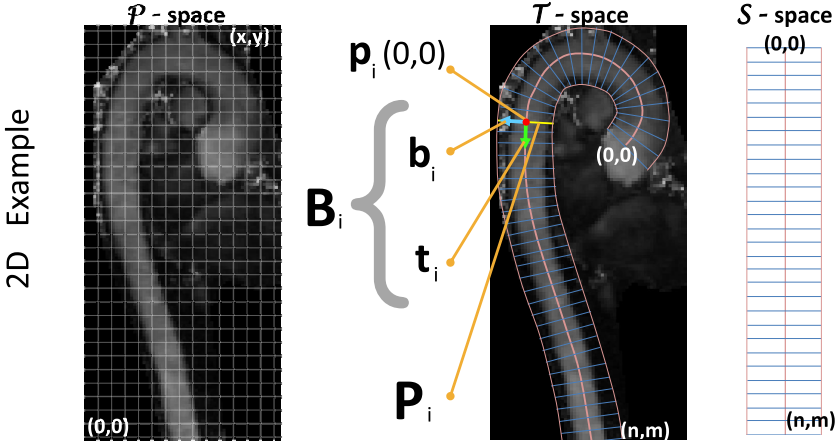


Figure 4: We consider three spaces: the data is given as a Cartesian grid (space \mathcal{P}). A curvilinear grid is constructed along and around the centerline (space \mathcal{T}), and after the reformation, this grid becomes a new Cartesian grid (in space \mathcal{S}).

intersection points between integrated lines, such as streamlines, and the cross-planes, in order to map each line to the straightened space.

Let us first formally introduce the three different spaces we are considering. The first space, \mathcal{P} , is the original physical space, in which the data, the centerline and the modified Frenet frame are defined. The second space, \mathcal{T} , is the tubular space defined by the moving frame. Finally, the straightened space, \mathcal{S} , is the space produced by the reformation, and it is a Cartesian grid.

Normally, \mathcal{P} is defined by the application, and in the cases presented here it is a Cartesian grid. \mathcal{T} , instead, is “traced” by the moving frame along the centerline, which generates a curvilinear grid. Assuming a subdivision of the centerline in n segments of equal length (the number of segments is controlled by the user), there are $n + 1$ evenly spaced points $\mathbf{p}_i^{\mathcal{P}}(0, 0)$ along the centerline, given in \mathcal{P} coordinates. For each i , $0 \leq i \leq n$, the $\mathbf{u}\mathbf{v}\mathbf{n}$ basis \mathbf{B}_i of the moving frame in the point $\mathbf{p}_i^{\mathcal{P}}(0, 0)$ is defined by

$$\mathbf{u} = \mathbf{b}_i \quad , \quad \mathbf{v} = \mathbf{n}_i \quad , \quad \mathbf{n} = \mathbf{t}_i \quad (1)$$

where, in $\mathbf{p}_i^{\mathcal{P}}(0, 0)$, \mathbf{t}_i is the normalized tangent to the centerline, \mathbf{n}_i is the unit normal and \mathbf{b}_i the unit binormal. The vectors \mathbf{t}_i , \mathbf{n}_i and \mathbf{b}_i are also defined in \mathcal{P} coordinates, and they are computed as described in Section B.3.1.

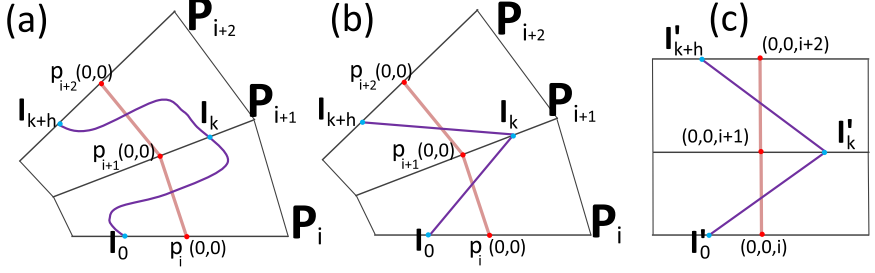


Figure 5: Intersections (in red) of the line traced from the point I_0 (a) skeleton of the line using only the intersection points (b). Straightened skeleton in S space, by performing the mapping from \mathcal{P} to \mathcal{S} of the intersections (c).

In every point $\mathbf{p}_i^{\mathcal{P}}(0,0)$, the plane \mathbf{P}_i , orthogonal to the centerline, is implicitly defined by $\mathbf{p}_i^{\mathcal{P}}(0,0)$ and \mathbf{t}_i (the normal vector of the plane). Furthermore, let $sector_i$ be the region enclosed between the two planes \mathbf{P}_i and \mathbf{P}_{i+1} .

To generate the tubular grid of radius r and resolution s using this moving frame, which creates \mathcal{T} , we define the grid points around each $\mathbf{p}_i^{\mathcal{P}}(0,0)$, lying in the plane \mathbf{P}_i , as

$$\forall x, y \in \mathbb{Z} : -s \leq x, y \leq s, \mathbf{p}_i^{\mathcal{P}}(x, y) = \mathbf{p}_i^{\mathcal{P}}(0, 0) + \frac{r}{s} x \mathbf{b}_i + \frac{r}{s} y \mathbf{n}_i \quad (2)$$

The edges of the curvilinear grid are then defined between points $\mathbf{p}_i^{\mathcal{P}}(x, y)$ and $\mathbf{p}_{i\pm 1}^{\mathcal{P}}(x, y)$, and between $\mathbf{p}_i^{\mathcal{P}}(x, y)$ and $\mathbf{p}_i^{\mathcal{P}}(x \pm 1, y \pm 1)$, forming hexahedral cells (see Figure 4 for an example in 2D). Equation 2 defines a mapping from \mathcal{S} to \mathcal{P} ; the inverse mapping from \mathcal{P} to \mathcal{S} of a point $[x, y, z]_i^{\mathcal{P}}$ lying on the plane \mathbf{P}_i is defined by

$$[x, y, i]^{\mathcal{S}} = \mathbf{B}_i^{-1}([x, y, z]_i^{\mathcal{P}} - \mathbf{p}_i^{\mathcal{P}}(0, 0)) + [0, 0, i] \quad (3)$$

Finally, \mathcal{S} is defined by the grid points of \mathcal{T} expressed with respect to their basis \mathbf{B}_i , forming a new Cartesian grid, that is the straightened grid \mathcal{T} . It should be noted that the space \mathcal{T} is given in \mathcal{P} coordinates, while it is parametrized in \mathcal{S} coordinates. In the following it is sufficient to only consider the two spaces \mathcal{P} and \mathcal{S} .

Centerline centric line straightening

With this approach the computation, e.g., by integration, of line primitives, such as streamlines, is performed in the original vector space \mathcal{P} . To straighten them, we use an algorithm that creates a parametrization of the points using the local bases from the moving frame. This algorithm performs a piecewise reformation of a line by using the planes \mathbf{P}_i , defined by

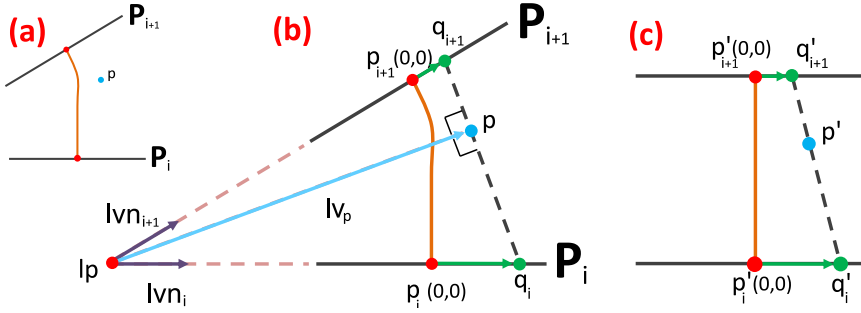


Figure 6: Example in $2D$ of a point p to be reformed, lying in $sector_i$ (a). Elements of the reformation, needed to compute q_i and q_{i+1} (b). Reformed p' in S space, computed through the points q'_i and q'_{i+1} .

the tangent of the moving frame, as reference (see Figure 5). These planes are defined in a discrete number of equidistant points along the centerline (see Figure 4). From Section B.3.1 we know how to straighten points that lie in planes P_i , using equation 3. To create a straightened *skeleton* of a line, integrated from a seed point $p_i^P(r, s)$ lying in plane P_i , we could compute all the intersection points of the line with the planes it intersects during the integration, and then transform these intersections from \mathcal{P} into S .

The following description of the tracing algorithm assumes that the first integration step goes in the direction of t_i , the opposite case is symmetric and we omit a detailed description here. First, let \mathbf{l}_k be the position of the integration front in \mathcal{P} coordinates after k integration steps. In the algorithm, we perform, at each integration step k , an intersection check against the next plane P_{i+1} , and, if it fails, against the current plane P_i , if the sign of the dot-product $[\mathbf{l}_k - \mathbf{l}_{k-1}] \cdot \mathbf{t}_i$ is negative or it is 0. If the dot product is positive we check solely against P_{i+1} . Intersection points are then reformed into S using equation 3. During the integration, we keep track of the current sector i , containing the integration front, and, at each intersection, we generate a reformed point using the formula described above, and we update the current sector.

Reforming also the points between two consecutive intersection points requires a mean to warp the space between two consecutive planes. Therefore we created a parametrization for points known to lie in a $sector_i$ based on the enclosing planes (illustrated in $2D$ in Figure 6). Let us assume, for now, that the two planes P_i and P_{i+1} are not parallel. Then, assuming that we want to reform the point p , the algorithm can be described as follows:

1. Compute the line L of the intersection between the two planes P_i and P_{i+1} .
2. Compute the vectors lv_i and lv_{i+1} , orthogonal to L , and going from L to the center points $p_i^P(0, 0)$ and $p_{i+1}^P(0, 0)$ of the quads lying on

- the two planes. Let \mathbf{lv}_i and \mathbf{lv}_{i+1} be the normalized versions of \mathbf{lv}_i and \mathbf{lv}_{i+1} .
3. Compute the vector \mathbf{lv}_p , orthogonal to \mathbf{L} , going from \mathbf{L} to the point \mathbf{p} . Compute also the point \mathbf{lp} as the intersection between \mathbf{L} and \mathbf{lv}_p . Let \mathbf{lv}_p be the normalized version of \mathbf{lv}_p .
 4. Compute the point $\mathbf{q}_i = \mathbf{lp} + \frac{\mathbf{lv}_i \cdot \|\mathbf{lv}_p\|}{\|\mathbf{lv}_p\| \cdot \|\mathbf{lv}_i\|}$. Similarly, compute \mathbf{q}_{i+1} .
 5. Compute the vector $\mathbf{vq}_i = [\mathbf{q}_i - \mathbf{p}_i^{\mathcal{P}}(0, 0)]$. Similarly, compute \mathbf{vq}_{i+1} .
 6. Transform the vector \mathbf{vq}_i to \mathcal{S} , by computing $\mathbf{vq}'_i = \mathbf{B}_i^{-1} \mathbf{vq}_i$. Similarly, transform \mathbf{vq}_{i+1} .
 7. Compute the point $\mathbf{q}'_i = [0, 0, i]^{\mathcal{S}} + \mathbf{vq}'_i$. Similarly, compute \mathbf{q}'_{i+1} .
 8. Compute the reformed point $\mathbf{p}' = \mathbf{q}'_i + [\mathbf{q}'_{i+1} - \mathbf{q}'_i] \frac{\|\mathbf{p} - \mathbf{q}_i\|}{\|\mathbf{q}_{i+1} - \mathbf{q}_i\|}$.

If the planes are parallel, it is sufficient to compute \mathbf{q}_i and \mathbf{q}_{i+1} as the intersection of the line $\mathbf{p} + s \mathbf{t}_i$ with the planes \mathbf{P}_i and \mathbf{P}_{i+1} respectively, and then start from point 5. Note that steps 1 and 2 are the same for each point in a *sector*_{*i*}, and can, in fact, be precomputed. This approach produces accurate line reformations, meaning that the positions along the reformed line in \mathcal{S} are the reformed positions along the line in the original space \mathcal{P} .

Centerline centric vector field reformation

Obtaining a local, and smoothly varying, coordinate frame for every point on a curve allows to perform a straightforward curve centric resampling for scalar volume straightening. However, to reform vector data, it is necessary to transform not only the vectors' magnitude, but in particular their direction. Transforming a vector \mathbf{u} , defined in the original space \mathcal{P} , into the vector \mathbf{v} , defined in \mathcal{S} , requires to compute the Jacobian matrix \mathbf{J} for the grid point of the space \mathcal{S} where \mathbf{u} is sampled. \mathbf{J} contains the partial derivatives of the grid (in \mathcal{P} coordinates) with respect to \mathcal{S} in the same point. Let $\mathbf{p}_i^{\mathcal{P}}(x, y)$ be a point in \mathcal{T} expressed in \mathcal{P} coordinates. Then, the Jacobian $\mathbf{J}(x, y, i)$ is defined as

$$\left(\begin{array}{ccc} \frac{\partial \mathbf{p}_i^{\mathcal{P}}(x, y)}{\partial x} & \frac{\partial \mathbf{p}_i^{\mathcal{P}}(x, y)}{\partial y} & \frac{\partial \mathbf{p}_i^{\mathcal{P}}(x, y)}{\partial i} \end{array} \right)$$

As the grid in the space \mathcal{T} is actually defined by our moving frame along the centerline, we know the grid vertices in the neighborhood of $\mathbf{p}_i^{\mathcal{P}}(x, y)$, as they are connected by the edges as defined in Section B.3.1. In any point of the grid in \mathcal{T} , the components $\frac{\partial \mathbf{p}_i^{\mathcal{P}}(x, y)}{\partial x}$ and $\frac{\partial \mathbf{p}_i^{\mathcal{P}}(x, y)}{\partial y}$ are given by the vectors \mathbf{b}_i and \mathbf{n}_i . Thus, the only component that has to be estimated to build the matrix $\mathbf{J}(x, y, i)$ is $\frac{\partial \mathbf{p}_i^{\mathcal{P}}(x, y)}{\partial i}$. This term can be approximated, for example, by using one of three differential operators: central differences,

forward differences or backward differences, as described also by Sadarjoen et al. [160]. For our purposes, we use a mixed forward and backward difference operator, depending on the sign of the dot product of the vector $\mathbf{v}_i^{\mathcal{P}}(x, y)$, sampled in the point $\mathbf{p}_i^{\mathcal{P}}(x, y)$, with the normal \mathbf{n}_i . This way we introduce less smoothing, compared to using central differences.

We therefore modify the CCVR method [93] to handle vector data, using the following equation

$$\mathbf{vec}_i^{\mathcal{S}}(x, y) = \mathbf{J}^{-1}(x, y, i)\mathbf{vec}_i^{\mathcal{P}}(x, y) \quad (4)$$

If $\mathbf{p}_i^{\mathcal{P}}(x, y)$ is not a grid point of the data space \mathcal{P} , $\mathbf{vec}_i^{\mathcal{P}}(x, y)$ has to be reconstructed using an interpolation scheme. In case of vector data this operation can be done in different ways. The simplest approach is to perform a per-component trilinear interpolation. However, in case of a vector field, this might not be the best solution, as it linearly interpolates only the direction of the vectors, not the length. A different approach, that we adopt in our prototype, consists of using spherical linear interpolation (slerp) using quaternions, in order to interpolate also vector lengths.

This method generates a straightened vector field, and primitive integration as well as other flow visualizations can be performed directly in \mathcal{S} , without the need of subsequent reformation. However, due to numerical inaccuracies, this approach and the one presented in Section B.3.1 might not lead to identical results. We have compared this approach with the one described in Section B.3.1, and the results are presented in Section B.4.3

B.3.2 Side-by-side straightened flow visualizations

By *complementing* the visualization of the original data with a juxtaposition of views of the straightened tubular flow, we aim to, first, provide a common axis for the alignment and co-registration of different views of the data, to easily relate them to each other. This also allows to create compact visualizations that give good overviews of the data, even combining different visualization techniques. Third, we want to statically convey the data variations over time, in case of unsteady flow datasets. Last, we want to help comparing different aspects of a dataset (such as different time points, or different descriptors), or even different datasets (as in population studies). In the next Section we describe a set of techniques to handle such straightened views properly, in order to create side-by-side straightened visualizations that fully exploit the possibilities that this method offers.

Visualization design and layout

When assembling the visualization, particular attention must be put in the combination of the views. First, the straightening axis in the views should

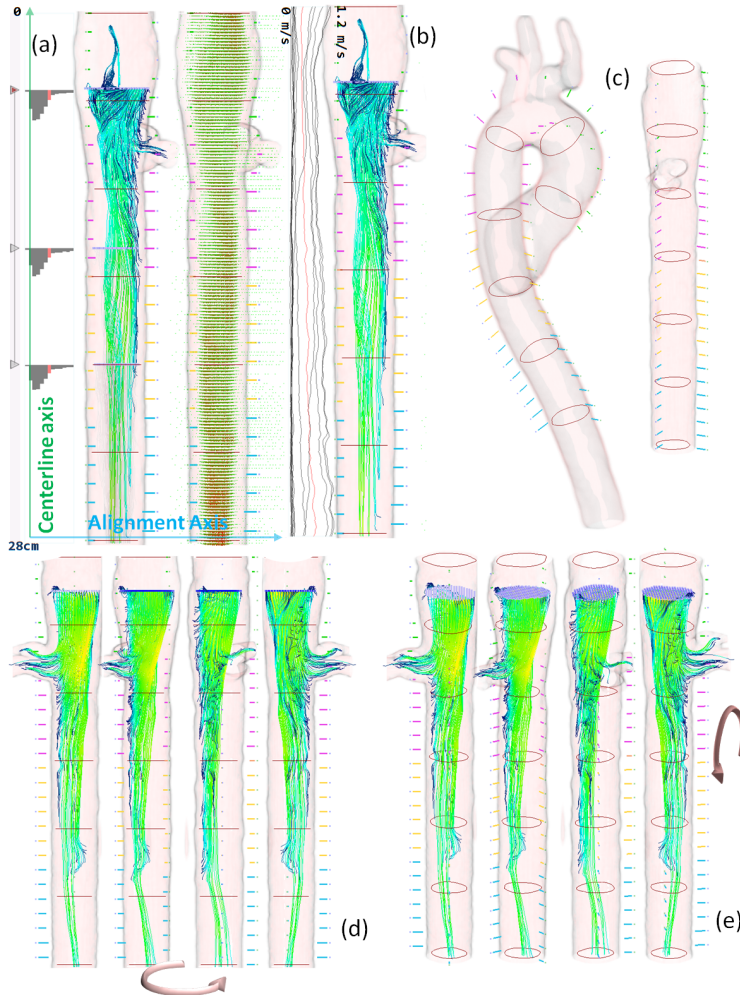


Figure 7: Design approaches to a side-by-side visualization of straightened tubular flow: straightened views should be aligned to one of the screen axes, and juxtaposed along the other. The first axis also serves to place navigational widgets to interact with the visualization along the centerline. The second axis is used to relate different views to each other. Informative visualizations, such as a line graph or a histogram of the flow magnitude can also be placed along the centerline, to provide quantitative information (a,b). Orientation cues are needed for orientation: we use volume rendering of the physical context, with contours, to convey the physical space. For additional orientation cues, we add glyphs (c). Interaction with the visualization should be modified to allow only meaningful camera transformations. We use only rotations around the two axes used for the alignment (d,e).

be aligned to one of the screen axes, in order to facilitate the juxtaposition and the alignment of several views. Having the reformed centerline aligned to one of the screen axes also allows to minimize the space in between different views. This alignment also allows to combine visualization of the actual data (such as standard flow visualization techniques) with more abstract visualization techniques, such as a line graph plotting certain quantities along the centerline (see Figure 7(a,b)). In such setup, it becomes possible to use the centerline axis as navigational tool: it can be used for operations such as cross-section placement and movement, and length measurement (see Figure 2).

Second, special attention must be put in conveying the shape of the reformation, in order to enable the viewer to easily relate positions and directions in the reformed view to positions and directions in the original space. We propose to use two kind of orientation cues. The primary cue is the rendering of the reformed tubular structure around the flow as its spatial context. To do this, we perform volume ray casting of the straightened context, instead of rendering the extracted isosurface. This allows us to perform fast and correct depth-buffer based alpha blending with the integrated geometric primitives, such as streamlines, in a single (modified) ray casting pass, without the need of performing expensive multi-pass rendering techniques, such as depth-peeling. In addition, we propose to use a number of “i-shaped” glyphs along the projection of the normal and of the binormal onto the flow bounding structure (see Figure 7). The body color of these glyphs encodes the distance from the beginning of the centerline, while the dot color encodes the projection axis (green dot = glyph above the normal, blue dot = glyph above the binormal). In this way we help the user to orient and understand from which viewpoint she is looking at the flow. These glyphs, in combination with a specified number of isocontours of the tubular structure, also help the user relating a region along the centerline “axis” between the conventional view and the reformed side-by-side visualization.

The proposed side-by-side layout also introduces some challenges in the interaction process with the visualization. Rotating the visualization with the classical joystick or trackball paradigms, in particular, might become unfeasible. For this reason we enable only 2 rotation methods: per-view rotation around the centerline axis, and global rotation around the other screen axis (see Figure 7). This method proved to allow thorough exploration of the straightened data, while, at the same time, being intuitive and error-proof, preventing that the user might “get lost” while interacting with the visualization.

Straightened side-by-side visualization

In this section we illustrates some of the visualization opportunities offered by juxtaposing straightened flow views. The most obvious opportu-

nity is to visualize many timesteps of an unsteady flow at the same time, aligned along the same axis, as shown in Figure 2. In this way it is possible to convey the temporal evolution in one single, compact visualization, that also allows to immediately relate the same region (position along the centerline) of the flow in different timesteps.

Another possibility consists of generating a compact, thorough view of the flow from different angles (see Figure 7(d,e)). This is particularly useful when inspecting tubular structures in complex shapes, for which few projections might still not make all the flow content visible. With only few views of the straightened flow from equiangular view points it becomes possible to inspect the flow from all possible sides.

Finally, this technique permits the juxtaposition of different types of visualizations side by side and relate them with each other. As an example, in Figure 8 we show a composition of pairs of visualizations, showing pathlines at each timestep next to the representation of the vector field at the same timestep. The clear advantage is again the simplicity of spatially relate the different aspects of the same data (the timestep). In Figure 2(right) different aspects of the same timestep (streamlines integration from different seeding planes) are also placed side by side, highlighting the contribution of each seeding plane to the result, on the left side.

B.4 Realization and evaluation

To use our technique, we developed a prototype, making partly use of VTK. In the prototype we implemented streamline and pathline tracing on the GPU, using geometry shaders [180]. We also implemented abstract visualization techniques such as line graphs and histograms (of averaged velocity), to demonstrate the simplicity of combining classic flow visualizations with other data visualization methods in an intuitive way. The proposed approach can, however, be also used with other types of flow visualization. We used our prototype to successfully visualize two datasets from different fields, which we describe in the next sections.

B.4.1 Aortic flow visualization

Magnetic Resonance Imaging (MRI) is one of the fastest developing imaging technologies in medicine. Recently, improved time-resolved 3D Phase-Contrast MRI (PC-MRI) has been successfully used to image the blood flow in the human body. Bock et al. [15] provide an overview of this imaging modality describing the characteristics of the generated data. The dataset we visualize is a vector field of a human aorta, specified on a Cartesian grid with a resolution of $192 \times 144 \times 24$ voxels in x , y and z respectively, containing 13 time steps acquired at a time resolution of about 50 milliseconds. The spatial resolution of the scan is [1.67mm, 1.67mm, 3.5mm] in x , y and z ,

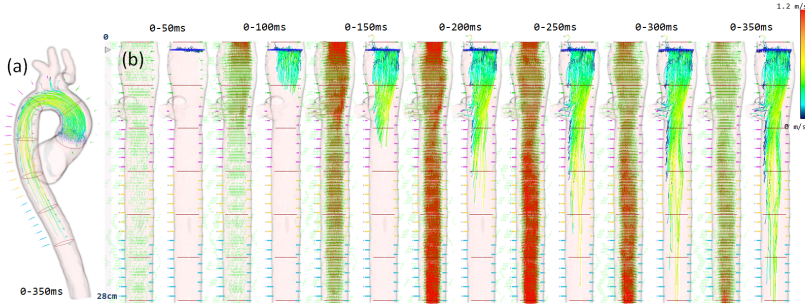


Figure 8: Timesteps from 0 to 6 of the aorta dataset, visualized with pathlines and glyphs illustrating the vector field. Each pair of views shows the glyphs rendering of the vector field at the last time point stated on top, and the pathline integration from time 0 to the last time point.

for an imaged volume of $32 \times 24 \times 8.5$ cm. To simplify the handling of the significant anisotropy of this dataset, we decided to upscale the dataset to an isotropic grid beforehand. The aorta was segmented as described in Section B.3, and the computed centerline of the arterial wall measured about 30cm. The centerline was subdivided in segments of voxel-length to minimize resampling artifacts, and the straightening was performed using quads with a side length of approximately 7.5 cm, with a transversal resampling resolution of 49×49 voxels (approximately the same resolution of the data). Figure 1 shows all the timesteps side by side using streamlines with a fixed seeding grid and 3 seeding planes, presenting the whole time-lapse with static time dependency. In Figure 2 we investigate a single timestep, by separating the seeding body into different views, to prevent streamlines overlapping. Finally, In Figure 8 we show the evolution of pathlines integration, from timestep 1 to 7, together with the vector field at each timestep. In this way we effectively combine different methods in a side-by-side visualization of the flow.

B.4.2 Exhaust system flow visualization

This dataset contains the simulation results of an exhaust system with 3 collectors from the cylinders and a common rail for the emission. The dataset is a vector field specified on a Cartesian grid, with resolution of $133 \times 82 \times 68$ voxels in x , y and z respectively, over 30 time steps. We computed the centerline starting at the beginning of the first collector to the end of the rail, thus analyzing the behavior of this part of the system. The centerline was subdivided again in segments of voxel-length, and the straightening was performed using quads of radius 20 voxels. In Figure 10 we visualize a time lapse of the flow, from timestep 0 to timestep 17, using streamlines, traced from 3 seed planes placed after each collector. The

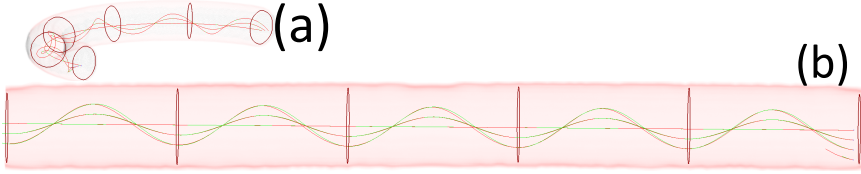


Figure 9: Synthetic dataset, a curved tube containing helical flow, with four streamlines seeded at the beginning of the tube, along the radius (a). The same dataset, straightened, with streamlines integrated in the reformed flow (red) and in the original flow and then deformed (green) (b). The average distance between the pairs of lines is 0.10 voxel, while the maximum distance is 0.21 voxel.

image clearly conveys the valves opening sequence (ts 1 = 2, ts 6 = 1, ts 14 = 3), and the curve of the decreasing velocity after the closure.

B.4.3 Performance and Error Analysis

We have compared the performance of standard streamline integration performed on the reformed vector field with the approach presented in Section B.3.1, using a CPU implementation of both algorithms on an Intel Core2 2.4ghz processor. We seeded 1000 streamlines on plane P_0 , the beginning of the centerline, on both the aorta and the manifold dataset, and used 1000 integration steps, with a step size of 0.25 voxel, on 10 different timesteps of each dataset. After averaging of the results, the standard integration took 0.65 seconds to complete this task seconds, while the line straightening method required 3.75 seconds. The second algorithm also showed higher variance in the results. This behavior can be explained considering that some timesteps contains low velocities, and the integration crosses only few sectors along the centerline, lowering the computational complexity. The conclusion is that the accurate approach is about 6 times slower than the other one.

We then carried out an error analysis to compute the average and maximum gap between lines traced with the two approaches, when they are seeded at the exact same locations. We measured the error by stepping along each pair of lines (the one integrated in the reformed field and the one straightened), using a step size of 0.25 voxel. At each step, we measured the distance between the corresponding locations along the two lines. The table below reports the average and maximum distance (expressed in voxel units) for the different datasets, averaged over 1000 streamlines and traced on 10 different timesteps. For this analysis we also added a synthetic dataset proposed by Roth and Peikert [158] (see Figure 9), consisting of a helical flow inside a bent pipe, for which the centerline is known. This analysis shows that the measured PC-MRI dataset is the one where the vector field reformation leads to the largest error. One of the reasons could be

	Aorta	Exhaust Manifold	Bent pipe
Average Diameter	23	24	18
Average Error	1.17	0.39	0.33
Maximum Error	1.83	1.07	0.72

Table 1: Average and maximum distance between streamlines integrated in the reformed vector field and streamlines straightened after the integration in the original field. The values are expressed in voxels.

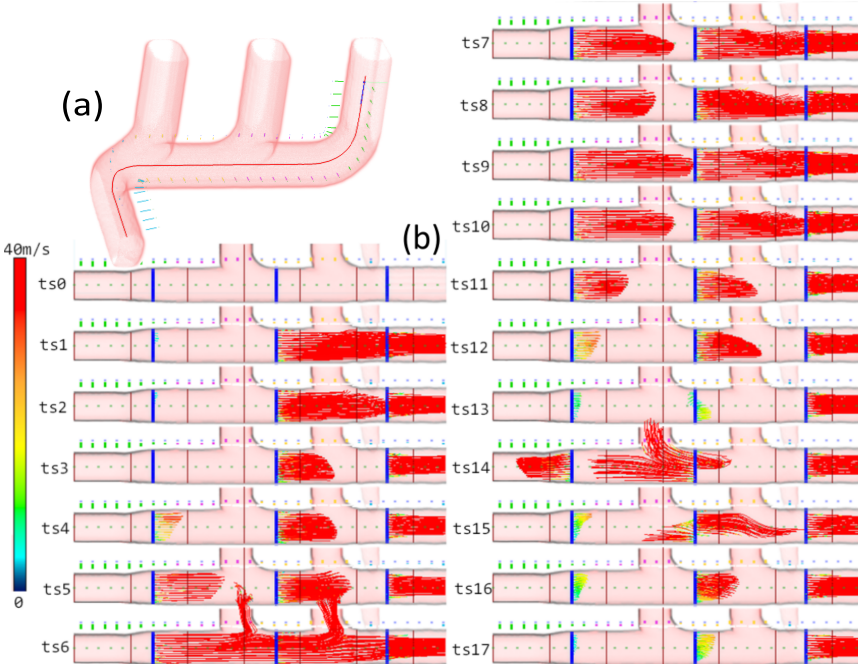


Figure 10: The exhaust system, volume rendering (a) Static time lapse visualization of the straightened flow in the exhaust system dataset, timesteps from 0 to 17 (b).

that the extracted centerline is not 100% accurate, and therefore the cross planes do not result perfectly orthogonal to the vessel. This may lead to inaccurate Jacobian computation for the two transversal components, that are taken directly from the moving frame. We can conclude that a crucial aspect of our technique is a robust and accurate centerline extraction algorithm, to be able to accurately integrate the reformed vector field.

B.4.4 Evaluation

The Cardiovascular MRI Group at the University Medical Center Freiburg, Medical Physics department, very kindly provided us with an informal evaluation of the presented technique, that we demanded in order to understand how possible end users would benefit from it. This evaluation is composed of general impressions and of answers to specific questions we asked. In general, the reformatting of the aorta has been seen as potentially useful to compare some hemodynamic parameters (such as wall shear stress or pressure differences), also across a population. However, in this case one would need some kind of aortic atlas, and then map the dataset onto this atlas (a starting point for this mapping could be actually found in the work of Ropinski et al. [156]). There was also some uncertainty about how the visualization would look in presence of an aneurysm or a stenosis. The group also believe that medical personnel is more accustomed to seeing the blood flow in its original context, and would, therefore, require a certain training in order to profit from the proposed method.

The specific questions we asked to the Cardiovascular MRI Group in Freiburg were what kind of visual comparison are they interested in, whether this approach would ease the comparison of integrated lines in the aorta, and what are other parameters typically investigated. Then we asked whether they think that physicians would profit from this technique as well, and what do physicians generally look at, in such data. According to their answers, at the present they do not perform that much comparison visually, but the presented approach could be useful to compare hemodynamic parameters, while other typical parameters of interest along the vessel are helicity and vorticity. The presented approach has been seen as definitely easing the comparison of integrated lines from their point of view, but, from a medical point of view, physicians are currently very accustomed to the original shape of the vessel. Last, visual features of interest from the medical point of views are helices, vortices, and retrograde flow at late timepoints.

From this evaluation we can conclude that domain experts could profit from this flow straightening techniques, but some training is necessary. However, there have been other cases of reformation techniques which required a certain learning, before being embraced in the clinical routine, such as the curved-planar reformation of the human vessel tree [75].

B.5 Summary and conclusions

In this paper we present a general solution for producing straightened tubular flow views by applying standard flow visualization techniques to a straightened vector field along the centerline of the tubular object. In addition, we presented multiple techniques for composing such views, in order

to form straightened side-by-side visualizations. We used our method to visualize two different tubular flow datasets, showing that the technique is generally applicable for any dataset where the flow under inspection streams within a tubular structure. With the generated side-by-side visualizations we achieved improvements over standard techniques, in terms of efficiency in the usage of the available visualization space, and in terms of ease in the comparison of the different aspects of the data. We received a positive feedback by domain experts, that let us conclude that it is worthwhile, in certain cases, to choose an alternative way to look at the data over the conventional ones, to exploit the power of visualization. Limitations of our approach are, at the present, the handling of structures with unnatural narrow bends, when cross planes intersects each other within the lumen of the pipe, and the handling of structures with major bifurcations. Both of these issues require further investigations. As a future work, we also plan to investigate more thoroughly the perception of flow straightening for longer, more complex structures and to obtain a more formal evaluation.

Acknowledgements

We are very grateful to Jelena Bock and to all the Cardiovascular MRI Group, Medical Physics at the University Medical Center, Freiburg, for the PC-MRI dataset and the very valuable feedback provided. The exhaust manifold dataset is courtesy of AVL GmbH, Graz, Austria, and we thank Alan Lež, Krešimir Matkovic and Philipp Muigg for helping us to import the data. Furthermore, we want to thank Andrea Brambilla, Ove Daae Lampe, Július Parulek, Armin Pobitzer and Eirik Vik for all the fruitful discussions together. Parts of this work originate in the EC-funded SemSeg project (FET-Open, grant number 226042), with the support of the MedViz network in Bergen, Norway (PK1760-5897-Project 11).

Interactive Visual Analysis of Heterogeneous Cohort Study Data

Paolo Angelelli¹, Steffen Oeltze², Judit Haász³, Cagatay Turkey¹, Erlend Hodneland³, Arvid Lundervold³, Astri J. Lundervold⁴, Bernhard Preim², Helwig Hauser¹

¹Department of Informatics, University of Bergen, Norway

²Department of Informatics, University of Magdeburg, Germany

³Department of Biomedicine, University of Bergen, Norway

⁴Department of Biological and Medical Psychology, University of Bergen, Norway

Abstract

Cohort studies in medicine are becoming more common, to enable the study of medical hypotheses in large samples. Often, a large amount of heterogeneous data is acquired from many subjects. The analysis is usually hypothesis-driven, i.e., a specific subset of such data is studied to confirm or reject specific hypotheses. In this paper, we demonstrate how we enabled the interactive visual exploration and analysis of such data, helping with the generation of such hypotheses and improving the process of validating them. We propose a data-cube based model which allows to handle partially overlapping data subsets during the interactive visualization. This enables seamless integration of the different measures, and linking of spatial and non-spatial views. We implemented this model in a prototype,

After a first round of reviewing, a major revision is now in preparation for the journal *Computer Graphics and Applications*

and analyzed a cohort study on cognitive aging, comprising information of white matter tracts, gray matter regions, and neuropsychological measures acquired at two time points.

C.1 Introduction

Cohort studies in medicine are becoming increasingly common, partly due to the availability and recent improvements in medical imaging technologies. Such studies are used to evaluate medical hypotheses in a sample, either healthy or presenting a common pathology, in order to gain a better understanding of healthy aging in contrast to pathological changes, or to assess the progress of a pathology. Cohort study data is often acquired over longer time periods and following strictly defined protocols. Normally, they are designed to deliver data which, later, can be a basis for evaluating further sets of hypotheses.

However, while there are means to evaluate specific hypotheses, based on such cohort study data, often involving accordingly designed data extraction, transformation, and fusion approaches, there is a lack of technology that would support the flexible and open-ended exploration of such data, mostly because of its highly heterogeneity. Integrating all the available data within one visualization tool that allows to seamlessly combine them on demand is expected to help the experts to explore heterogeneous cohort study data more easily, to allow for an improved hypothesis generation, and, not at the least, to speed up their current research workflow.

The exploration and analysis of cohort study data generates specific new challenges for visualization. In this article we characterize them, in particular in relation to the substantial heterogeneity of the data, and exemplify how a tailored approach enables hypothesis generation as well as the swift analysis of relations between otherwise unconnected data parts. We describe our solution in terms of a more general data-cube based model that can also be adopted in similar situations of highly heterogeneous data.

C.2 A Typical Scenario of Heterogeneous Data in a Cohort Study

One goal of this work was to create a solution that would enable the explorative visualization and analysis of data that was acquired as part of a longitudinal study on cognitive aging. During this study, more than 100 healthy individuals (mean age 60.8 (7.8), 65% females at inclusion) were recruited through advertisements in local newspapers. At inclusion, all the participants were interviewed before inclusion, to exclude those reporting previous or present neurological or psychiatric disorders, a history of substance abuse, or other significant medical conditions. The neuropsychological evaluation confirmed that the participants showed no symptoms indicating mild cognitive impairment (MCI) or dementia. Each participant was examined twice, first in year 2004/2005, and then in 2008 (a third wave is at the moment about to be completed). The participants were subjected to neuropsychological testing, genetic analysis (not used in this work), and multimodal MR imaging. The result of each examination consisted of data on white matter fiber integrity, as expressed by fractional anisotropy computed from diffusion tensor imaging (DTI), cortical and subcortical gray matter measures, automatically calculated from structural MR images, and a number of neuropsychological tests, including the California Verbal Learning Test–Second Version (CVLT-II), the Color–Word Interference Test (CWIT), the Digit Symbol Substitution Task from WAIS-R, and the Mini Mental State Exam (MMSE). In addition, multiple quantitative measures for the white matter fiber bundles and the gray matter segments were extracted: different anisotropy measures for the bundles, and volume, thickness and area measures for the brain regions. To summarize, each examination (per subject and year) consists of:

- white matter fiber bundles with anisotropy measures. Each individual fiber was divided into 100 segments of equal length for the derivation of associated measures.
- gray matter cortical and subcortical regions with quantitative measures for each region.
- scores from different neuropsychological tests.

For a detailed study protocol and previous results from this longitudinal study see, e.g., Ystad et al. [199].

A heterogeneous dataset

Resulting from this study, a number of measures related to different aspects are available. One specific challenge with respect to data exploration and analysis is that their domains overlaps only partially. For example, how should one combine, in a scatterplot, fractional anisotropy, specified

for each segment of the fiber bundles, with thickness of the cortex, available for each cortical region? In short, this partial incompatibility of the data domains proved to be one – if not *the* – key challenge of this work.

Physical and abstract data

For certain aspects such as white matter fiber bundles and gray matter regions, there are both quantitative abstract measures (such as fiber anisotropy or cortical region thickness), and physical (anatomical) data of the bundles trajectories, or brain regions meshes. While the analysis is often performed on the quantitative measures, it also becomes necessary to occasionally fetch and inspect the related anatomical data, which can, for example, explain data outliers.

Analysis goals

When designing a solution for visualization of such data, there is a dual goal: on one side, it is important to enhance the data exploration process, in particular in those aspects not yet investigated, and possibly provide enough information to generate new hypotheses and subsequently verify them. On the other side, it is also important to enhance the process of hypotheses verification by easing the extraction of the aspects of interest from the dataset, and to investigate the relation between them.

C.3 Related Work (goes in a box)

While the vast majority of visualization research – in particular also medical visualization – was (and still is) focused on the visualization of individual datasets, the visualization of data from population studies has not been a research topic until recently. One recent exception is the work by Bruckner et al. [19], who presented a system to retrieve and visualize anatomical brain data of fruit flies, covered in a large database of such flies brains. This system enables a novel way to perform visual queries, combined with a volume rendering solution called Maximum Intensity Difference Accumulation (MIDA). Longitudinal medical imaging datasets are analyzed in the work by Durrleman et al. [36]. The authors investigated the variability of the data by devising a regression model that fits the data of a single subject over time. They use their framework to estimate a spatio-temporal atlas from the data. They analyze the morphological evolution of hominids' skulls and the growth of certain brain regions. More recently, Steenwijk et al. [169] presented a novel visual analytics framework to query and visualize data from a cohort study on neuropsychiatric SLE, consisting of imaging and non-imaging data for each subject. Their approach was to preprocess and store the imaging and non-imaging data

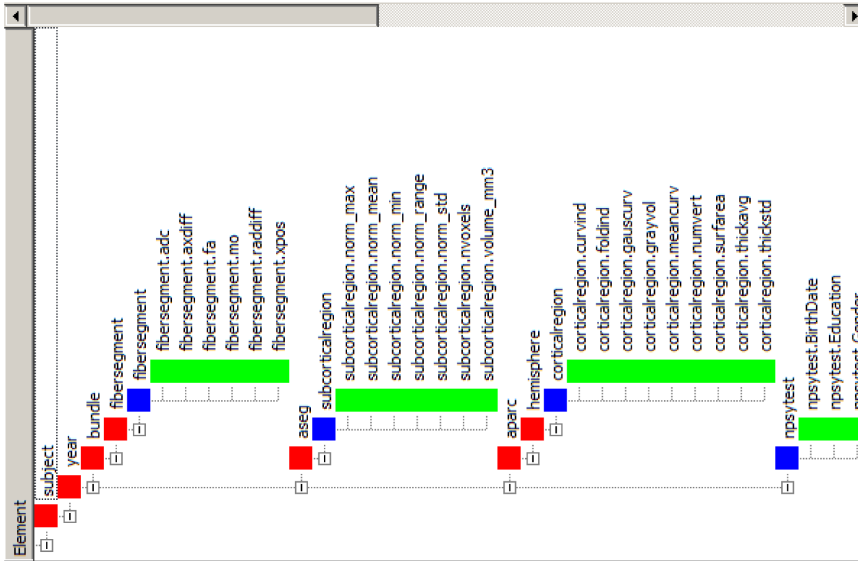


Figure 1: A tree visualization of the dimensions (red), measures (green) and entities (blue) present in the cohort study data-cube collection. The dimension hierarchy is not inherently present in the data, but has been derived according to the number of occurrences of each dimension in the database. This hierarchy is used only for presentation, as the presented model makes no assumptions on a hierarchy of dimensions, and can treat all the dimensions equally.

in a searchable database, to which a visual interface would perform dynamic queries.

More generally, quite a number of visual analysis methods have been proposed for the analysis of higher-dimensional and heterogeneous data. One relevant related solution was presented by North et al. [126], who introduced visualization schemas to achieve the concurrent analysis of different sources of information in relational databases. Their system offers opportunities to construct coordinated visualizations in a similar fashion as when constructing relational data schemas. More recently, Weaver uses a method called cross-filtered views [193] to interactively drill down into multidimensional relations between multiple datasets. In his method, different variables are visualized in particular views and brushes in these multiple views are cross-filtered to discover complex relations in the data.

C.4 A Data-Cube Based Model To Enable Interactive Visual Analysis

Storing and accessing the data acquired with such studies in a fast and flexible way is the first and perhaps the biggest challenge in designing an

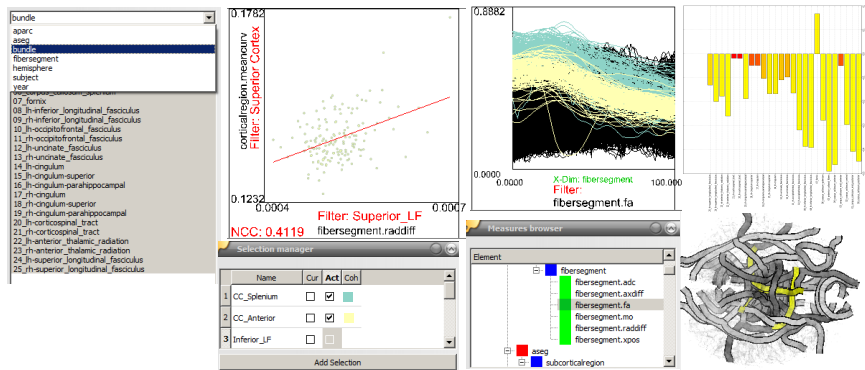


Figure 2: Screen-shot of the prototype of the proposed model. The Measure Browser lets the user drag desired measures into a view, the Selection Manager allows to add new selections, activate them, enable one of them for editing, and drag them into views, to be used as filters. The Dimension Brusher (left) enables slicing the data cubes in the data collection, while the other views can be seen as projections of the data, and allow a more advanced definition of the selections, by means of brushing ranges of measures. Finally, the VTK Fiber Model view represents a selection in the anatomical context using a brain model.

interactive visualization system targeted at this problem. Organizing the data in a relational database, similarly to Steenwijk et al. [169], is probably the first solution at hand, and probably the easiest to design. However, it is inflexible: the database schema is bound to the particular structure of a specific study, and has to be redefined for different studies, as well as the logic for data access. Moreover, using a relational database does not provide the required performance to enable interactive exploration of such large data. In Polaris, Stolte et al. [170] showed how data can also be organized for visualization as n -dimensional data cubes, in data warehousing called OLAP cubes (for On-Line Analytical Processing).

Dimensions, measures and entities

In data warehousing, OLAP cubes are constructed using categorical attributes as dimensions, while quantitative numerical values are stored as measures. The dimensions and measures can be thought as independent and dependent variables, where dimension coordinates are used to access the measures. Practically, after assigning an order to the dimensions, a data cube can be implemented as an in-memory n -dimensional array. This allows, for example, a faster data access, as compared to keeping the data in a relational database. In our model we organize the cohort study data in data-cubes. In this way, for example, a measure of a segment of a white matter fiber bundle, say, fractional anisotropy, is represented as a floating

point data cube consisting of four dimensions: *subject*, *year*, *bundle*, and *segment*. In principle, these dimensions do not have any embedded hierarchy, (they are independent). However, if we want to have a dimension hierarchy to, for example, represent the data in a tree-like visualization (as shown in Fig. 1), we could define the dimensions that occur most often as root nodes, and then proceed with the dimensions having less occurrences. In case that two or more dimensions have the same number of occurrences (in our example, this is the case with the dimensions *subject* and *year*), it is sufficient to define an arbitrary order among them. Having defined such a hierarchy, it is possible to represent the measures in our cohort study data like in Fig. 1. Compared to the model as proposed for Polaris, we also introduce a third type of element, called *entity*. An entity can be thought of as a row in a database table, and quantitative row fields are then the measures for that entity. In our example, the measure *fibersegment_fa* is related to the entity *fibersegment*. In our model, an entity takes the place of the measures attached to it, when it comes to defining a data selection, an operation that is described further below.

Seamless dimension aggregation

One of the advantages of having the measures stored in data cubes is that we are able to automatically compute the common dimensions of two or more measures by simply intersecting the dimensions' set of the measures, without having any prior knowledge of the relations between measures (as necessary when using a relational database model for the data – the system would then need to know about the database schema, together with a complex logic for performing the operations). In our model, when multiple measures are combined in a visualization (e.g., in a scatterplot, or a parallel coordinate view), each measure is aggregated across those dimensions not belonging to the intersection. This operation is also referred to as the *projection* of a data-cube [170] (see Fig. 3). There are several options for the aggregation operator (usually estimating a statistic of the data), but for the moment we can simply think of using the average operator as aggregator.

Fig. 4(left) shows a scatterplot of two measures, i.e., the radial diffusivity of all fiber bundle segments versus the mean curvature of all cortical brain regions. As in Fig. 1, the common dimensions of these two measures are (*subject*, *year*), therefore each point in the scatterplot represents a single examination, while its position along the x axis represent the average radial diffusivity over all fiber segments of all bundles of the subject's brain during that specific examination. On the y axis, the position represents the average mean curvature over all the cortical regions of the subject. In our framework we implemented a drag-and-drop interaction model, where it is sufficient to drag the desired measures into a view to obtain the aggregation (if necessary) and the visualization. In certain cases, it is also useful

to change the level of detail. In the situation above, for example, we might want a point to represent a single year of examination, aggregated across all subjects, to see if the overall values decrease over time. To allow this, we propose to give the user the opportunity to toggle which of the common dimensions should be kept during the aggregation, and which not, thus performing something similar to a *roll-up* operation. The difference with a classical roll-up operation is that there is no hierarchy in the dimension structure, and it would be possible to disable any dimension in the set.

Selections and selection-based filtering

So far, we are able to create projections of a measure by aggregating over entire dimensions. Obtaining the average of a measure over a whole brain, however, may not always be enough to answer specific questions. To enable a more focused analysis, filtering and/or selection techniques can be

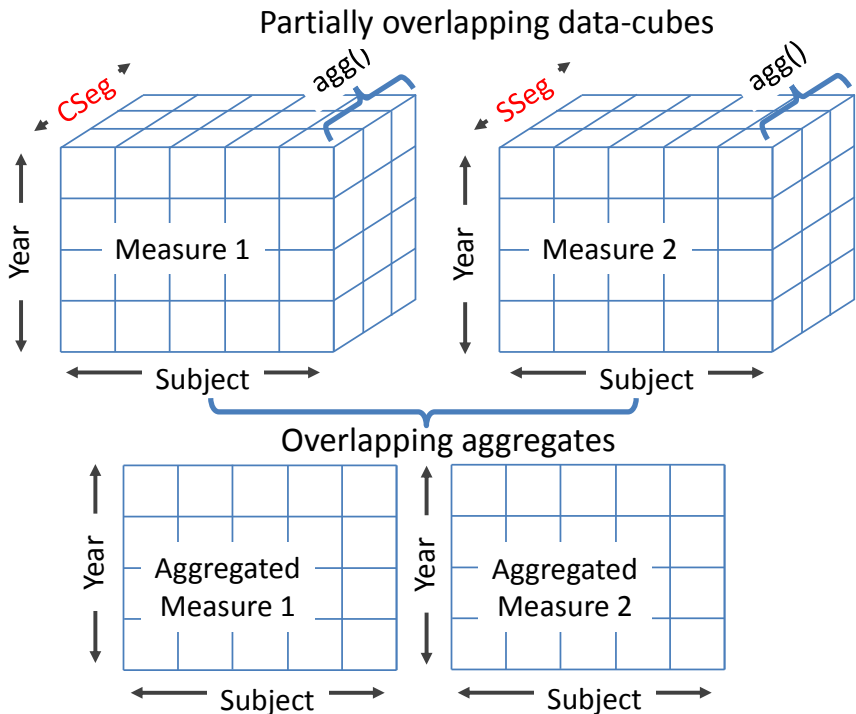


Figure 3: Projecting two three-dimensional measure cubes (e.g., thickness of cortical regions and volume of subcortical regions) on the common dimensions. The dimensions which are not common (in red) are processed using a statistical estimator (e.g., average).

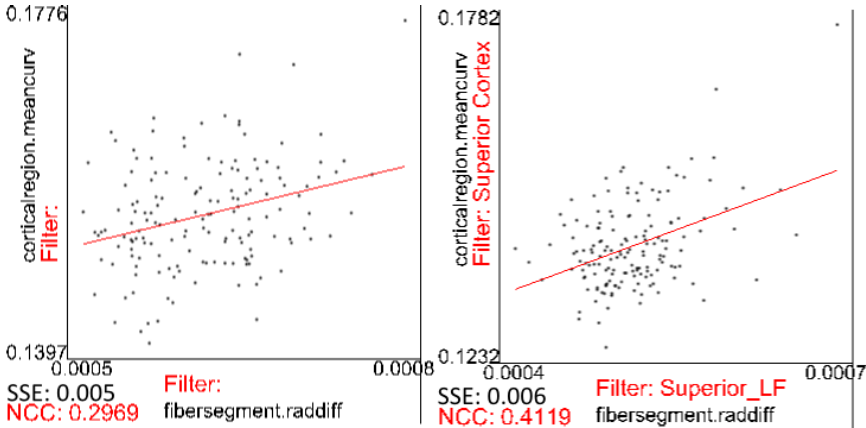


Figure 4: (left) Radial Diffusivity of the all the fiber bundles opposed to the mean curvature of all the cortical regions in a scatterplot, for each examination (meaning a pair subject, year, the common dimensions of these two measures). (right) The same measures, with the radial diffusivity now filtered using a selection containing the superior longitudinal fasciculi, while the mean curvature of the cortical regions is filtered with a selection containing the superior cortical regions, showing a higher correlation, and suggesting the hypothesis that these two aspects are related.

used in order to restrict the processed/visualized data to the focus of the analysis. An example is the Polaris specifications [170] for defining selections. Interactive visual analysis has also introduced the concept of brushing, a visual method to select items with certain characteristics (e.g., fitting a certain range on specific measures), by defining a visual brush over a view on the data. Normally, this brush gets transformed into a structure like a data-cube itself, where each item is tagged either with a binary or with a percentage value. In our case, we have an additional challenge: we have to tag all those items in the collection sharing at least one dimension. In this case, an extension of this brushing paradigm is needed. In our model, a brush on one entity (to which the brushed measure belongs) is propagated to all the other entities in the collection that share dimensions with the brushed one, by first computing a projection of the brushed entity using the common dimensions with the other ones. This projection of the brush is performed using the *max* operator, which eventually tags the items in these projections that have been created out of at least one tagged item. Using the *percentage* operator, instead, would produce a non-binary measure of what percentage of items has been tagged using the specific common coordinates, resulting in a smooth value of the Degree-Of-Interest (DOI).

This approach gives the user more flexibility wrt. selecting items, and multiple selections can also be combined using Boolean logic. These se-

lections can be visually highlighted in the views. In our model, they can be used also for another purpose: since most of the views are built upon aggregated data-cubes, this aggregation can be steered, or *filtered*, using an item selection – see Fig. 4 (right) for an example). By setting a selection as aggregation filter, the aggregation is performed only using the items that are selected in the filter. In this case, selections containing smooth DOI values are treated as binary.

C.5 Linking Abstract and Spatial Data

Sometimes it is of interest to relate abstract information to the brain’s anatomy. A practical example would be showing where, in the anatomy, the parts of the white matter fiber bundles within a certain range of anisotropy, or having certain properties (e.g., sensitivity to aging) are located. Once these segments have been determined, they must be related to the brain’s anatomy. The problem here is that we are dealing with entities belonging to many different brains, therefore there is the need of a sort of anatomical aggregation.

Visualizing aggregates in anatomical space: using an atlas

To represent statistical information for a selection in anatomical space, we propose to use an anatomical atlas of the brain onto which these aggregated statistics can be mapped and visualized, for example using a color encoding. For this purpose, a template brain together with its coarse segmentation into white and gray matter as well as a more fine-granular parcellation of the cortical and sub-cortical white and gray matter are needed. Furthermore, a geometric representation of the fiber tracks is required. Since the display of each individual fiber in every fiber bundle across all subjects (>20,000 fibers in total, per subject) results in a highly cluttered visualization (see Fig. 5a), we propose to compute a representative fiber for each fiber bundle. For simplification purposes, we so far treat the individual data of a representative subject as an atlas. A more sophisticated approach would require the computation of brain regions and representative fibers which are averaged across all subjects. The latter is described by O’Donnell et al. [129].

The computation of a representative fiber for each fiber bundle is carried out similarly that approach [129], also. If all fibers in the bundle take a very similar course, the fiber with the highest fiber density is chosen as a representative. If not, a clustering step is carried out in order to group fibers with a similar course. Then, an individual representative is computed per cluster as described above. For the grouping, we employ a spectral clustering approach leading to a spectral embedding of all fibers on which finally a standard k-means clustering is performed [128].

Since each individual fiber was divided into 100 segments of equal length for the derivation of associated parameters such as fractional anisotropy, we also divide each representative fiber into 100 segments. The color value of each segment may then be modified individually. For mapping a statistical parameter to fiber segments, we first decide in favor of a color scale and then, map each parameter value to its segment and a RGBA value (Fig. 5b). Then, we modify the saturation of the assigned color with respect to the corresponding DOI value, for example a high value results in a high saturation (recall Sec.4 for a description of DOI values). The fibers are visualized by means of illuminated streamlines which are extended with halos to improve spatial perception. Instead of representing each fiber segment by a tube, view-aligned quads are employed in a GPU-based implementation. This guarantees a high-quality rendering at interactive frame rates even when the user drills down to subject specific data and wants to display all individual fibers instead of a few fiber bundle representatives (Fig. 5a). Gasteiger et al. [50] successfully used this approach for visualizing streamlines in the exploration of blood flow in cerebral aneurysms.

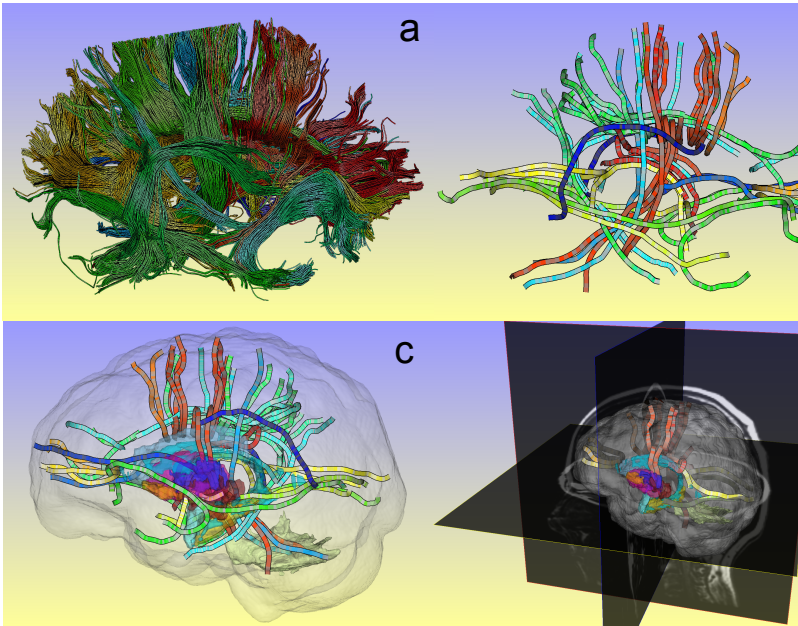


Figure 5: (a) The white matter fiber tracts of the subject used as model. (b) The bundles representatives, computed from each bundle. (c) Bundles in combination with the segmented brain regions and the brain outer surface. (d) Cross sectional images to augment the rendering.

Besides the statistical information related to the fiber tracks, measures of the segmented brain regions are available from the study. The segmentations were obtained by using the software Freesurfer (<http://surfer.nmr.mgh.harvard.edu/>) and the therein contained brain atlases. For displaying the measures, the surface geometry must be constructed based on the segmentation results. The standard Marching Cubes algorithm is employed for generating an isosurface per segmented region. Each surface is either assigned a uniform color according to Freesurfer's look-up color table or a color scale is defined and the value of a selected measure is mapped through this scale to surface color (Fig. 5c). The transparency of the surface is modified with respect to the DOI value which is associated to the brain region, for example a low DOI results in a highly transparent surface. We augment the visualization of fibers and brain regions by superimposing the outer surface of the brain as a highly transparent surface. Furthermore, orthogonal, adjustable image planes can be added that show slice renderings through the original volume data (Fig. 5d). Both approaches simplify the spatial orientation and serve as a context rendering.

C.6 Case Study

To exemplify the potential of our model/method, we show how to use our prototype to explore and analyze the data as described above. In particular, we investigate which fiber bundles show a decline in fractional anisotropy with age, and which do not. In the next phase, we then look for evidences of known hypotheses of age related white matter changes in the sample under investigation. We start the explorative investigation of the relation between anisotropy decline and age, by looking at the correlation coefficient of each fiber bundle's fractional anisotropy with age, as well as the regression coefficient. The system estimates these statistics for the chosen measure by iterating over a user specified dimension, in our case *fiberbundle*. These estimates are presented in two bar charts shown in Fig. 6. It is easy to spot one fiber (fornix) that goes against the general declining trend, also showing a bad fitting (sum of squared residual, SSE). We decide to show this fiber in a scatterplot (Fig. 6, top right) and detect several zero values, probably due to missing data, so the information for this fiber should be discarded or the missing data should be removed. Therefore we perform a brush on the scatterplot, to exclude the incorrect values, and this leads to opposite results (Fig. 6, bottom right), in line with the overall declining trend (these results are sketched with a dashed line in the bar chart of Fig. 6). We also notice that the corticospinal fiber tracts seem to be particularly insensitive to age decline, while other tracts have very strong decline (anterior callosal fibers and inferior longitudinal fasciculi). Finally, we notice two corresponding tracts, left and right occipitofrontal fasciculi, which are not homogeneous, with the right one showing a more

C.6. Case Study

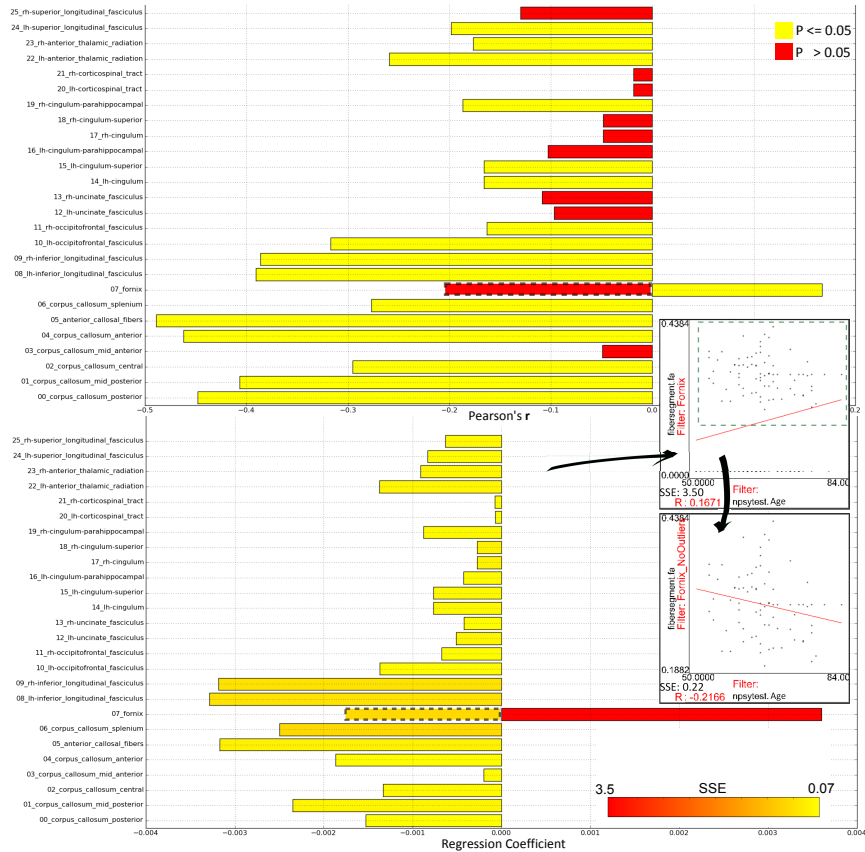


Figure 6: (top) Visualizing the correlation coefficient between age and fractional anisotropy of the fibers across all subjects,years. The FA measure is filtered by automatically iterating over a chosen dimension, in this case fiberbundle (thus iteratively slicing the measure). Therefore, each bar in the bar chart represents the correlation referred to a specific coordinate in the fiberbundle dimension. (bottom) The same type of visualization representing the regression coefficient instead. (right) Scatterplots related to the fornix, before and after excluding wrong values.

pronounced anisotropy decline, even though they are anatomically symmetrical.

In the second part of this case study, we attempt to confirm or reject three hypotheses (which were already statistically examined in previous work [172, 189]):

- The increased anisotropy decline in the anterior callosal fiber (CC-Anterior) with aging, as compared to the posterior portion of the corpus callosum, called splenium (CC-Splenium).

- The higher sensitivity of superior fibers (Superior-LF) to anisotropy decline, as compared to inferior fibers (Inferior-LF).
- The resistance of the cortico-spinal tract to anisotropy decline.

To do so, we begin with selecting the fibers under investigation. Then, we use these selections as filters in scatterplots opposing the age of the subjects and the fractional anisotropy (FA) of the fiber segments in their brains. In these scatterplots, shown in Fig. 7, each point represents a single subject examination (*subject, year*), while the other dimensions are aggregated for each of the measures. In the case of FA, this aggregation was filtered using the selections above. The system automatically computes the Pearson's r value of the two measures (one aggregated using the filter), the p -value, which, in our case, is below 0.05 except for the corticospinal tract (that, therefore, does not show a correlation that is statistically significant) and the regression line. The regression analysis also provides the regression coefficient and the sum of squared residuals (SSE) as a metric of the goodness of fit. These plots confirm that the spinal tract is relatively insensitive to the age effect. They also show that the posterior portion of the corpus callosum is less prone to age effect compared to the frontal portion. However, in contrast to our hypothesis, superior fibers were less prone to age effect than inferior fibers, which could mean that language function stays normal, but visual integration might decline.

C.7 Conclusion and Future Work

Medical cohort studies are an excellent starting point for exploratory data analysis, because most of the data acquisition is standardized before specific hypotheses are formulated. Often, such studies are designed to provide enough data, of very heterogeneous character, such that a large set of possible hypotheses can be tested on them. Accordingly, hypothesis generation becomes an own challenge, when associated with populations studies. In this work, we have demonstrated that an exploratory interface, which is capable of flexibly linking up different aspects of the data even if they are not given with respect to the exactly same domain, can help to swiftly identify new and possibly promising research hypotheses. We also showed, that the same approach is also capable of enabling a first quick analysis of the identified hypotheses, leading to an accelerated analysis methodology with respect to such highly rich and versatile data. This project is, however, very broad, and the prototype system presented here is still relatively limited in the spectrum of functionalities offered.

As future work we plan to import genotype data for the subjects, that at the time being was not readily available, and to integrate 2D/3D graph views for representing the brain connectivity information. We are also trying to obtain a more thorough evaluation of the system in terms of required

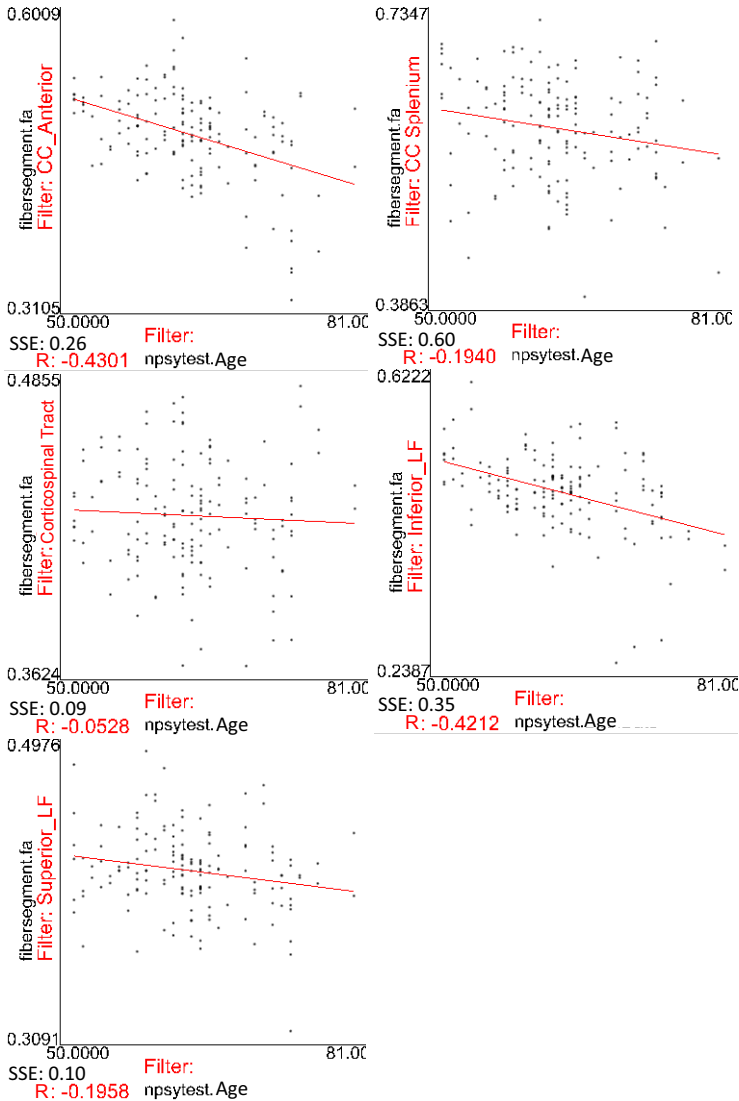


Figure 7: Age opposed to Fractional Anisotropy (FA) for each examination (subject, year). In each scatterplot, the FA value has been aggregated (across segments and bundles) using a different filter, as labeled in the views. Top left and middle right show a stronger negative correlation of the FA plotted against age, while top right and bottom left show a weaker negative correlation. Middle left shows almost no correlation of FA change with age for the corticospinal fiber tracts, which confirms previously published studies, and can be used as control. In each plot: R is the correlation coefficient, SSE is the sum of squared residuals of the regression analysis.

functionalities, in particular from a statistical and data-mining perspective. Finally, we plan to add functionalities to retrieve and visualize patient specific image data, in order to assess whether outliers originates from the image data, or whether they are the result of an erroneous derivation process.

Acknowledgements

We wish to thank Rocco Gasteiger for having provided us with the illuminated streamline renderer used to visualize the fiber tracts. Furthermore we wish to thank Stefan Bruckner for developing the VolumeShop framework, used to create the prototype showed in the paper. The cohort study used in this work was financially supported by the Research Council of Norway, University of Bergen, MedViz, and Western Norway Health Authority (grant #911593 to A.L., and grant #911397 to A.J.L.). This work was also supported by the MedViz network in Bergen, Norway (PK1760-5897-Project 11).

Guided Visualization of Ultrasound Image Sequences

Paolo Angelelli¹, Ivan Viola¹, Kim Nylund²,
Odd Helge Gilja^{2,3}, Helwig Hauser¹

¹Department of Informatics, University of Bergen, Norway

²Institute of Medicine, University of Bergen, Norway

³National Centre for Gastroenterologic Ultrasonography, Haukeland University Hospital, Bergen, Norway

Abstract

Ultrasonography allows informative and expressive real time examinations of patients. Findings are usually reported as printouts, screen shots and video sequences. However, in certain scenarios, the amount of imaged ultrasound data is considerable or it is challenging to detect the anatomical features of interest. Post-examination access to the information present in the data is, therefore, cumbersome. The examiner must, in fact, review entire video sequences or risk to lose relevant information by reducing the examination to single screen shot and printouts. In this paper we propose a novel post-processing pipeline for guided visual exploration of ultrasound video sequences, to allow easier and richer exploration and analysis of the data. We demonstrate the usefulness of this approach by applying it to a liver examination case, showing easier and quicker ultrasound image selection and data exploration.

This article was published in the *Proceedings of the Eurographics Workshop on Visual Computing for Biomedicine*, 2010:125–132

D.1 Introduction

Ultrasonography (US) is a powerful and inexpensive imaging modality appreciated by many physicians. It causes little to no patient discomfort and is non invasive, providing high safety with neither contraindications nor radiation exposure. Ultrasonography has also good spatial resolution, combined with very high temporal resolution. This makes it an invaluable tool for examinations, where both anatomic and dynamic information is of interest. In the clinical practice it is successfully used for examination, diagnosis and intra-operative guidance.

However, US also suffers from certain limitations when it comes to interpretation and retrieval of image information. US waves are heavily attenuated by air and bones, and fatty tissue causes artifacts in the images. Furthermore, the acquisition process is dependent on the examiner, as the image acquisition is done by free hand and the interpretation is done in real time. US has also drawbacks regarding the data storage and reviewing modalities: the typical ultrasonographic examination work flow, in fact, consists of live diagnosis during the examination. When there is the need to communicate the examination further, the acquired data can be saved for later reviewing. Data exported by 2D US scanners consists of annotated, and often printed, still images, and video sequences containing all the acquired US images, captured during the examinations at a certain frame rate. During certain kinds of US examinations, the physician scans several different anatomical structures, without focusing exclusively on one part of the anatomy. In such situations, as, for example, during abdominal examinations, simple snapshots of US slices may lack contextual information. They may also miss some important information that the examiner may have scanned, but not recognized and thus stored, in the first place. Stored video sequences contain all the imaged data, and, to a certain extent, prevent the loss of important information about structures of interest or their context. Unfortunately, such video data lacks higher semantic information, present during the live examination, such as the 3D position and orientation of the US planes, knowledge of which anatomical structures are imaged, neighboring anatomical structures, scanning direction, and so on. Therefore it can be challenging and time-consuming to review ultrasonographic sequences *after* the examination, especially if the review is performed by another physician, without first hand knowledge of the examination. Considerable efforts are required to mentally reconstruct the spatial position and orientation of the US images, and sometimes to understand which anatomical structures the displayed images refer to. Moreover, videos of US data, lacking semantic annotations such as the imaged anatomical structures, require the examiner to go through all the video sequences, during the reviewing process, to find the images with the structures of interest, taking (potentially) long time.

To solve these limitations, in this paper we present a pipelined approach that enriches the US data with semantic information. By using the added semantics, we want to guide the examiner during the data exploration and reviewing tasks. The key concept of the presented solution is to compute the *degree of interest* (DOI) for each US image with respect to which anatomical structures the examiner wants to see. We do this by considering a so called *DOI volume*, that describes how much each voxel belongs to the structure(s) of interest. In the following step we combine this user defined annotation of the space with the US images. This way we derive an aggregated measure of the DOI for each image in the US sequences. This measure is a semantic information that represents how much of the selected anatomical regions is present, or visible, in the US images, and can therefore be seen as a measure of the *importance* of the US images. It is used through proposed visualization methods to guide the examiner to the relevant images or video subsequences.

A possible use-case of our technique is when a physician wants to review previously acquired US scans of, for example, gastrointestinal examinations of a patient, and focus on regions that look suspicious. Normally, she would have to browse through each video sequence, trying to understand the position and orientation of each image with respect to the anatomy of the patient. Then she would identify the region of interest in each image of the sequences. Using our approach, the same physician could select the desired suspicious regions, specified in one of the proposed ways. The system computes a DOI profile, showing the DOI of each of the images for all the US scans she wants to review. Using this additional semantics, the system helps the physician to find quickly the images showing the desired anatomical regions in the videos. It can also superimpose the corresponding regions over the US images to allow for easier and quicker identification of the interesting anatomical regions. Our technique could also be useful for physicians who need to communicate examinations results to other doctors: video sequences together with relative regions of interest contain much more information as compared to single screen shots. Using our method, these videos are much easier to analyze by a physician without first hand knowledge of the examination.

Our implementation of the proposed technique has, at the moment, two pre-examination requirements. First, a volumetric dataset of the patient, such as MRI scan. This is used as anatomical context, as reference coordinate frame and as basis for the definition of DOI volumes along the anatomical regions of interest. Second, even if, in this work, we make the assumption that the multi-modal data are already spatially co-register, for the registration method adopted in our prototype the US videos must be recorded with US plane positioning information, acquired via any suitable tracking device. This provides registration of all the frames in the videos with the DOI volumes by just having to register one frame [20, 187].

Our pipeline is, in principle, also applicable without a volumetric dataset of the patient: it could be possible to specify the DOI information based solely on the tracked US data, as explained in Section D.3.1. The presented technique is, however, useful even in presence of a pre-acquired volumetric scan of the patient: ultrasonography allows to re-examine patients in an effective, fast and inexpensive way, without having to let the patient undergo other complex, expensive, and potentially harmful examinations such as CT or MRI.

The paper is structured as follows: in the next section we discuss the related works regarding multimodal visualization focused on US with special attention on guidance, focus+context and importance driven visualization. In Section 3 we present the details of each stage of the pipeline. In Section 4 we present the results of this technique applied to a case of liver examination, showing the benefits achieved through our guided visualization system. We conclude discussing the presented work in Section 5.

D.2 Related work

Our work aims at improving the diagnosis and treatment planning, which is one of the main challenges in medical visualization research. The challenge is to enable a clear understanding of the medical conditions depicted, and to guide the US examiner to the most relevant information during the reviewing process. Previous research related to advanced US data visualization has been mainly focused on the development of techniques for noise-free image rendering, especially in the case of three-dimensional visualization. The direct volume rendering of 3D US data requires a filtering stage to improve the image quality [161]. More recent approaches use probability metrics to evaluate a presence of an interface between tissues [67]. Furthermore, redundant information from 3D US measurements, resulting from volume overlap of consecutive scans, can be exploited to improve the rendering by preserving the temporal coherence [139].

2D US data rendering has been previously combined with augmented reality hardware to blend US with the real environment. US images have been displayed in the context of the body of the patient to show where they intersect the body [8]. Currently, registration techniques are usually based on internal landmarks and external markers, visible in the US data and in the pre-interventional 3D acquisition modality. In clinical practice non-rigid registration techniques are occasionally used [100, 123]. US images have been fused with MRI for neurosurgical interventions [124, 151]. Most of the commercially available techniques, such as fused visualization of PET-CT through image overlays, or linked CT-US slicing, or fused visualization of CT and US operate primarily on the data level [167]. Very recently, GE added a point tracking feature in their last generation of Logiq

scanners (Logic E9), to aid the physician during the examination to find previously analysed areas.

To provide better 3D orientation, an integration of a 3D CT visualization with 2D interventional US has been recently proposed for CT-US guided intervention incorporating cutaway views [20], or superimposed information on imaged liver segments on US images [187]. These works originate from importance-driven visualization techniques, which use data segmentation and relevance information to automatically generate expressive visualizations [185]. Approaches to visually emphasize features in volume renderings have also been discussed in different contexts. In the visualization of volumetric scalar data, two-level volume rendering uses segmentation information to render objects in the data with different composition and rendering techniques [62]. In the visualization of 3D flow data, a user-specified DOI function affecting optical properties is shown to visualize important flow features [61]. A more comprehensive overview about focus+context visualization is given by Hauser [59].

Our work is also related to the context of video visualization as we deal with video sequences. Chen et al. [23] propose a technique to extract features from video sequences. 2D US videos have also been automatically classified using a machine learning approach [134]. With respect to the visualization of time-varying data, interesting approaches to visualize the changes in time are also available [74, 196].

D.3 Guided Ultrasound Visualization

D.3.1 DOI Volume Specification

The first stage of the pipeline, illustrated in Figure 1, consists of the acquisition of the DOI volumes. These volumes represent the anatomical regions that the examiner is interested to see in the US data, and are used as a guidance instrument in the following stages. The value of a voxel in a DOI volume represents to which degree the respective anatomical location is relevant, or interesting, to the examiner. Special attention is required not only for the placement of the boundaries of the region of interest, but also for their definition. Hard boundaries are characterized by a steep transition to the region of interest from the surrounding volume. DOI values change immediately from 0 to 1 when entering a region of interest with hard boundaries and thus defines precisely the region of interest. However, since there is no gradual transition, DOI volumes with hard boundaries cause the DOI profiles to be rougher. Moreover, hard boundaries amplify segmentation and registration errors present at the edge of segmented regions of interest. To attenuate this, we propose to allow for soft boundaries in the specification of DOI volumes [34], for example, by convolving the volume with a suitable smoothing kernel, such as an averag-

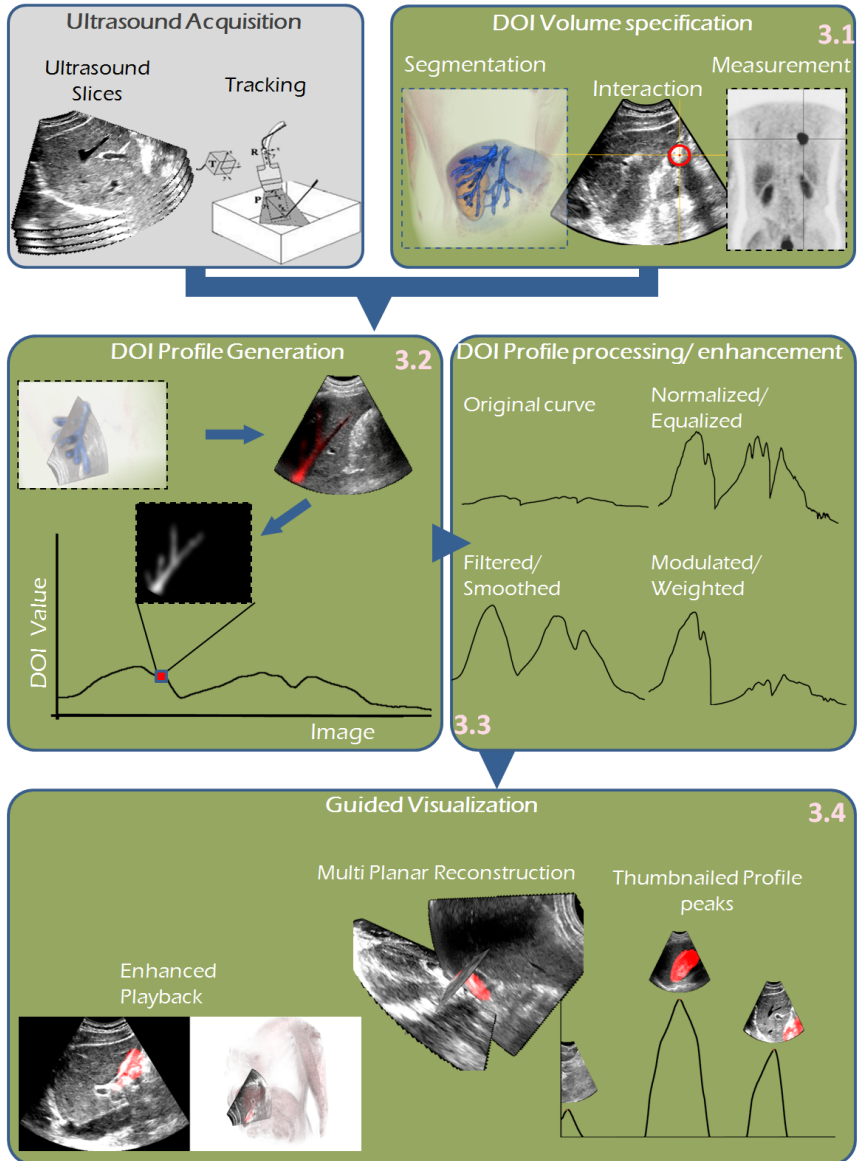


Figure 1: Schematic illustration of the proposed pipeline for guided visualization of US video sequences

ing or Gaussian 3D kernel. This way we attenuate small segmentation or registration errors by covering a slightly larger area with fading DOI values (Figure 3). By this, we also obtain a smoother transition of the DOI

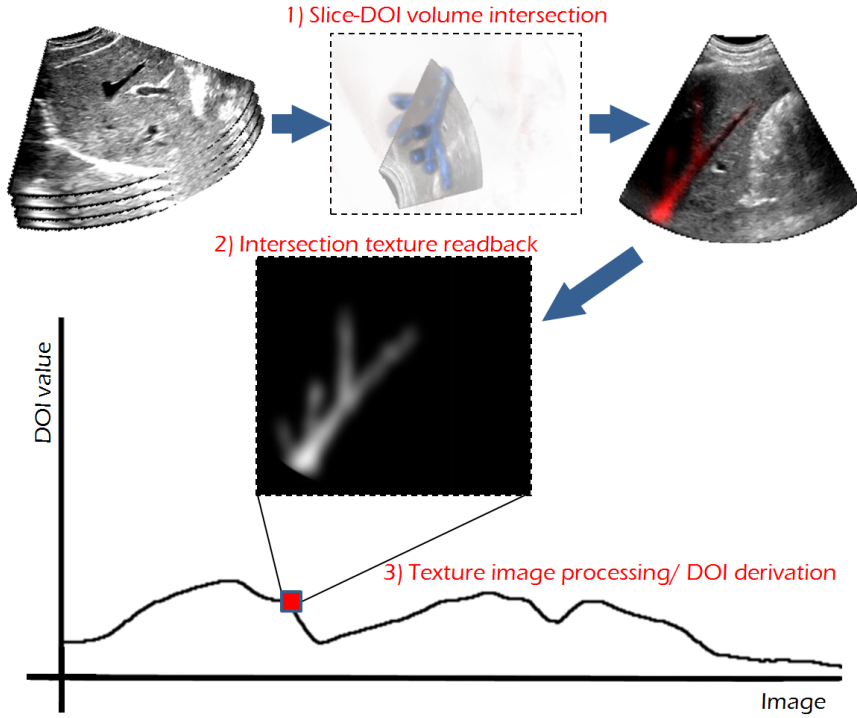


Figure 2: DOI profile generation through intersection between an US image plane and a DOI volume (segmented right hepatic vein tree), used as 3D texture. The result is a gray scale footprint of the DOI values in the 3D texture on the image plane. Summing each pixel of the intersection texture gives the DOI value for the US image

from one image to another. In case of DOI volumes with small interesting features, however, the smoothing operations should be carefully tuned to prevent information loss. A more formal definition of DOI volumes is then:

$$DOI(x, y, z) = \begin{cases} 1, & \text{structure in } (x, y, z) \text{ in focus.} \\ 0 < d < 1, & \text{structure in } (x, y, z) \text{ near focus.} \\ 0, & \text{structure in } (x, y, z) \text{ is context.} \end{cases} \quad (1)$$

DOI volumes are scalar volumes and they must be co-registered with the US to match the desired anatomical structure in the US data with the related DOI value. There are several methods to specify the regions of interest. The most intuitive one is by segmentation of a volumetric scan of the patient, such as a CT or MRI. For example, if a PET scan of the patient is available, high tracer uptakes in the PET scan can be used as a DOI

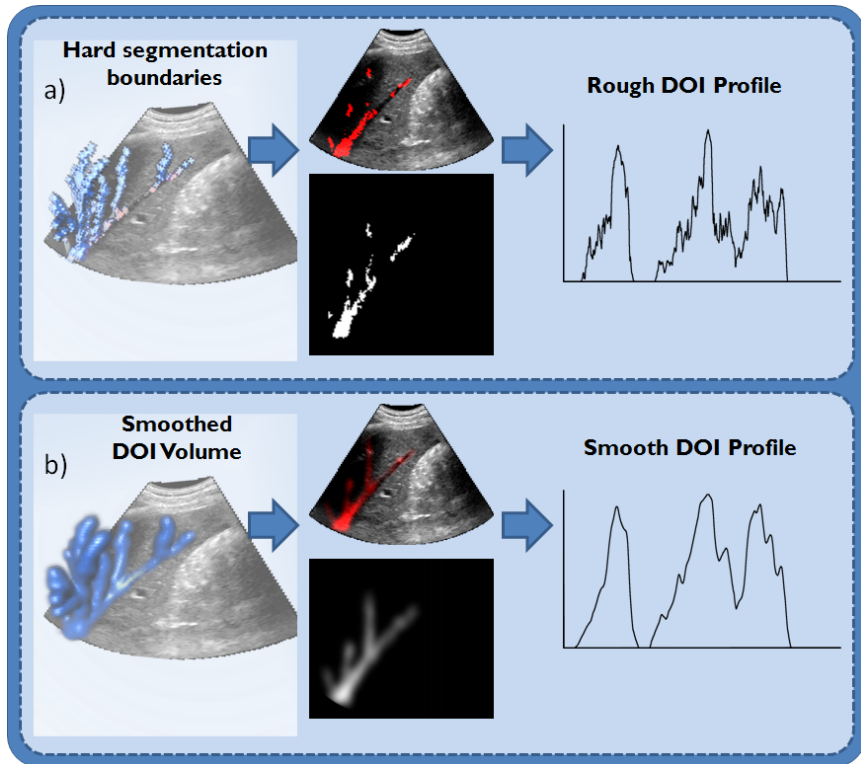


Figure 3: Original (a) and smoothed (b) DOI volume (segmented right hepatic vein tree). Small registration errors result attenuated and the DOI profile of the sequence results smoother

volume. Another possible method consists of using a transfer function to define structures of interest in a volume without the need of segmentation [20, 86, 150]. In this case, modifications to the transfer function are equivalent to selecting a new DOI volume. One more way to specify DOI volumes consists of selecting interesting regions in US images, which can then be transferred into 3D space using the registration information. This selection can be as simple as a point, used to position a simple sphere of parameterizable radius, or to start a limited region growing process, following the gradients either from the volumetric data, if available, or from the US data.

D.3.2 DOI Profile Generation

The second stage of the pipeline consists of the derivation of the DOI for the US images in the video sequences the examiner wants to review. With

the DOI of each image, we build a curve, or profile, of the relevance of each image in the video sequences, and we call it *DOI profile*. We compute the DOI of an US image with respect to a DOI volume as the amount of the volume intersected by the image. This is done by using the registration information for the image, coming from a (suitable) registration method, and calculating the image spatial coordinates with respect to the DOI volume. Details on the registration method we employed in our prototype system are given in Section D.4. We can now use the DOI volume as a 3D texture, and the image spatial coordinates as texture mapping for a rectangular polygon. The next step consists of texturing the polygon with the 3D DOI information from the DOI volume, and rendering it to a frame buffer object (FBO). The rendered image is a gray scale footprint of the values in the DOI volume on the polygon, representing the US image, as illustrated in Figure 2. Summing up the intensities of the pixels in the rendered image allows us to compute the aggregated DOI value of the US image. Storing the footprint enables us also to use it for visualization, as it highlights the interesting region in the US image. Keeping in mind that, by lowering the frequency of the US waves, the imaged area increases and vice-versa, a formal definition of the aggregated DOI, derived from the intersection footprint, is

$$DOI(image) = \frac{image\ area}{w \cdot h} \cdot \sum_{i=0}^{w \cdot h} pixel_i \quad (2)$$

The w and h parameters in Equation 2 represent the width and the height resolution of the intersection image. The $pixel_i$ parameter represents each pixel of the intersection image, while $image\ area$ is the physical area of the region in the US image. The DOI profile generated in this stage of the pipeline should be easy to modulate and use, and therefore needs to be normalized, or equalized, to be fitted into a $[0,1]$ range. These operations are going to be performed in the next stage of the pipeline.

D.3.3 DOI Profile Processing / Enhancement

The third stage of the pipeline is dedicated to processing and enhancement operations on DOI profiles to enhance the usability of the profiles. As previously outlined, raw DOI profiles do not have any common value range, and the values can be very small if the region of interest is small. Therefore, the first step consist of bringing the values into the unit range. We propose two possible techniques: normalization and histogram equalization of the profiles [70]. Both map the values onto the unit range, but normalization retains the proportions between values, while equalization evenly distributes the profile values in the value range. Equalization will enhance local variations of the DOI intensity instead of global variations,

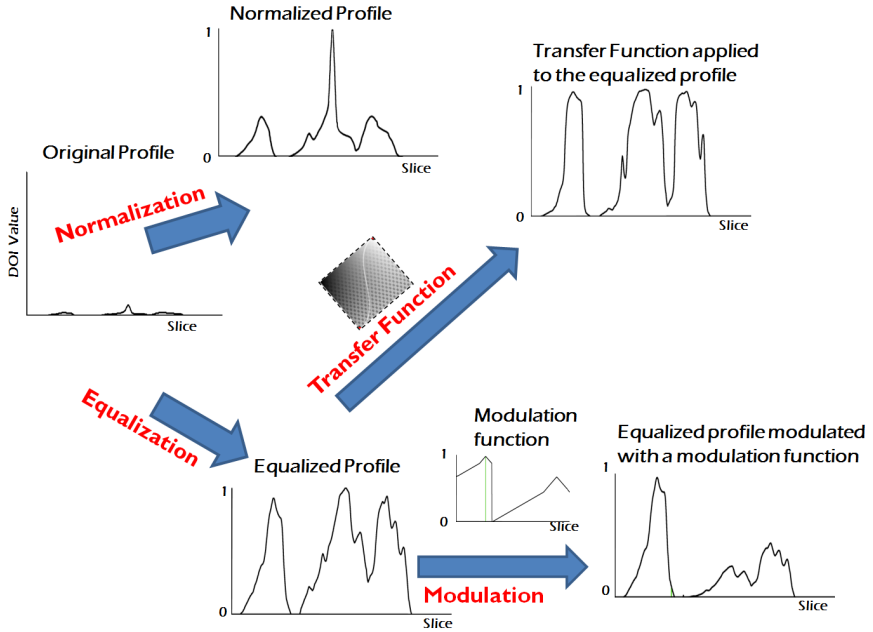


Figure 4: DOI Profile processing / enhancement operations

and it is useful when a small number of images have very different values compared to the others.

Once the profiles have been mapped into the unit range, they are ready for further processing, to improve the derivation of useful information for the visualization. The first operation we propose is temporal filtering of the DOI profiles. A filter kernel can be used for temporal smoothing, when the profile is too rough. This helps in the profile visualization, as it shows better the trends in the data. We then adopt a peak detection algorithm [12, 127], that identifies cluster peaks on the DOI profiles in a waterfall-alike way, and thus finds a representative image for each cluster. To achieve good results, such algorithms are usually also applied on a relatively smooth curve, otherwise they lead to too many peaks along the profile.

The last operation we propose to process the profiles is profile modulation. This type of operation multiplies an input profile with one or more other profiles, to modulate the input profile values. If p_{DOI} is the DOI profile and p_m is the modulation profile, a formal description of profile modulation is then

$$p'_{DOI}(x) = p_{DOI}(x) \cdot p_m(x) \quad (3)$$

Profile modulation is very useful as it can combine information from different profiles, and we use this operation to weight the DOI profile with a similarity profile of the scans. The reason for this is that the desired structures of interest may be poorly imaged or visualized from specific points of view, even when the image plane intersects well the structure of interest. So the image with the highest DOI value might not show the structures of interest in an optimal way. This can happen under certain circumstances like with air, or bones, attenuating the US waves. But the structures may become visible with a similar image plane position, or under different patient conditions. For this reason we want to provide the examiner with a similarity weighted DOI profile, different for each image in the videos, so that similar and important images can be found quickly. To provide this functionality, we needed a metric to define the similarity between two US images. We have chosen to use distance and orientation: closer images have closer image centers, while a small angle between image normals means similar orientation of images in space. So we compute the similarity between a selected image and another image by multiplying the distance between image centers with the angle between image normals. This way the system can build a similarity profile for a selected image, and use it to modulate the DOI profile (see Figure 4). Such augmentation is especially useful when there are many sequences to review and they are acquired with different transducers or under different examination setups or patient conditions. We also use DOI profile modulation with a profile of angles between image normals in the automatic generation of a multi planar reconstruction, as explained in the next section.

D.3.4 Guided Visualization

The first visualization technique we create using the DOI information is a plot of the DOI profile. In the plot we also highlight the position of the currently visualized US image (see Figure 7(d)). This becomes a navigation tool for the examiner during the data exploration process. We also apply a peak detection algorithm to the profile, as previously discussed. This enables us to find representatives for clusters of neighboring images. We use the peaks to place a selectable US image thumbnail on the corresponding profile location. The thumbnails work both as a high level overview of the data and as a bookmark for quick data browsing. The second technique we propose to enhance the exploration and playback of US images consists of using the intersection images already utilized in the DOI computation (Section D.3.2), as an on-demand, semi-transparent layer to superimpose over the US images. This visualization highlights to the examiner the relevant regions in the image. We also integrate the classic 2D US image visualization, familiar to the examiner, in a linked 3D view where the image is rendered together with the DOI volume or a volumetric scan of

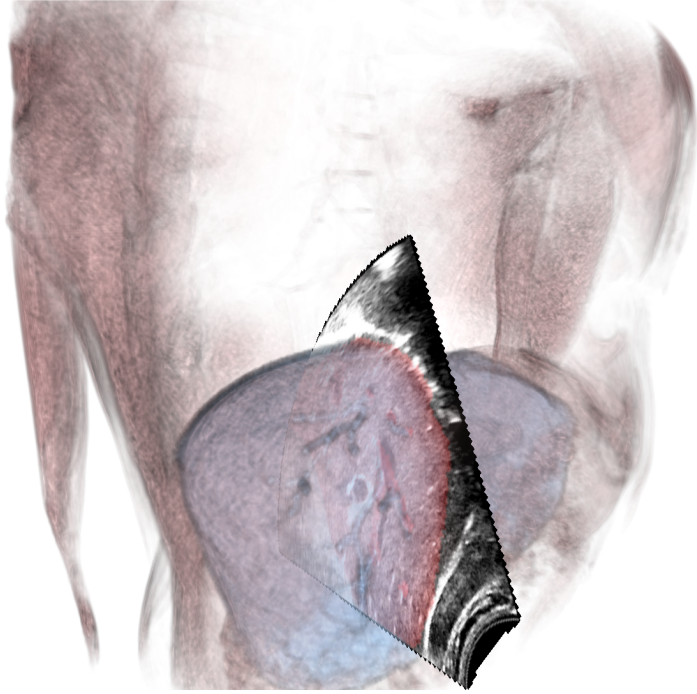


Figure 5: Image of a US image co-registered with the MRI volume

the patient. We do this by rendering a proxy geometry, textured with the US image, correctly positioned into a volume rendering of the volumetric data (Figure 5). This helps the examiner to better understand the position and orientation of the displayed US image.

Multi-Planar Reconstruction from 2D US Data

The last visualization technique proposed here is an automatic multi-planar reconstruction (MPR) of the anatomy with intersecting 2D US images. It provides a “ $2\frac{1}{2}D$ ” visualization of the region of interest using the 2D US data (Figure 6). In the US domain such visualization is possible nowadays only with 3D US volume data, or has to be generated manually [80]. To create such an MPR visualization, we again employ a proxy geometry for each US image in the reconstruction, texture it with the image and then render each geometry in 3D space. For this technique we have also developed an algorithm to automatically compute a suitable selection of intersecting images showing the region of interest. It consists of a recursive modulation of the DOI profile of the US data with the angle between the images in order to favor images that are as normal to each other as possible. The

algorithm works as follows: It takes the current DOI profile and selects the image with the highest DOI value. Then it calculates a modulation profile with $(1 - \cos(\text{angle}))$ of the angles between the selected image and all the others, to have a measure of the orthogonality of the all the images against the selected image. Finally, it modulates the current DOI profile with the computed modulation profile, and iterates. The second selected image will therefore be the image that conjugates best DOI value with orthogonality with the previously selected image. The third image will conjugate DOI value with orthogonality with the first and the second images. This algorithm is fast, taking only the normal of the US planes into consideration. However we also provide a manual tuning option to allow complete data exploration capability.

D.4 Results

To demonstrate the usefulness of the presented approach, and to obtain a first evaluation from the medical side, we built a prototype system and exemplified its capabilities in a proof-of-concept case study consisting of a trans-abdominal US examination with the focus on the liver. A 31 year old healthy male volunteer was examined after having first undergone an MRI scan of the abdomen. Several trans-abdominal US examinations were performed at different times. The US data (total of 7 scans) were obtained using different 2D transducers, in combination with a commercially available magnetometer-based tracking device (Flock of Birds, Ascension Technology) for image tracking during freehand US acquisitions. In our prototype system we have decided to adopt a landmark based rigid registration technique, well suited if tracking information is going to be employed. Our registration approach consist of identifying anatomical features visible in both the modalities, and indicating these through the placement of landmarks in the data directly on screen. These two sets of points are then used to compute a rigid transformation matrix from one dataset to the other [187]. This matrix is then combined with the transformations recorded with the tracking system, to compute a suitable transformation for each US image in the video sequences. The presented visualization pipeline is, however, independent of the employed registration technique, as long as it can provide registration of each image in the video sequences to the DOI volumes. More advanced registration techniques are nowadays available. However, we found that the employed registration method is quickly applicable to our type of data, a goal of the proposed technique, and provides sufficiently good results. Abdominal examination scans do not contain highly moving anatomy, and the deformation of the organs caused by the pressure of the probe proved to be minimal, so this method was able to register the two modalities sufficiently well. In case of changing the patient position, the physician simply started a new video

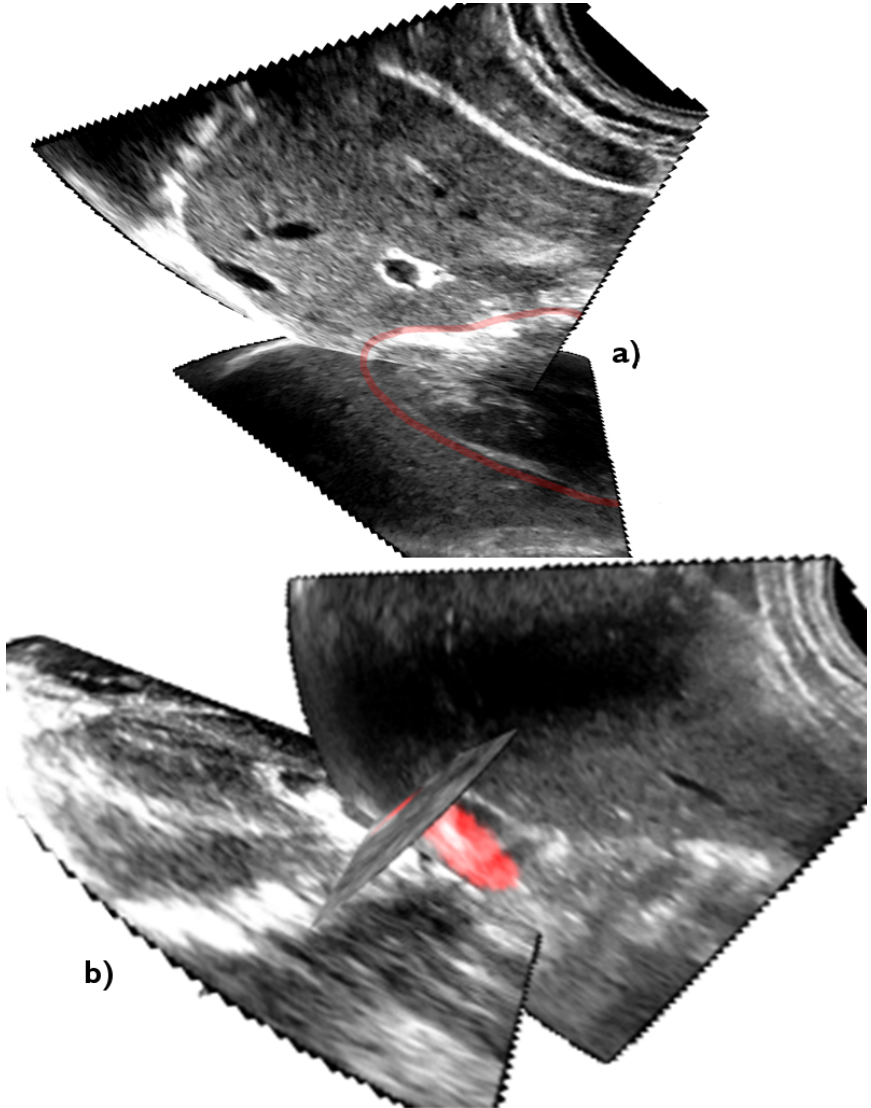


Figure 6: Multi planar reconstruction of the region of interest using 2D US images. a) MPR of the right kidney b) MPR of the right hepatic vein c) comparison image showing how MPR is currently applied to volume data

sequence. The US data uptakes were stored in AVI format, then imported into our system. The MRI scan was acquired at a resolution of $256^2 \times 176$. Figure 5 shows both the modalities co-registered, with the intersection between the whole liver parenchyma and the US image highlighted in red.

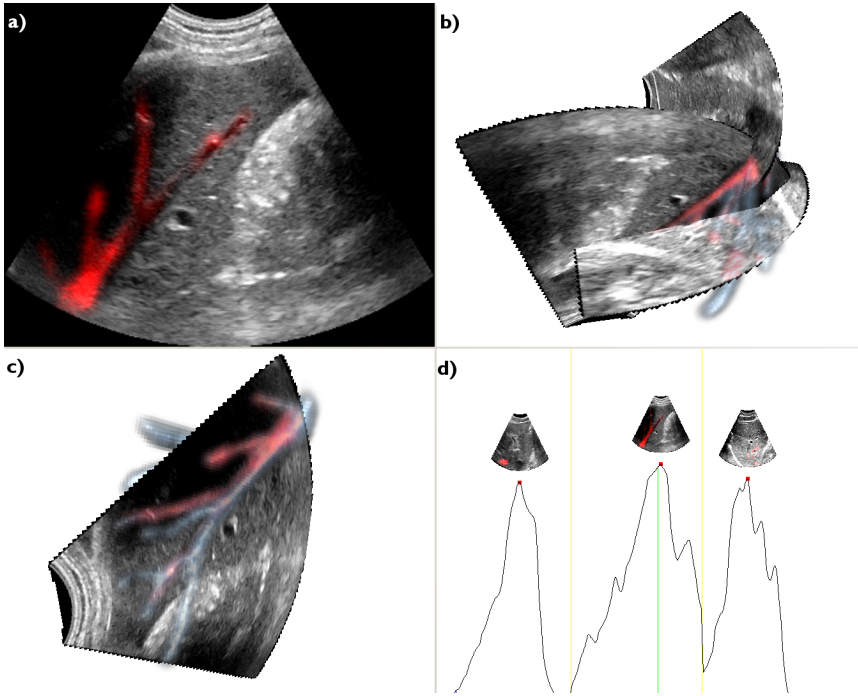


Figure 7: Screen shot of the system showing linked views of a US image, (a) with the intersection image superimposed, (b) forming a MPR with images crossing the DOI volume, (c) positioned in DVR of the MRI data to provide spatial orientation and context, (d) highlighted in the thumbnailled DOI profile (in green). The used DOI volume is the segmented and smoothed right hepatic vein tree. The yellow lines in the profile view (d) represent sequence boundaries. Here, three US sequences have been joined.

We have specified several DOI volumes, all of them through segmentation of the MRI scan. For the segmentation we used the ITK-SNAP tool. The DOI volumes we used define the liver parenchyma, the right kidney, the gallbladder, the right hepatic vein tree and the middle hepatic vein tree. With respect to the performances, processing a video sequence of ca. 3000 frames against a DOI volume requires around 5 seconds of computation, with our CPU based implementation, on an Intel Xeon 2.5GHz workstation. Figure 7 shows an examples of three US video sequences joined together, enriched with DOI information and visualized with our system. The development of the proposed pipeline into a prototype system benefited from our tight cooperation between technological and medical expertise. In the beginning we started with a broader range of possible visualization techniques, and some of them did not prove to be promising, as, for instance, modulation of the playback speed according to the DOI

values. The multi-planar reconstruction made out of 2D US images is a visualization which attracted particular interest, since it was not realized out of 2D data and from different sequences before, and it eventually turned out to be a useful visualization to inspect the data. The DOI profile was a handy tool for an active and quicker inspection of the US videos. The multimodal visualization of US images combined with DVR of the volumetric scan was useful for enabling a quicker understanding of the orientation of the images. The DOI region overlay was accepted as an interesting and useful method for examination training. After the demonstration of the test examinations with our system, it was acknowledged (on behalf of the medical side) that it combines assisted navigation and useful visualization techniques of US data in a novel way. It offers real time enhanced video playback and interaction for image selection and visualization customization, and changing the DOI volume takes also just a few seconds. The tool has been seen also especially interesting for doctor-to-doctor communication, as it enriches plain video streams with semantic information and allows to communicate the findings without leaving out part of the original data. Our system also potentially enables to find suspicious regions during the review, which was missed by the examiner during the live examination.

D.5 Summary and Conclusions

In this paper we have presented a pipelined approach for guided visualization during the review of US examinations. We have introduced the concept of *degree-of-interest* volumes in the context of US data visualization, to annotate the data with semantic information. We have presented a suite of visualization techniques that use the added semantic information to provide guidance and insight during the reviewing process, and aiming at improving the diagnosis and treatment planning process. We have implemented the proposed solution in a prototype system, and used it to review a case of a trans-abdominal US examination, achieving positive and useful feedbacks from our medical partners.

During the development of the prototype we tightly cooperated with our medical partners and addressed their needs. The presented prototype has been seen as possibly useful tool for post examination data exploration, to communicate examination results to other doctors, and for examination training. To the best of our knowledge, no mechanism has been previously presented to aid the examiner to focus on particular structures while reviewing 2D US examinations. Our approach extends the current ultrasonographic examination work flow during the live acquisition, since the data must be acquired with tracking, unless registration for the US data can be obtained by other means. We then add post processing steps currently non-existent in ultrasonographic work flow to enrich the data with

semantic information and thereby enable advanced data exploration. The presented method is also meant for examinations of anatomy that does not move particularly, or deform easily. When applied to cardiac data, for example, the high dynamic behavior of the imaged anatomy would represent a problem for the registration of the data to the DOI volumes. In such scenarios, alternative or additional solutions for the registration are needed.

Acknowledgements

This work has been supported by the IllustraSound research project, funded by the VERDIKT program of the Norwegian Research Council (Nr. 193170), and by the MedViz Initiative (medviz.uib.no, PK1760 Project 11). Furthermore, we are grateful to Stefan Bruckner for providing the VolumeShop visualization framework, and Timo Ropinski, for fruitful discussions enabled via the NRC's researcher exchange program DAADppp (Nr. 194673). A special mention goes to Yngve Devik Hammersland, for integrating the support for magnetic tracking devices into VolumeShop.

Bibliography

- [1] M. D. Abramoff, P. J. Magelhaes, and S. J. Ram. Image processing with imagej. *Biophotonics International*, 11(7):36–42, 2004.
- [2] P. Acton, L. Pilowsky, H. Kung, and P. Ell. Automatic segmentation of dynamic neuroreceptor single-photon emission tomography images using fuzzy clustering. *European Journal of Nuclear Medicine*, 26(6):581–590, 1999.
- [3] L. Agati, G. Tonti, G. Pedrizzetti, F. Magri, S. Funaro, M. Madonna, F. Celani, T. Messenger, and A. Broillet. Clinical application of quantitative analysis in real-time MCE. *European Journal of Echocardiography*, 5(suppl 2):17–23, 2004.
- [4] W. Anderson, G. Preston, and C. Silva. Using python for signal processing and visualization. *Computing in Science & Engineering*, 12(4):90–95, 2010.
- [5] I. Arganda-Carreras, C. O. S. Sorzano, R. Marabini, J. M. Carazo, C. O. de Solorzano, and J. Kybic. Consistent and elastic registration of histological sections using vector-spline regularization. In *Computer Vision Approaches to Medical Image Analysis*, volume 4241 of *Lecture Notes in Computer Science*, pages 85–95. Springer Berlin / Heidelberg, May 2006.
- [6] S. P. Awate and R. T. Whitaker. Feature-Preserving MRI Denoising using a Nonparametric, Empirical-Bayes Approach. *IEEE Transactions on Medical Imaging*, 26(9):1242–1255, 2007.
- [7] N. Ayache, J. Boissel, S. Brunak, G. Clapworthy, G. Lonsdale, J. Fingberg, A. Frangi, G. Deco, P. Hunter, P. Nielsen, et al. Towards virtual physiological human: Multilevel modelling and simulation of the human anatomy and physiology. *Virtual Physiological Human: White paper, EC-DG INFSO and DG JRC*, 2006.
- [8] M. Bajura, H. Fuchs, and R. Ohbuchi. Merging virtual objects with the real world: Seeing ultrasound imagery within the patient. In *Proceedings of SIGGRAPH '92*, pages 203–210, 1992.
- [9] J. B. Bassingthwaight. Strategies for the physiome project. *Annals of Biomedical Engineering*, 28:1043–1058, 2000. 10.1114/1.1313771.
- [10] R. Becker and W. Cleveland. Brushing scatterplots. *Technometrics*, pages 127–142, 1987.
- [11] U. Behrens, J. Teubner, C. Everts, M. Walz, and H.-O. Peitgen. Computer-Assisted Dynamic Evaluation of Contrast-Enhanced MRI. In *Proceedings of CARS*, pages 362–367, 1996.
- [12] S. Beucher. Watershed, hierarchical segmentation and waterfall algorithm. In J. Serra and P. Soille, editors, *Mathematical morphology and its applications to image processing*, pages 69–76. Kluwer Academic Publishers, 1994.

-
- [13] Å. Birkeland and I. Viola. View-dependent peel-away visualization for volumetric data. In *Proceedings of the Spring Conference on Computer Graphics (SCCG 2009)*, pages 133–139, 2009.
- [14] J. Blaas, C. Botha, C. Majoie, A. Nederveen, F. Vos, and F. Post. Interactive visualization of fused fmri and dti for planning brain tumor resections. In *Proceedings of SPIE*, volume 6509, page 65091P, 2007.
- [15] J. Bock, A. Frydrychowicz, A. Stalder, T. Bley, H. Burkhardt, J. Hennig, and M. Markl. 4D phase contrast MRI at 3 T: Effect of standard and blood-pool contrast agents on SNR, PC-MRA, and blood flow visualization. *Magnetic Resonance in Medicine*, 63(2):330–338, 2010.
- [16] H. Bogren, M. Buonocore, et al. 4 d magnetic resonance velocity mapping of blood flow patterns in the aorta in young vs. elderly normal subjects. *Journal of Magnetic Resonance Imaging*, 10(5):861–869, 1999.
- [17] M. Borkin, K. Gajos, A. Peters, D. Mitsouras, S. Melchionna, F. Rybicki, C. Feldman, and H. Pfister. Evaluation of artery visualizations for heart disease diagnosis. *Visualization and Computer Graphics, IEEE Transactions on*, 17(12):2479–2488, 2011.
- [18] M. Borkin, S. Melchionna, C. Feldman, E. Kaxiras, and H. Pfister. Multidimensional visualization of hemodynamic data. Proceedings of IEEE Visualization Conference, Atlantic City, USA, October 2009.
- [19] S. Bruckner, V. Solteszova, M. Groller, J. Hladuvka, K. Buhler, J. Yu, and B. Dickson. Braingazer-visual queries for neurobiology research. *Visualization and Computer Graphics, IEEE Transactions on*, 15(6):1497–1504, 2009.
- [20] M. Burns, M. Haidacher, W. Wein, I. Viola, and E. Gröller. Feature emphasis and contextual cutaways for multimodal medical visualization. In *Proceedings of EuroVis '07*, pages 275–282, 2007.
- [21] M. Cerqueira, N. Weissman, V. Dilsizian, A. Jacobs, S. Kaul, W. Laskey, D. Pennell, J. Rumberger, T. Ryan, M. Verani, et al. Standardized myocardial segmentation and nomenclature for tomographic imaging of the heart a statement for healthcare professionals from the cardiac imaging committee of the council on clinical cardiology of the american heart association. *Circulation*, 105(4):539–542, 2002.
- [22] L. Chen, G. Herman, and R. Reynolds. Surface shading in the cuberille environment. *IEEE COMP. GRAPHICS APPLIC.*, 5(12):33–43, 1985.
- [23] M. Chen, R. Botchen, R. Hashim, D. Weiskopf, and T. Ertl. Visual signatures in video visualization. In *IEEE Transactions on Visualization and Computer Graphics*, volume 12, pages 1093–1100, oct 2006.
- [24] M. Chen, A. E. Kaufman, and R. Yagel. *Volume Graphics*. Springer, 2000.
- [25] M. Chen, D. Silver, A. Winter, V. Singh, and N. Cornea. Spatial transfer functions: a unified approach to specifying deformation in volume modeling and animation. In *Proceedings of the 2003 Eurographics/IEEE TVCG Workshop on Volume graphics*, pages 35–44. ACM, 2003.
- [26] W. Chen, M. L. Giger, and U. Bick. A Fuzzy C-Means (FCM)-Based Approach for Computerized Segmentation of Breast Lesions in Dynamic Contrast-Enhanced MR Images. *Academic Radiology*, 13(1):63–72, 2006.

- [27] N. Cornea, D. Silver, and P. Min. Curve-skeleton properties, applications, and algorithms. *Visualization and Computer Graphics, IEEE Transactions on*, 13(3):530–548, 2007.
- [28] C. Correa, D. Silver, and M. Chen. Discontinuous displacement mapping for volume graphics. In *Proceedings of Volume Graphics*, volume 6, pages 9–16, 2006.
- [29] E. Coto, S. Grimm, S. Bruckner, M. E. Gröller, A. Kanitsar, and O. Rodriguez. MammoExplorer: An Advanced CAD Application for Breast DCE-MRI. In *Proceedings of Vision, Modelling, and Visualization 2005*, pages 91–98, Nov. 2005.
- [30] A. Crippa and J. B. T. M. Roerdink. Data-driven visualization of functional brain regions from resting state fmri data. In P. Eisert, K. Polthier, and J. Hornegger, editors, *Proceedings Vision, Modeling and Visualization Workshop (VMV)*, 4–6 Oct, Berlin, 2011.
- [31] M. Descoteaux, E. Angelino, S. Fitzgibbons, and R. Deriche. Regularized, fast, and robust analytical q-ball imaging. *Magnetic Resonance in Medicine*, 58(3):497–510, 2007.
- [32] H. Doleisch. Simvis: Interactive visual analysis of large and time-dependent 3d simulation data. In *Simulation Conference, 2007 Winter*, pages 712–720, dec. 2007.
- [33] H. Doleisch. SIMVIS: interactive visual analysis of large and time-dependent 3D simulation data. In *Proceedings of the 39th conference on Winter simulation*, pages 712–720. IEEE Press, 2007.
- [34] H. Doleisch and H. Hauser. Smooth brushing for focus+context visualization of simulation data in 3D. *Journal of WSCG*, 10(1):147–154, 2002.
- [35] R. Drebin, L. Carpenter, and P. Hanrahan. Volume rendering. In *ACM Siggraph Computer Graphics*, volume 22, pages 65–74. ACM, 1988.
- [36] S. Durrleman, X. Pennec, A. Trounev, G. Gerig, and N. Ayache. Spatiotemporal atlas estimation for developmental delay detection in longitudinal datasets. *Medical Image Computing and Computer-Assisted Intervention–MICCAI 2009*, pages 297–304, 2009.
- [37] S. Eikeland. Multi-volume visualization and exploration. Master’s thesis, University of Bergen, 2010.
- [38] N. Elie, A. Kaliski, P. Pouponneau, P. Opolon, A. Roche, and N. Lassau. Methodology for Quantifying Interactions Between Perfusion Evaluated by DCE-US and Hypoxia Throughout Tumor Growth. *Ultrasound in Medicine & Biology*, 33(4):549–560, 2007.
- [39] M. Everts, H. Bekker, J. Roerdink, and T. Isenberg. Depth-dependent halos: Illustrative rendering of dense line data. *Visualization and Computer Graphics, IEEE Transactions on*, 15(6):1299–1306, 2009.
- [40] J. Fails, A. Karlson, L. Shahamat, and B. Shneiderman. A visual interface for multivariate temporal data: Finding patterns of events across multiple histories. In *Visual Analytics Science And Technology, 2006 IEEE Symposium On*, pages 167–174. Ieee, 2006.
- [41] Z. Fang, T. Möller, G. Hamarneh, and A. Celler. Visualization and exploration of time-varying medical image data sets. In *GI ’07: Proceedings of Graphics Interface 2007*, pages 281–288, New York, NY, USA, 2007. ACM.
- [42] D. D. Feng, editor. *Biomedical Information Technology*. Elsevier, October 2007.
- [43] J. Fenner, B. Brook, G. Clapworthy, P. Coveney, V. Feipel, H. Gregersen, D. Hose, P. Kohl, P. Lawford, K. McCormack, et al. The europhysiome, step and a roadmap for the virtual physiological human. *Philosophical Transactions of the Royal Society A: Mathematical, Physical and Engineering Sciences*, 366(1878):2979–2999, 2008.

- [44] F. Frenet. Sur les courbes a double courbure. *Journal des Mathematiques Pures et Appliquees*, 17:437–447, 1852.
- [45] O. Friman, A. Hennemuth, A. Harloff, J. Bock, M. Markl, and H. Peitgen. Probabilistic 4d blood flow mapping. *Medical Image Computing and Computer-Assisted Intervention—MICCAI 2010*, pages 416–423, 2010.
- [46] P. Frinking, L. Mercier, N. Rognin, M. Arditi, F. Tranquart, and M. Schneider. Real-time contrast-enhanced ultrasound parametric imaging in prostate. In *Proceedings of the 15th European Symposium On Ultrasound Contrast Imaging*, pages 40–49, Jan 2010.
- [47] A. Frydrychowicz, A. Stalder, M. Russe, J. Bock, S. Bauer, A. Harloff, A. Berger, M. Langer, J. Hennig, and M. Markl. Three-dimensional analysis of segmental wall shear stress in the aorta by flow-sensitive four-dimensional-MRI. *Journal of Magnetic Resonance Imaging*, 30(1):77–84, 2009.
- [48] R. Fuchs and H. Hauser. Visualization of Multi-Variate Scientific Data. 28(6):1670–1690, 2009.
- [49] K. K. Garfield, S. Joffe, and S. A. Okon. Hepatic adenoma. <http://emedicine.medscape.com/article/369104-overview>, feb 2009.
- [50] R. Gasteiger, M. Neugebauer, O. Beuing, and B. Preim. The FLOWLENS: A Focus-and-Context Visualization Approach for Exploration of Blood Flow in Cerebral Aneurysms. *IEEE Transactions on Visualization and Computer Graphics*, 17(12):2183–2192, 2011.
- [51] R. Gasteiger, M. Neugebauer, C. Kubisch, and B. Preim. Adapted surface visualization of cerebral aneurysms with embedded blood flow information. In *Eurographics Workshop on Visual Computing for Biology and Medicine (EG VCBM)*, pages 25–32. Citeseer, 2010.
- [52] S. Glagov, E. Weisenberg, C. Zarins, R. Stankunavicius, and G. Kolettis. Compensatory enlargement of human atherosclerotic coronary arteries. *New England Journal of Medicine*, 316(22):1371–1375, 1987.
- [53] S. Glaßer, S. Schäfer, S. Oeltze, U. Preim, K.-D. Toennies, and B. Preim. A Visual Analytics Approach to Diagnosis of Breast DCE-MRI Data. In *Proc. of Vision, Modeling, and Visualization (VMV)*, pages 351–362, Braunschweig, November 2009.
- [54] B. Gooch and A. Gooch. Non-photorealistic rendering. *AK peters, Ltd*, pages 2–3, 2001.
- [55] J. Greenleaf, J. Tu, and E. Wood. Computer generated three-dimensional oscilloscopic images and associated techniques for display and study of the spatial distribution of pulmonary blood flow. *Nuclear Science, IEEE Transactions on*, 17(3):353–359, 1970.
- [56] A. C. Guyton and J. E. Hall. *Textbook of Medical Physiology, 11th edition*. Elsevier Saunders, 2005.
- [57] M. Hadwiger, J. M. Kniss, C. Rezk-salama, D. Weiskopf, and K. Engel. *Real-time Volume Graphics*. A. K. Peters, Ltd., Natick, MA, USA, 2006.
- [58] V. Harinarayan, A. Rajaraman, and J. Ullman. Implementing data cubes efficiently. In *ACM SIGMOD Record*, volume 25, pages 205–216. ACM, 1996.
- [59] H. Hauser. Generalizing focus+context visualization. In *Scientific Visualization: The Visual Extraction of Knowledge from Data*, pages 305–327. Springer, 2005.

- [60] H. Hauser. Generalizing focus+ context visualization. *Scientific visualization: The visual extraction of knowledge from data*, pages 305–327, 2006.
- [61] H. Hauser and M. Mlejnek. Interactive volume visualization of complex flow semantics. In *Proceedings of VMV '03*, pages 191–198, 2003.
- [62] H. Hauser, L. Mroz, G. I. Bisch, and M. E. Gröller. Two-level volume rendering. *IEEE Transactions on Visualization and Computer Graphics*, 7(3):242–252, 2001.
- [63] E. A. Hauth, C. Stockamp, S. Maderwald, A. Mühler, R. Kimmig, H. Jaeger, J. Barkhausen, and M. Forsting. Evaluation of the three-time-point method for diagnosis of breast lesions in contrast-enhanced mr mammography. *Clinical Imaging*, 30(3):160 – 165, 2006.
- [64] G. Herman. Three-dimensional imaging on a ct or mr scanner. *Journal of computer assisted tomography*, 12(3):450, 1988.
- [65] G. Herman. A survey of 3d medical imaging technologies. *Engineering in Medicine and Biology Magazine, IEEE*, 9(4):15–17, 1990.
- [66] G. T. Herman and H. K. Liu. Three-dimensional display of human organs from computed tomograms. *Computer Graphics and Image Processing*, 9(1):1 – 21, 1979.
- [67] D. Hönigmann, J. Ruisz, and C. Haider. Adaptive design of a global opacity transfer function for direct volume rendering of ultrasound data. In *Proceedings of IEEE Visualization '03*, pages 489–496, 2003.
- [68] C. Huang-Wei, A. Bleuzen, M. Olar, D. Portalez, J. Roumy, H. Trillaud, and F. Tranquart. Role of parametric imaging in contrast-enhanced sonography of hepatic focal nodular hyperplasia. *Journal of Clinical Ultrasound*, 34(8):367–373, 2006.
- [69] P. Hunter, P. Robbins, and D. Noble. The iups human physiome project. *Pflügers Archiv European Journal of Physiology*, 445(1):1–9, 2002.
- [70] A. K. Jain. *Fundamentals of digital image processing*. Prentice Hall, 1989.
- [71] R. Janardhanan, J. C. Moon, D. J. Pennell, and R. Senior. Myocardial contrast echocardiography accurately reflects transmural myocardial necrosis and predicts contractile reserve after acute myocardial infarction. *American Heart Journal*, 149(2):355–362, 2005.
- [72] C. Johnson and S. Parker. Applications in computational medicine using scirun: A computational steering programming environment. *Supercomputer '95*, pages 2–19, 1995.
- [73] C. Jones and K. Ma. Visualizing Flow Trajectories Using Locality-based Rendering and Warped Curve Plots. *Visualization and Computer Graphics, IEEE Transactions on*, 16(6):1587–1594, 2010.
- [74] A. Joshi and P. Rheingans. Illustration-inspired techniques for visualizing time-varying data. In *Proceedings of VisConference*, pages 679–686, Los Alamitos, CA, USA, 2005. IEEE Computer Society.
- [75] A. Kanitsar, R. Wegenkittl, D. Fleischmann, and M. Gröller. Advanced curved planar reformation: Flattening of vascular structures. *Visualization and Computer Graphics, IEEE Transactions on*, pages 43–50, 2003.

- [76] A. Kaufman. *Volume Visualization*. IEEE Computer Society Press, Los Alamitos, CA, USA, 1991.
- [77] D. Keefe, M. Ewert, W. Ribarsky, and R. Chang. Interactive coordinated multiple-view visualization of biomechanical motion data. *Visualization and Computer Graphics, IEEE Transactions on*, 15(6):1383–1390, 2009.
- [78] D. Keim, F. Mansmann, J. Schneidewind, and H. Ziegler. Challenges in visual data analysis. In *Information Visualization, 2006. IV 2006. Tenth International Conference on*, pages 9–16. IEEE, 2006.
- [79] E. Keppel. Approximating complex surfaces by triangulation of contour lines. *IBM Journal of Research and Development*, 19(1):2–11, 1975.
- [80] R. Kern, F. Perren, S. Kreisel, and K. Szabo. Multiplanar transcranial ultrasound imaging: standards, landmarks and correlation with magnetic resonance imaging. *Ultrasound in Medicine and Biology*, 31(3):311–315, 2005.
- [81] B. H. Kevles. *Naked To The Bone: Medical Imaging In The Twentieth Century*. Basic Books, 1998.
- [82] G. Kindlmann. Superquadric tensor glyphs. In *Proceedings of IEEE Symposium on Visualization*, volume 2004, pages 147–154. Eurographics Association, 2004.
- [83] R. Kirby, D. Keefe, and D. Laidlaw. Painting and visualization. *The Visualization Handbook*, pages 873–891, 2005.
- [84] R. E. Kirk. *Statistics: An Introduction*. Wadsworth Publishing, 2007.
- [85] M. Kitano, H. Sakamoto, U. Matsui, Y. Ito, K. Maekawa, T. von Schrenck, and M. Kudo. A novel perfusion imaging technique of the pancreas: contrast-enhanced harmonic EUS. *Gastrointestinal Endoscopy*, 67(1):141–150, 2008.
- [86] J. Kniss, G. Kindlmann, and C. Hansen. Multidimensional transfer functions for interactive volume rendering. *IEEE Transactions on Visualization and Computer Graphics*, 8(3):270–285, 2002.
- [87] S. Kohle, B. Preim, J. Wiener, and H.-O. Peitgen. Exploration of time-varying data for Medical Diagnosis. In *Vision, Modelling und Visualization (VMV)*, pages 31–38, Erlangen, 2002.
- [88] P. Kondratieva, J. Kruger, and R. Westermann. The application of gpu particle tracing to diffusion tensor field visualization. In *Visualization, 2005. VIS 05. IEEE*, pages 73–78. IEEE, 2005.
- [89] P. R. Krekel, C. P. Botha, E. R. Valstar, P. W. de Bruin, P. M. Rozing, and F. H. Post. Interactive simulation and comparative visualisation of the bone-determined range of motion of the human shoulder. In *SimVis*, pages 275–288, 2006.
- [90] P. R. Krekel, E. R. Valstar, J. D. Groot, F. H. Post, R. G. H. H. Nelissen, and C. P. Botha. Visual analysis of multi-joint kinematic data. *Comput. Graph. Forum*, 29(3):1123–1132, 2010.
- [91] T. Kroes, F. H. Post, and C. P. Botha. Interactive direct volume rendering with physically-based lighting. Preprint 2011-11, Delft University of Technology, 2011.
- [92] D. Laidlaw, E. Ahrens, D. Kremers, M. Avalos, R. Jacobs, and C. Readhead. Visualizing diffusion tensor images of the mouse spinal cord. In *Visualization'98. Proceedings*, pages 127–134. IEEE, 1998.

- [93] O. Lampe, C. Correa, K. Ma, and H. Hauser. Curve-centric volume reformation for comparative visualization. *IEEE Transactions on Visualization and Computer Graphics*, pages 1235–1242, 2009.
- [94] B. Langille and F. O'Donnell. Reductions in arterial diameter produced by chronic decreases in blood flow are endothelium-dependent. *Science*, 231(4736):405–407, 1986.
- [95] R. Laramée, H. Hauser, H. Doleisch, B. Vrolijk, F. Post, and D. Weiskopf. The State of the Art in Flow Visualization: Dense and Texture-Based Techniques. In *Computer Graphics Forum*, volume 23, pages 203–221. Wiley Online Library, 2004.
- [96] R. Laramée, H. Hauser, L. Zhao, and F. Post. Topology-based flow visualization, the state of the art. *Topology-based Methods in Visualization*, pages 1–19, 2007.
- [97] N. Lassau, M. Lamuraglia, L. Chami, J. Leclere, S. Bonvalot, P. Terrier, A. Roche, and A. Le Cesne. Gastrointestinal Stromal Tumors Treated with Imatinib: Monitoring Response with Contrast-Enhanced Sonography. *Am. J. Roentgenol.*, 187(5):1267–1273, 2006.
- [98] T. Lee, A. Chaudhuri, F. Porikli, and H. Shen. Cyclestack: Inferring periodic behavior via temporal sequence visualization in ultrasound video. In *Pacific Visualization Symposium (PacificVis)*, 2010 IEEE, pages 89–96. IEEE, 2010.
- [99] T. C. Lee, R. L. Kashyap, and C. N. Chu. Building skeleton models via 3-d medial surface/axis thinning algorithms. *CVGIP: Graph. Models Image Process.*, 56:462–478, November 1994.
- [100] A. Leroy, P. Mozer, Y. Payan, and J. Troccaz. Intensity-based registration of freehand 3D ultrasound and CT-scan images of the kidney. In *International journal of computer assisted radiology and surgery*, volume 2, pages 31–41, 2007.
- [101] D. Lesage, E. Angelini, I. Bloch, and G. Funka-Lea. A review of 3d vessel lumen segmentation techniques: Models, features and extraction schemes. *Medical Image Analysis*, 13(6):819–845, 2009.
- [102] M. Levoy. Display of surfaces from volume data. *Computer Graphics and Applications, IEEE*, 8(3):29–37, 1988.
- [103] A. Lez, A. Zajic, K. Matkovic, A. Pobitzer, M. Mayer, and H. Hauser. Interactive exploration and analysis of pathlines in flow data. In *Proc. International Conference in Central Europe on Computer Graphics, Visualization and Computer Vision (WSCG 2011)*, pages 17–24, 2011.
- [104] F. Lindemann and T. Ropinski. About the influence of illumination models on image comprehension in direct volume rendering. *Visualization and Computer Graphics, IEEE Transactions on*, 17(12):1922–1931, 2011.
- [105] W. Lorensen and H. Cline. Marching cubes: A high resolution 3d surface construction algorithm. In *ACM Siggraph Computer Graphics*, volume 21, pages 163–169. ACM, 1987.
- [106] D. G. Lowe. Distinctive image features from scale-invariant keypoints. In *International Journal of Computer Vision*, volume 60, pages 91–110, 2004.
- [107] C. Lundström, P. Ljung, and A. Ynnerman. Local histograms for design of transfer functions in direct volume rendering. *IEEE Transactions on Visualization and Computer Graphics*, 12:1570–1579, 2006.

- [108] M. Lysaker, A. Lundervold, and X.-C. Tai. Noise removal using fourth-order partial differential equation with applications to medical magnetic resonance images in space and time. *IEEE Transactions on Image Processing*, 12(12):1579 – 1590, 2003.
- [109] D. Marcus, T. Wang, J. Parker, J. Csernansky, J. Morris, and R. Buckner. Open access series of imaging studies (oasis): cross-sectional mri data in young, middle aged, nondemented, and demented older adults. *Journal of Cognitive Neuroscience*, 19(9):1498–1507, 2007.
- [110] M. Markl, P. Kilner, and T. Ebbers. Comprehensive 4D velocity mapping of the heart and great vessels by cardiovascular magnetic resonance. *Journal of Cardiovascular Magnetic Resonance*, 13(1):7, 2011.
- [111] K. Matkovic, W. Freiler, D. Gracanin, and H. Hauser. Comvis: A coordinated multiple views system for prototyping new visualization technology. In *Information Visualization, 2008. IV'08. 12th International Conference*, pages 215–220. IEEE, 2008.
- [112] T. McLoughlin, R. Laramée, R. Peikert, F. Post, and M. Chen. Over Two Decades of Integration-Based, Geometric Flow Visualization. In *Computer Graphics Forum*, volume 29, pages 1807–1829. Wiley Online Library, 2010.
- [113] S. Meier, A. Hennemuth, O. Friman, J. Bock, M. Markl, and T. Preusser. Non-invasive 4D Blood Flow and Pressure Quantification in Central Blood Vessels via PC-MRI. *Computing in Cardiology*, 37:903–906, 2009.
- [114] C. Merritt. Doppler color flow imaging. *Journal of clinical ultrasound*, 15(9):591–597, 1987.
- [115] J. Meyer-Spradow, L. Stegger, C. Döring, T. Ropinski, and K. Hinrichs. Glyph Based SPECT Visualization for the Diagnosis of Coronary Artery Disease. *IEEE TVCG*, 14(6):1499–1506, 2008.
- [116] M. Mitterberger, A. Pelzer, D. Colleselli, G. Bartsch, H. Strasser, L. Pallwein, F. Aigner, J. Gradl, and F. Frauscher. Contrast-enhanced ultrasound for diagnosis of prostate cancer and kidney lesions. *European Journal of Radiology*, 64(2):231 – 238, 2007.
- [117] M. Mlejnek, P. Ermes, A. Vilanova, R. van der Rijt, H. van den Bosch, F. Gerritsen, and M. E. Gröller. Profile flags: a novel metaphor for probing of T_2 maps. In *Proceedings of IEEE Visualization'05*, pages 599–606, 2005.
- [118] S. A. Napel, C. F. Beaulieu, C. Rodriguez, J. Cui, J. Xu, A. Gupta, D. Korenblum, H. Greenspan, Y. Ma, and D. L. Rubin. Automated Retrieval of CT Images of Liver Lesions on the Basis of Image Similarity: Method and Preliminary Results1. *Radiology*, 256(1):243–252, 2010.
- [119] T. W. Nattkemper and A. Wismaller. Tumor feature visualization with unsupervised learning. *Medical Image Analysis*, 9(4):344–351, 2005.
- [120] M. Neugebauer, R. Gasteiger, O. Beuing, V. Diehl, M. Skalej, and B. Preim. Map displays for the analysis of scalar data on cerebral aneurysm surfaces. In *Computer Graphics Forum*, volume 28, pages 895–902. Wiley Online Library, 2009.
- [121] M. Neugebauer, G. Janiga, O. Beuing, M. Skalej, and B. Preim. Anatomy-guided multi-level exploration of blood flow in cerebral aneurysms. In *Computer Graphics Forum*, volume 30, pages 1041–1050. Wiley Online Library, 2011.
- [122] C. Newton. Graphics in medicine and biology. In *Proceedings of the June 4-8, 1973, national computer conference and exposition*, pages 639–642. ACM, 1973.

- [123] G. Niculescu, D. J. Foran, and J. Noshier. Non-rigid registration of the liver in consecutive CT studies for assessment of tumor response to radiofrequency ablation. In *Proceedings of IEEE Engineering in Medicine and Biology*, pages 856–859, 2007.
- [124] D. C. Nikas, A. Hartov, K. Lunn, K. Rick, K. Paulsen, and D. W. Roberts. Coregistered intraoperative ultrasonography in resection of malignant glioma. *Neurosurg Focus*, 14(2):338–343, 2003.
- [125] T. Nobrega, D. Carvalho, and A. von Wangenheim. Simplified simulation and visualization of tubular flows with approximate centerline generation. In *Computer-Based Medical Systems*, pages 1–7. IEEE, 2009.
- [126] C. North, N. Conklin, K. Indukuri, and V. Saini. Visualization schemas and a web-based architecture for custom multiple-view visualization of multiple-table databases. *Information Visualization*, 1(3-4):211, 2002.
- [127] M. Novotny and H. Hauser. Outlier-preserving focus+context visualization in parallel coordinates. *IEEE Trans. on Visualization and Computer Graphics*, 12:893–900, 2006.
- [128] L. O'Donnell, C. Westin, and A. Golby. Tract-based morphometry. *Medical Image Computing and Computer-Assisted Intervention–MICCAI 2007*, pages 161–168, 2007.
- [129] L. O'Donnell, C. Westin, and A. Golby. Tract-based morphometry for white matter group analysis. *NeuroImage*, 45(3):832–844, 2009.
- [130] S. Oeltze, H. Doleisch, H. Hauser, P. Muigg, and B. Preim. Interactive visual analysis of perfusion data. *IEEE Transactions on Visualization and Computer Graphics*, 13:1392–1399, 2007.
- [131] S. Oeltze, H. Hauser, J. Rørvik, A. Lundervold, and B. Preim. Visual Analysis of Cerebral Perfusion Data – Four Interactive Approaches and a Comparison. In *Proc. of the 6th International Symposium on Image and Signal Processing and Analysis (ISPA)*, pages 588–595, 2009.
- [132] S. Oeltze, A. Hennemuth, S. Glaßer, C. Kühnel, and B. Preim. Glyph-based visualization of myocardial perfusion data and enhancement with contractility and viability information. *VCBM 2008*, pages 11–20, 2008.
- [133] H. Pagendarm and F. Post. Studies in comparative visualization of flow features. *Scientific Visualization, Overviews, Methodologies, and Techniques*, pages 211–227, 1997.
- [134] J. H. Park, S. K. Zhou, C. Simopoulos, J. Otsuki, and D. Comaniciu. Automatic cardiac view classification of echocardiogram. *International Conference on Computer Vision*, pages 1–8, 2007.
- [135] D. Patel, M. Haidacher, J.-P. Balabanian, and M. E. Gröller. Moment curves. In *Proceedings of the IEEE Pacific Visualization Symposium 2009*, pages 201–208, 2009.
- [136] T. Peeters, A. Vilanova, and B. ter Haar Romeny. Visualization of dti fibers using hair-rendering techniques. In *Proc ASCI*, pages 66–73, 2006.
- [137] N. Pelc, R. Herfkens, A. Shimakawa, D. Enzmann, et al. Phase contrast cine magnetic resonance imaging. *Magnetic Resonance Quarterly*, 7(4):229, 1991.
- [138] Z. Peng and R. Laramée. Higher Dimensional Vector Field Visualization: A Survey. *Theory and Practice of Computer Graphics (TPCG)*, pages 149–163, 2009.

- [139] B. Petersch, M. Hadwiger, H. Hauser, and D. Hönlmann. Real time computation and temporal coherence of opacity transfer functions for direct volume rendering of ultrasound data. *Computerized Medical Imaging and Graphics*, 29(1):53–63, 2005.
- [140] B. Petersch and D. Hönlmann. Blood flow in its context: Combining 3d b-mode and color doppler ultrasonic data. *Visualization and Computer Graphics, IEEE Transactions on*, 13(4):748–757, 2007.
- [141] C. Plaisant, B. Milash, A. Rose, S. Widoff, and B. Shneiderman. Lifelines: visualizing personal histories. In *Proceedings of the SIGCHI conference on Human factors in computing systems: common ground*, pages 221–227. ACM, 1996.
- [142] A. Pobitzer, R. Peikert, R. Fuchs, B. Schindler, A. Kuhn, H. Theisel, K. Matkovic, and H. Hauser. On the way towards topology-based visualization of unsteady flow - the state of the art. In *EuroGraphics 2010 State of the Art Reports (STARs)*, pages 137–154, 2010.
- [143] F. Post, B. Vrolijk, H. Hauser, R. Laramée, and H. Doleisch. Feature extraction and visualization of flow fields. *Eurographics 2002 State-of-the-Art Reports*, pages 69–100, 2002.
- [144] F. Post, B. Vrolijk, H. Hauser, R. Laramée, and H. Doleisch. The state of the art in flow visualisation: Feature extraction and tracking. In *Computer Graphics Forum*, volume 22, pages 775–792. Wiley Online Library, 2003.
- [145] M. Postema and O. H. Gilja. Ultrasound-directed drug delivery. *Current Pharmaceutical Biotechnology*, 8(6):355–361, 2007.
- [146] B. Preim and D. Bartz, editors. *Visualization in Medicine*. Morgan-Kaufmann, June 2007.
- [147] B. Preim, S. Oeltze, M. Mlejnek, E. Gröller, A. Hennemuth, and S. Behrens. Survey of the visual exploration and analysis of perfusion data. *Visualization and Computer Graphics, IEEE Transactions on*, 15(2):205–220, 2009.
- [148] B. Preim, S. Oeltze, M. Mlejnek, E. Gröller, A. Hennemuth, and S. Behrens. Survey of the Visual Exploration and Analysis of Perfusion Data. *IEEE Transactions on Visualization and Computer Graphics*, 15(2):205–220, Apr/Mai 2009.
- [149] E. Quaia, F. Calliada, M. Bertolotto, S. Rossi, L. Garioni, L. Rosa, and R. Pozzi-Mucelli. Characterization of Focal Liver Lesions with Contrast-specific US Modes and a Sulfur Hexafluoride-filled Microbubble Contrast Agent: Diagnostic Performance and Confidence. *Radiology*, 232(2):420–430, 2004.
- [150] C. Rezk-Salama. Visual parameters and transfer functions. In *Trends in Interactive Visualization*, pages 99–116. Springer, 2008.
- [151] K. Rick, A. Hartov, D. W. Roberts, K. E. Lunn, H. Sun, and K. D. Paulsen. Graphical user interface for intraoperative neuroimage updating. In *Medical Imaging 2003: Visualization, Image-Guided Procedures, and Display*, pages 210–221, 2003.
- [152] J. Roberts. State of the art: Coordinated & multiple views in exploratory visualization. In *Coordinated and Multiple Views in Exploratory Visualization, 2007. CMV'07. Fifth International Conference on*, pages 61–71. IEEE, 2007.
- [153] N. Rognin, M. Arditi, L. Mercier, P. Frinking, F. Tranquart, A. Anaye, G. Perrenoud, and J. Y. Meuwly. Parametric imaging of dynamic vascular patterns of focal liver lesions in contrast-enhanced ultrasound. In *Proceedings of the 15th European Symposium On Ultrasound Contrast Imaging*, pages 5–9, Jan 2010.

- [154] N. Rognin, P. Frinking, T. Messenger, M. Arditì, G. Perrenoud, and J. Y. Meuwly. A new method for enhancing dynamic vascular patterns of focal liver lesions in contrast ultrasound. *Proceedings of IEEE Ultrasonics Symposium*, 1:546–549, 2007.
- [155] W. Röntgen. On a new kind of rays. *Science*, 3(59):227–231, 1896.
- [156] T. Ropinski, S. Hermann, R. Reich, M. Schäfers, and K. Hinrichs. Multimodal vessel visualization of mouse aorta PET/CT scans. *IEEE Transactions on Visualization and Computer Graphics*, pages 1515–1522, 2009.
- [157] T. Ropinski, J. Meyer-Spradow, S. Diepenbrock, J. Mensmann, and K. Hinrichs. Interactive volume rendering with dynamic ambient occlusion and color bleeding. In *Computer Graphics Forum*, volume 27, pages 567–576. Wiley Online Library, 2008.
- [158] M. Roth and R. Peikert. Flow visualization for turbomachinery design. In *Proceedings of the 7th conference on Visualization'96*, pages 381–384. IEEE Computer Society Press, 1996.
- [159] K. Ryden and C. Newton. Graphics software for remote terminals and their use in radiation treatment planning. In *Proceedings of the May 16-18, 1972, spring joint computer conference*, pages 1145–1156. ACM, 1972.
- [160] A. Sadarjoen, T. Van Walsum, A. Hin, and F. Post. Particle tracing algorithms for 3D curvilinear grids. *Scientific Visualization, Overviews, Methodologies, and Techniques*, pages 311–335, 1997.
- [161] G. Sakas, L. Schreyer, and M. Grimm. Preprocessing and volume rendering of 3D ultrasonic data. *IEEE Computer Graphics and Applications*, 15(4):47–54, 1995.
- [162] T. Salzbrunn, H. Jänicke, T. Wischgoll, and G. Scheuermann. The state of the art in flow visualization: Partition-based techniques. *Simulation and Visualization 2008 Proceedings*, pages 75–92, 2008.
- [163] S. Schäfer, P. Angelelli, K. Nylund, O. Gilja, and K. Tönnies. Registration of ultrasonography sequences based on temporal regions. In *Image and Signal Processing and Analysis (ISPA), 2011 7th International Symposium on*, pages 749–754. IEEE, 2011.
- [164] M. Schwenke, A. Hennemuth, B. Fischer, and O. Friman. Blood flow computation in phase-contrast mri by minimal paths in anisotropic media. *Medical Image Computing and Computer-Assisted Intervention–MICCAI 2011*, pages 436–443, 2011.
- [165] B. Shneiderman. The eyes have it: A task by data type taxonomy for information visualizations. In *Visual Languages, 1996. Proceedings., IEEE Symposium on*, pages 336–343. IEEE, 1996.
- [166] V. Šoltészová, D. Patel, S. Bruckner, and I. Viola. A multidirectional occlusion shading model for direct volume rendering. In *Computer Graphics Forum*, volume 29, pages 883–891. Wiley Online Library, 2010.
- [167] SonoWand. The sonowand system. www.sonowand.no.
- [168] T. Sørensen, P. Beerbaum, H. Körperich, and E. Pedersen. Three-dimensional, isotropic mri: a unified approach to quantification and visualization in congenital heart disease. *The International Journal of Cardiovascular Imaging (formerly Cardiac Imaging)*, 21(2):283–292, 2005.
- [169] M. D. Steenwijk, J. Milles, M. A. Buchem, J. H. Reiber, and C. P. Botha. Integrated Visual Analysis for Heterogeneous Datasets in Cohort Studies. In *IEEE VisWeek Workshop on Visual Analytics in Health Care*.

- [170] C. Stolte, D. Tang, and P. Hanrahan. Polaris: A system for query, analysis, and visualization of multidimensional relational databases. *Visualization and Computer Graphics, IEEE Transactions on*, 8(1):52–65, 2002.
- [171] K. Sugimoto, F. Moriyasu, N. Kamiyama, R. Metoki, and H. Iijima. Parametric imaging of contrast ultrasound for the evaluation of neovascularization in liver tumors. *Hepatology Research*, 37(6):464–472, 2007.
- [172] Sullivan, E.V. and Rohlfing, T. and Pfefferbaum, A. Quantitative fiber tracking of lateral and interhemispheric white matter systems in normal aging: Relations to timed performance. *Neurobiology of aging*, 31(3):464–481, 2010.
- [173] A. Sunguroff and D. Greenberg. Computer generated images for medical applications. *ACM SIGGRAPH Computer Graphics*, 12(3):196–202, 1978.
- [174] M. Termeer. Comprehensive Visualization of Cardiac MRI Data, 2009.
- [175] K. D. Toennies, A. Celler, S. Blinder, T. Moeller, and R. Harrop. Scatter segmentation in dynamic spect images using principal component analysis. In *Proceedings of SPIE, San Diego, Part I*, pages 507–516, 2003.
- [176] J. W. Tukey. *Exploratory Data Analysis*. Addison Wesley, 1977.
- [177] T. Twellmann, O. Lichte, and T. Nattkemper. An adaptive tissue characterization network for model-free visualization of dynamic contrast-enhanced magnetic resonance image data. *Medical Imaging, IEEE Transactions on*, 24(10):1256–1266, oct. 2005.
- [178] J. Udupa, H. Hung, and K. Chuang. Surface and volume rendering in three-dimensional imaging: a comparison. *Journal of digital Imaging*, 4(3):159–168, 1991.
- [179] A. Van Dixhoorn, B. Vissers, L. Ferrarini, J. Milles, and C. P. Botha. Visual analysis of integrated resting state functional brain connectivity and anatomy. In *Eurographics Workshop on Visual Computing for Biology and Medicine*, 2010.
- [180] R. van Pelt, J. Bescós, M. Breeuwer, R. Clough, M. Gröller, B. ter Haar Romeny, and A. Vilanova. Exploration of 4D MRI Blood Flow using Stylistic Visualization. *Visualization and Computer Graphics, IEEE Transactions on*, 16(6):1339–1347, 2010.
- [181] R. van Pelt, J. Oliván Bescos, M. Breeuwer, R. Clough, M. Groller, B. ter Haar Romenij, and A. Vilanova. Interactive virtual probing of 4d mri blood-flow. *Visualization and Computer Graphics, IEEE Transactions on*, 17(12):2153–2162, 2011.
- [182] V. Verma and A. Pang. Comparative flow visualization. *Visualization and Computer Graphics, IEEE Transactions on*, 10(6):609–624, 2004.
- [183] A. Vilanova, E. Gröller, and A. König. Cylindrical approximation of tubular organs for virtual endoscopy. In *Proceedings of Computer Graphics and Imaging*, volume 11, pages 283–289, 2000.
- [184] A. Vilanova, R. Wegenkittl, A. König, and E. Gröller. Nonlinear virtual colon unfolding. *Visualization and Computer Graphics, IEEE Transactions on*, pages 411–418, 2001.
- [185] I. Viola, M. Feixas, M. Sbert, and E. Gröller. Importance-driven focus of attention. *IEEE Transactions on Visualization and Computer Graphics*, 12(5):933–940, Oct 2006.
- [186] I. Viola, M. E. Gröller, M. Hadwiger, K. Bühler, B. Preim, and D. Ebert. Illustrative Visualization. In undefined, editor, *Eurographics Conference 2005 – Tutorials*, pages 187–329, undefined. Eurographics Association.

- [187] I. Viola, K. Nylund, O. K. Øye, D. M. Ulvang, O. H. Gilja, and H. Hauser. Illustrated ultrasound for multimodal data interpretation of liver examinations. In *Visual Computing in Biomedicine proceedings*, pages 125–133, Oct 2008.
- [188] I. Viola, M. C. Sousa, D. Ebert, B. Andrews, B. Gooch, S. Bruckner, B. Preim, D. Stredney, N. Svakhine, and C. Tietjen. Illustrative Visualization for Science and Medicine. IEEE Visualization Conference Tutorial, 2006.
- [189] A. Voineskos, T. Rajji, N. Lobaugh, D. Miranda, M. Shenton, J. Kennedy, B. Pollock, and B. Mulsant. Age-related decline in white matter tract integrity and cognitive performance: a dti tractography and structural equation modeling study. *Neurobiology of aging*, 2010.
- [190] T. Vrtovec, B. Likar, and F. Pernuš. Automated curved planar reformation of 3D spine images. *Physics in medicine and biology*, 50:4527, 2005.
- [191] T. Wang, C. Plaisant, B. Shneiderman, N. Spring, D. Roseman, G. Marchand, V. Mukherjee, and M. Smith. Temporal summaries: Supporting temporal categorical searching, aggregation and comparison. *Visualization and Computer Graphics, IEEE Transactions on*, 15(6):1049–1056, 2009.
- [192] M. Ward. Xmdvtool: Integrating multiple methods for visualizing multivariate data. In *Proceedings of the Conference on Visualization'94*, pages 326–333. IEEE Computer Society Press, 1994.
- [193] C. Weaver. Cross-filtered views for multidimensional visual analysis. *Visualization and Computer Graphics, IEEE Transactions on*, 16(2):192–204, 2010.
- [194] T. C. Williams, W. B. DeMartini, S. Peacock, and C. D. Lehman. Breast MR Imaging: Computer-aided Evaluation Program for Discriminating Benign from Malignant Lesions. *Radiology*, 244(1):94–103, 2007.
- [195] P. Wong and J. Thomas. Visual analytics. *Computer Graphics and Applications, IEEE*, 24(5):20–21, 2004.
- [196] J. Woodring and H.-W. Shen. Chronovolumes: A direct rendering technique for visualizing time-varying data. In *Volume Graphics*, pages 27–34, 2003.
- [197] M. Ystad, T. Eichele, A. Lundervold, and A. Lundervold. Subcortical functional connectivity and verbal episodic memory in healthy elderly—a resting state fmri study. *Neuroimage*, 52(1):379–388, 2010.
- [198] M. Ystad, E. Hodneland, S. Adolfsdottir, J. Haász, A. Lundervold, T. Eichele, and A. Lundervold. Cortico-striatal connectivity and cognition in normal aging: A combined dti and resting state fmri study. *Neuroimage*, 55(1):24–31, 2011.
- [199] M. Ystad, A. Lundervold, E. Wehling, T. Espeseth, H. Rootwelt, L. Westlye, M. Andersson, S. Adolfsdottir, J. Geitung, A. Fjell, et al. Hippocampal volumes are important predictors for memory function in elderly women. *BMC medical imaging*, 9(1):17, 2009.